SUSTAINABLE MARINE STRUCTURES

NASS
NAN YANG ACADEMY OF SCIENCES

SUSTAINABLE MARINE STRUCTURES

Editor-in-Chief

Prof. Erkan Oterkus

University of Strathclyde,
United Kingdom

Prof. Xiangyuan Zheng
Tsinghua University, China

Contents

ARTICLE

Comparison of Potential Theory and Morison Equation for Deformable Horizontal Cylinders

Chungkuk Jin[*]

Department of Ocean Engineering, Texas A&M University, Texas, the United States

ABSTRACT

This study investigates the hydro-elastic behaviors of fully submerged horizontal cylinders in different regular waves. Two methods were proposed and compared in this study. The first method was based on potential theory in frequency domain and the discrete-module-beam (DMB) method, which discretizes a floating elastic structure into a sufficient number of rigid bodies while simultaneously representing the elastic behavior from beam elements with Euler-Bernoulli beam and Saint-Venant torsion. Moreover, the Morison method in time domain was employed; this method estimates wave forces from the semi-empirical Morison equation, and the elastic behavior is embodied by massless axial, bending, and torsional springs. Various parametric studies on cylinder diameter, submergence depth, and wave direction were conducted. Wave forces, dry/wet mode shapes/natural frequencies, and dynamic motions are presented and analyzed.

1. Introduction

Underwater cylindrical structures have been suggested for various reasons. Many of them lie on the seabed, and typical examples include submarine pipelines that transport water, oil, and natural gas, submarine cables for electricity transmission, and immersed tunnels for public transportation. Even if these structures have accumulated engineering practices, several critical limitations still exist. These structures are susceptible to seismic activities [1,2]; the seabed should be even for installation; scours, the removal of sediment around the pipeline, can occur and are critical for vibration and fatigue damage associated with seabed movement [3]. Also, the deepwater application is very challenging for submarine pipelines and cables due to not only high hydrostatic pressure and temperature difference but also high costs associated with a longer length and additional intervention work for the seabed [4].

Submerged floating structures have been proposed as novel alternatives to the above structures, and representative examples are submerged floating pipelines and submerged floating tunnels. These structures float at a submergence depth and keep their location with mooring

---

*Corresponding Author:
Chungkuk Jin,
Department of Ocean Engineering, Texas A&M University, Texas, the United States;
Email: jinch999@tamu.edu

systems if needed. They have several advantages: (1) they can be safe from wave and seismic actions by properly selecting design parameters, (2) the deepwater application is much more straightforward without considerable hydrostatic pressure and temperature difference, as in the deepwater location, and (3) structural health monitoring is much easier [4-9].

Their considerable dynamic and structural behavior and the resulting large mooring tension are still considered severe under various environmental conditions such as waves, currents, earthquakes, and tsunamis. Many studies adopted the Morison equation [10] for force estimation of the horizontal cylinder [11-13] due to low computational cost. However, the Morison equation has limitations in that wavelength should be more than five times the characteristic length ($D/L \le 0.2$ where D is cylinder diameter and L is wavelength), and the radiation effect is neglected. In addition, when the structure is close to free surface, the free-surface effect can be substantial, which results in a considerable variation of the scattering wave force compared with the deeply submerged structure cases [14]. The resulting mooring tension can also be different to a great extent. In this regard, validation work of the Morison equation for fully submerged floating structures is essential with respect to different diameters, submergence depths, and wave directions.

Several papers discussed the validity of the Morison equation by comparing it with theory-based approaches. Typically, the inertia coefficient C_M is fixed at 2 according to the slender body assumption and can vary for the non-slender body. For example, Chakrabarti and Tam [15] estimated the effective inertia coefficient for the Morison equation for bottom-mounted surface-piecing vertical cylinder and proved that the effective inertia coefficient significantly decreases as D/L increases. Chung [16] stated that when an object is close to free surface, the inertia coefficient can be a function of frequency, and radiation damping can be empirically added. In other words, its validity may be weakened when the free-surface effect exists to a great degree. Chang et al. [17] showed that the Morison equation reasonably estimates wave force up to second order for the hinged vertical cylinder at small wave steepness. However, they also mentioned that the Morison equation underestimates the peak wave force and overestimates trough wave forces at high wave steepness. Varying inertia coefficients along the submergence depth are proposed as in Ref. [18]. Regarding horizontal cylinders, Li et al. [19] conducted experimental studies for in-line responses for a submerged horizontal cylinder and showed that the inertia coefficient is not changing significantly with respect to the Keulegan-Carpenter number as

opposed to vertical cylinders. Chen et al. [20] compared the Morison equation with CFD simulation and showed that the Morison equation underestimates the wave force on a partially submerged horizontal cylinder by up to 50% relative errors.

This study compared the potential theory with the Morison equation for fully-submerged horizontal cylinders. Both ends were fixed with the fixed-fixed boundary condition in which there are no displacements and angles at both ends. The multibody-based hydro-elasticity method with the potential theory in frequency domain—referred to as the discrete-module-beam (DMB) method—was compared with the lumped mass method with Morison equation—referred to as the Morison method. The Froude-Krylov, scattering wave, and radiation damping forces in the DMB method were compared with the inertia force of the Morison equation in the Morison method. Dry/wet natural frequencies/mode shapes and horizontal/vertical motions/forces were systematically presented and analyzed.

2. Theory and Formulation

Two different approaches were selected to evaluate dynamic behaviors and wave forces for a fully submerged horizontal cylinder. The first method was the DMB method, in which wave forces are estimated by 3-dimensional (3D) potential theory in frequency domain and Euler-Bernoulli beam and Saint-Venant torsion are employed for representing elastic behaviors. The second method is the Morison method, in which the Morison equation estimates wave forces with representative added mass and inertia coefficients in time domain while beam elements are modeled by the lumped mass method with massless axial, bending, and torsional springs. The theory and formulation of the two methods are explained in this section. Detailed formulations regarding the two methods and their validations can be found in Refs [12,21,22].

2.1 Discrete-Module-Beam Method in Frequency Domain

The DMB method is based on 3D potential theory for the multibody in frequency domain; a large deformable structure consists of M rigid bodies and $M-1$ connecting beams [23,24], as shown in Figure 1. The DMB method uses the right-handed Cartesian coordinate system.
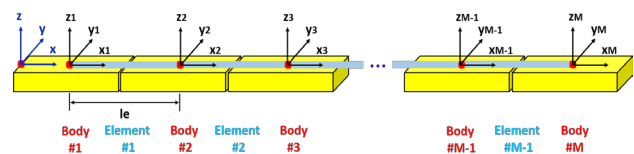

Figure 1. DMB method [25].

Laplace equation is governing equation for the potential theory when fluid is incompressible, irrotational, and inviscid as:

$$\nabla^2 \Phi = 0$$
$$\Phi = \varphi e^{-i\omega t} \tag{1}$$

where Φ is the total time-dependent velocity potential, which can be decomposed into the total time-independent velocity potential φ and the time-dependent term $e^{-i\omega t}$ based on the assumption of harmonic excitation with wave angular frequency ω and time t. φ can further be decomposed into diffraction and radiation components with the incident, scattered, and radiation potentials φ_I, φ_S, and $\varphi_R^{(m)}$ as:

$$\varphi = \varphi_I + \varphi_S + \sum_{m=1}^{M} \varphi^{(m)}$$
$$\varphi_R^{(m)} = -i\omega \sum_{j=1}^{6} \xi_j^{(m)} \varphi_{jR}^{(m)} \tag{2}$$

where m represents the mth rigid body and $\xi_j^{(m)}$ is six degrees of freedom (6DOF) displacements of the mth rigid body, i.e., surge, sway, heave, roll, pitch, and yaw motions. First-order φ_I can be written as:

$$\varphi_I = \frac{igA_w}{\omega} \frac{\cosh k(z+H)}{\cosh kH} e^{ik(x\cos\theta + y\sin\theta)} \tag{3}$$

where A_w is the amplitude of an incident wave, k is the wavenumber, H is water depth, θ is the wave direction, and g is the gravity acceleration. Moreover, φ_S and $\varphi_R^{(m)}$ can be obtained by considering the following boundary conditions on the free surface S_F, bottom S_B, body $S_k (k = 1, 2, ..., M)$, and far-field S_∞ as:

$$\left(-\omega^2 + g\frac{\partial}{\partial z}\right)\varphi^\times = 0 \qquad \text{on } S_F (z=0)$$

$$\frac{\partial \varphi^\times}{\partial z} = 0 \qquad \text{on } S_B (z = -H)$$

$$\frac{\partial \varphi_S}{\partial n} = -\frac{\partial \phi_I}{\partial n} \qquad \text{on } S_k \tag{4}$$

$$\frac{\partial \varphi_{jR}^{(m)}}{\partial n^{(k)}} = \begin{cases} n_j^{(m)}, & k = m \\ 0, & k \neq m \end{cases} \qquad \text{on } S_k$$

$$\lim_{r\to\infty} \sqrt{r}\left(\frac{\partial}{\partial r} - ik\right)\varphi^\times = 0 \qquad \text{on } S_\infty$$

where r is the radial distance from the origin. $\varphi^\times$ can be φ_S or $\varphi_{jR}^{(m)}$. $n_j^{(m)}$ is the inward unit normal vector for the jth DOF on the mth body surface with respect to the body-fixed coordinate system. φ_S and $\varphi_{jR}^{(m)}$ are obtained by the 3D boundary element method. Each body's coordinate center is its center of gravity.

The wave excitation force that is the sum of the Froude-Krylov and scattered wave forces for the jth DOF

on the mth rigid body in the body-fixed coordinate system is given in Equation (5):

$$F_{jW}^{(m)} = i\rho\omega \iint_{S_m} (\varphi_I + \varphi_S) n_j^{(m)} dS \tag{5}$$

The radiation force for the jth DOF on the mth rigid body induced by the kth DOF of the nth rigid body in the body-fixed coordinate system is given in Equation (6):

$$F_{jkR}^{(mn)} = \omega^2 A_{jk}^{(mn)} \xi_k^{(n)} + i\omega B_{jk}^{(mn)} \xi_k^{(n)} = \rho\omega^2 \xi_k^{(n)} \iint_{S_m} \varphi_{kR}^{(n)} \frac{\partial \varphi_{jR}^{(m)}}{\partial n^{(m)}} dS \tag{6}$$

where $A_{jk}^{(mn)}$ and $B_{jk}^{(mn)}$ denote the added mass and radiation damping coefficients of the jth DOF of the mth rigid body induced by the kth DOF of the nth rigid body. In addition, the hydrostatic restoring force of the mth rigid body for the jth DOF is given in Equation (7):

$$F_{jH}^{(m)} = -\rho g \iint_{S_m} \left(\xi_3^{(m)} + \xi_4^{(m)} y_m - \xi_5^{(m)} x_m\right) n_j^{(m)} dS \tag{7}$$

After the hydrodynamic forces and coefficients have been introduced, the equation of motion for M rigid bodies can be written with the mass, added mass, radiation damping, hydrostatic restoring coefficient matrices, $\mathbf{M}$, $\mathbf{A}$, $\mathbf{B}$, and $\mathbf{K}$, and wave-excitation-force vector $\mathbf{F}_W$ as:

$$(\mathbf{M} + \mathbf{A}(\omega))\ddot{\xi} + (\mathbf{B}(\omega) + \mathbf{B_R})\dot{\xi} + (\mathbf{K} + \mathbf{K}_E)\xi = \mathbf{F}_W(\omega) \tag{8}$$

where upper dot means time derivative and $\mathbf{B_R}$ is the structural damping matrix. In Equation (8), the external stiffness matrix $\mathbf{K}_E$ is introduced to consider the elastic behavior of a deformable floating structure. $\mathbf{K}_E$ is constructed with Euler-Bernoulli beam and Saint-Venant's torsion theory for $M-1$ beam elements. The 12 by 12 sub-stiffness matrix $\mathbf{K}_e$ for the eth beam element in the local coordinate system is given in Equation (9):

$$\mathbf{K}_e = \begin{bmatrix}
\frac{EA_c}{l_e} & & & & & & & & & & & \text{symm.} \\
0 & \frac{12EI_z}{l_e^3} & & & & & & & & & & \\
0 & 0 & \frac{12EI_y}{l_e^3} & & & & & & & & & \\
0 & 0 & 0 & \frac{GI_x}{l_e} & & & & & & & & \\
0 & 0 & -\frac{6EI_y}{l_e^2} & 0 & \frac{4EI_y}{l_e} & & & & & & & \\
0 & \frac{6EI_z}{l_e^2} & 0 & 0 & 0 & \frac{4EI_z}{l_e} & & & & & & \\
-\frac{EA_c}{l_e} & 0 & 0 & 0 & 0 & 0 & \frac{EA_c}{l_e} & & & & & \\
0 & -\frac{12EI_z}{l_e^3} & 0 & 0 & 0 & -\frac{6EI_z}{l_e^2} & 0 & \frac{12EI_z}{l_e^3} & & & & \\
0 & 0 & -\frac{12EI_y}{l_e^3} & 0 & \frac{6EI_y}{l_e^2} & 0 & 0 & 0 & \frac{12EI_y}{l_e^3} & & & \\
0 & 0 & 0 & -\frac{GI_x}{l_e} & 0 & 0 & 0 & 0 & 0 & \frac{GI_x}{l_e} & & \\
0 & 0 & -\frac{6EI_y}{l_e^2} & 0 & \frac{2EI_y}{l_e} & 0 & 0 & 0 & \frac{6EI_y}{l_e^2} & 0 & \frac{4EI_y}{l_e} & \\
0 & \frac{6EI_z}{l_e^2} & 0 & 0 & 0 & \frac{2EI_z}{l_e} & 0 & -\frac{6EI_z}{l_e^2} & 0 & 0 & 0 & \frac{4EI_z}{l_e}
\end{bmatrix} \tag{9}$$

where E and G are Young's and shear moduli, A_c is the cross-sectional area, l_e is the element length, and I_x, I_y, and I_z are the torsional, vertical, and lateral second moments of area about x, y, and z axes, respectively. $\mathbf{K}_E$ can be expressed for $M-1$ beam elements with the 6 by 6 sub-stiffness matrices of $\mathbf{K}_e$ as:

$$\mathbf{K}_E = \begin{bmatrix} \mathbf{K}_1^{(11)} & \mathbf{K}_1^{(12)} & 0 & \cdots & 0 \\ \mathbf{K}_1^{(21)} & \mathbf{K}_1^{(22)}+\mathbf{K}_2^{(11)} & \mathbf{K}_2^{(12)} & \cdots & 0 \\ 0 & \mathbf{K}_2^{(21)} & \mathbf{K}_2^{(22)}+\mathbf{K}_3^{(11)} & \cdots & 0 \\ \vdots & \vdots & \vdots & \ddots & \vdots \\ 0 & 0 & 0 & \cdots & \mathbf{K}_{M-1}^{(22)} \end{bmatrix} \quad (10)$$

$$\mathbf{K}_e = \begin{bmatrix} \mathbf{K}_e^{(ii)} & \mathbf{K}_e^{(ij)} \\ \mathbf{K}_e^{(ji)} & \mathbf{K}_e^{(jj)} \end{bmatrix}$$

2.2 Morison Method in Time Domain

The Morison method was also modeled in time domain [26]. In this method, a deformable floating structure consists of finite elements with nodes and segments. Key physical properties are included in the nodes while segments present structure's deformability with massless axial, bending, and torsional springs. The Morison equation evaluates the hydrodynamic forces for a moving body at its instantaneous node position. The computational time of this method is lower than the frequency-domain DMB method since this method is dependent on the Morison equation for wave-force estimation. It is worth utilizing this method if accurate global performance estimation is possible with a cheaper computational cost. The equation of motion for a deformable floating structure in time domain can be expressed as:

$$\mathbf{M}\ddot{\mathbf{X}} + \mathbf{B_R}\dot{\mathbf{X}} + \mathbf{K_S}\mathbf{X} = \mathbf{F_M} + \mathbf{w}$$

$$\mathbf{F_M} = -C_A \Delta \ddot{\mathbf{X}}^n + C_M \Delta \dot{\boldsymbol{\eta}}^n + \frac{1}{2} C_D \rho A \left| \boldsymbol{\eta}^n - \dot{\mathbf{X}}^n \right| \left(\boldsymbol{\eta}^n - \dot{\mathbf{X}}^n \right) \quad (11)$$

where $\mathbf{K_S}$ are the structural stiffness matrix, $\mathbf{F_M}$ is the hydrodynamic force vector based on the Morison equation, $\mathbf{w}$ is the wet-weight vector (i.e., buoyancy minus dry weight), C_A, C_M, and C_D are the added mass, inertia, and drag coefficients, Δ and A are the displaced mass and drag area, ρ is the seawater density, η and $\dot{\eta}$ are the velocity and acceleration vectors of fluid particles, and n denotes the normal direction. Structural deformability

is represented by K_S with axial, bending, and torsional springs. The drag term of the Morison equation, i.e., 3rd term in Equation (11), was neglected since the Keulegan-Carpenter number of the presented problem is low (inertia dominant).

3. Case Description

Figure 2 shows the configuration of a concrete hollow cylinder. Its density and Young's modulus were 2300 kg/m³ and 30 GPa. The length of the concrete cylinder was fixed at 500 m, whereas various diameters of 10 m–20 m, submergence depths of 20 m–60 m, and wave directions of 30°–90° were selected as design parameters. In this study, the cylinder's buoyancy-weight ratio was set at 1.0, which means its buoyancy is the same as its dry weight. Then, the inner diameter and axial, bending, and torsional stiffness were reversely estimated based on the given buoyancy-weight ratio. The fixed-fixed boundary condition at both ends was designed; in other words, displacements and angles at both ends do not change. Water depth was fixed at 100 m.

4. Results and Discussions

4.1 Wave Force

The wave excitation force $\mathbf{F_W}$ in potential theory is often correlated with the inertia force term $\mathbf{F_I}$ in the Morison equation, i.e., 2nd term in Equation (11). $\mathbf{F_I}$ is with the inertia coefficient $C_M (=1+C_A)$, and 1 and C_A are associated with contributions from the Froude-Krylov force and scattered wave force. The validity of the Morison equation is then assessed by comparing $\mathbf{F_W}$ and $\mathbf{F_I}$. Figures 3–4 show the comparison of horizontal/vertical $\mathbf{F_W}$ and $\mathbf{F_I}$ (wave force per unit length). Wave direction was fixed at 90°
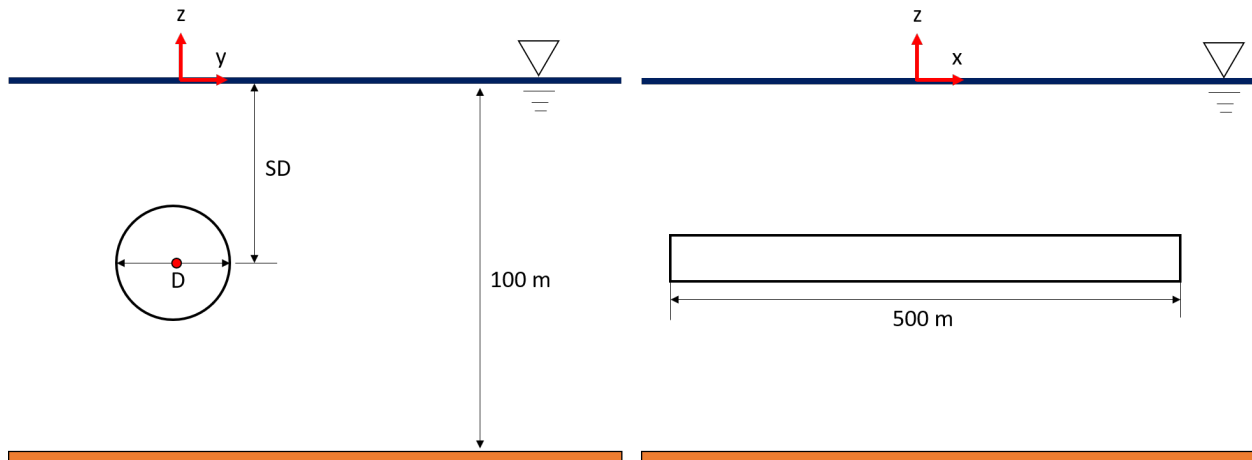
Figure 2. Configuration of a cylinder with fixed-fixed boundary condition (D denotes diameter; SD stands for submergence depth).

with respect to the positive x-axis, and $\mathbf{F_I}$ was calculated from the fixed body. At a low submergence depth of 20 m, which is close to free surface, trends and magnitudes of $\mathbf{F_W}$ are somewhat different from those of $\mathbf{F_I}$, as shown in Figure 3(a) and (c). The Morison model tends to overestimate the wave force at high frequencies of 0.7 rad/s or more. However, $\mathbf{F_W}$ and $\mathbf{F_I}$ are very close at higher submergence depths, regardless of the wave frequency range, as shown in Figure 3(b) and (d), which means that the Morson method can estimate the wave force accurately for deeply submerged cylinders even if the cylinder diameter is large. Moreover, the higher the submergence depth, the lower the importance of high-frequency wave forces since the wave kinematics decreases with submergence depth as a function of $\cosh k(z+H)$ for intermediate water and e^{kz} for deep water. As shown in Figure 4, the difference between the two forces is significantly reduced at a small diameter of 10 m even if the submergence depth is 20 m.

The previous results show that the Morison equation accurately estimates the wave inertia force at the large submergence depth and small cylinder diameter. It is well known that the Morison equation has a limitation, i.e.,

$D/L \le 0.2$. At the given water depth of 100 m and a cylinder diameter of 20 m, the wave frequency should be less than around 0.8 rad/s to be included in this condition. The scattered wave force $\mathbf{F_{SC}}$ is mainly associated with this limitation since the scattered wave force has a tendency to be important as the wave frequency increases. Figure 5 shows the comparison of the Froude-Krylov force $\mathbf{F_{FK}}$ and $\mathbf{F_{SC}}$ in the DMB method with half of $\mathbf{F_I}$ in the Morison method $(0.5\mathbf{F}_I = \mathbf{F_{MF}})$ that corresponds to $\mathbf{F_{FK}}$ in the DMB method. Wave kinematics for the Morison equation is estimated at the geometric center, while that for $\mathbf{F_{FK}}$ is based on the cylinder surface. At the given cylinder diameters, regardless of submergence depths, $\mathbf{F_{MF}}$ is similar to $\mathbf{F_{FK}}$, which means that kinematics estimation at the geometric center in the Morison method is still valid for this horizontal cylinder at the given frequency range. Then, as noticed in Figure 5(a), $\mathbf{F_{SC}}$ induces the difference between $\mathbf{F_W}$ and $\mathbf{F_I}$ only when submergence depth is low. In this case, the existence of free surface influences the calculation of $\mathbf{F_{SC}}$. No free-surface effect is detected when the submergence depth is 60 m due to a large distance between free surface and the cylinder.
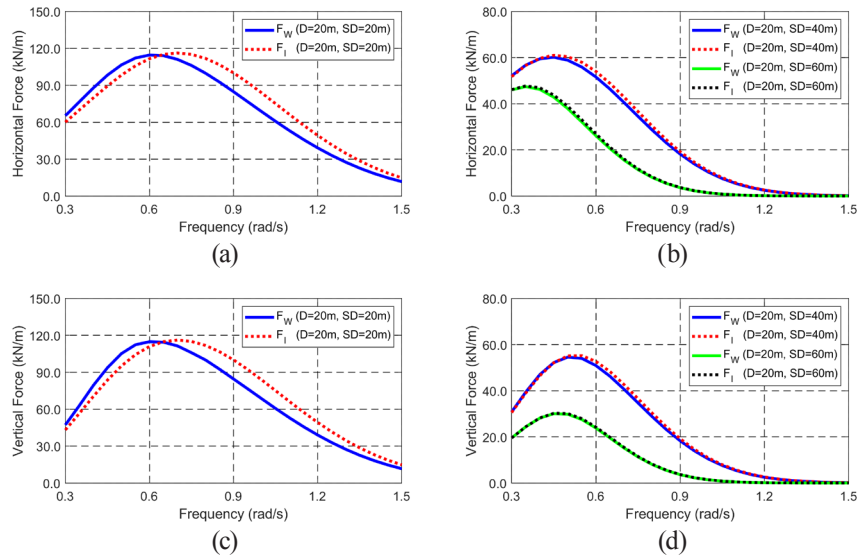
Figure 3. Comparison of horizontal/vertical $\mathbf{F_W}$ and $\mathbf{F_I}$ at a diameter of 20 m and different submergence depths.
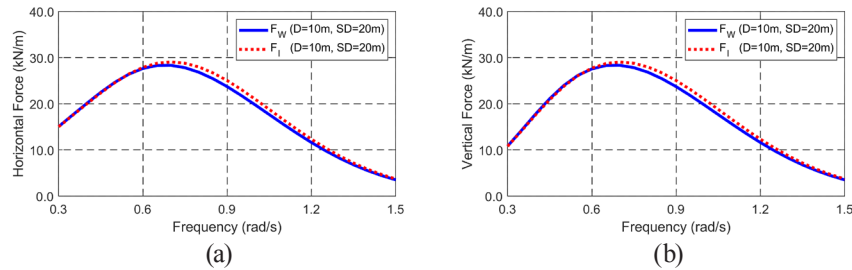
Figure 4. Comparison of horizontal/vertical $\mathbf{F_W}$ and $\mathbf{F_I}$ at a diameter of 10 m and a submergence depth of 20 m.
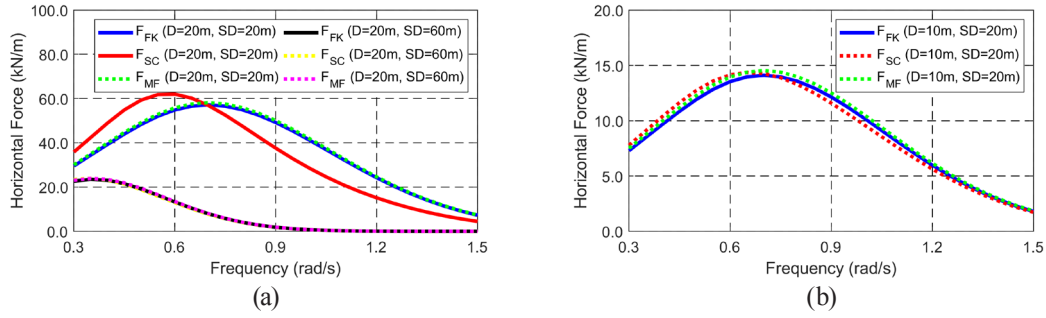
Figure 5. Comparison of F_{FK}, F_{SC}, and F_{MF} at different diameters and submergence depths.

4.2 Modal Analysis

Next, modal analysis was conducted, and dry/wet mode shapes/natural frequencies were obtained. Wet mode shapes and natural frequencies require the added mass and hydrostatic restoring coefficient matrices. In the Morison equation, C_A is typically selected as 1 based on previous practices for the slender body [27]. However, the added mass is frequency-dependent, and wet mode shapes and natural frequencies can be changed. Tables 1-2 give dry and wet natural frequencies at different diameters and submergence depths. Morison and DMB models calculate similar dry natural frequencies with a maximum difference of 0.3%. Note that elements number for DMB and Morison methods for this example are 22 and 50, respectively. Since the Morison method is based on the lumped mass method, more elements are generally required than the high-order beam-based DMB method. Twenty-two finite elements in the DMB method are sufficient to represent the elastic behavior. For the wet mode, while both approaches are well matched at a small diameter of 10 m or a large submergence depth of 60 m, the large difference is observed when diameter and submergence depth are both 20 m. In this case, free surface plays some roles in the modification of wet natural frequencies by changing added mass. The maximum difference is increased to be 5.0%. In this regard, when a cylinder is large and close to free surface, special care should be made to evaluate wet natural frequencies.

Figure 6 shows the representative wet mode shapes of two methods at the diameter and submergence depth of 20 m. Even if there is a maximum difference of 5% in wet natural frequencies, there is no noticeable difference in the wet mode shape up to 3rd mode.

Table 1. Dry natural frequencies at different diameters.

D(m)	Direction	Mode#	Morison (rad/s)	DMB (rad/s)	Difference (%)
20	Horizontal	1	2.01	2.01	0.0
		2	5.51	5.51	-0.1
		3	10.73	10.73	-0.3
	Vertical	1	2.01	2.01	0.0
		2	5.51	5.51	-0.1
		3	10.73	10.73	-0.3
10	Horizontal	1	1.01	1.01	-0.3
		2	2.77	2.76	-0.2
		3	5.40	5.38	-0.3
	Vertical	1	1.01	1.01	-0.3
		2	2.77	2.76	-0.2
		3	5.40	5.38	-0.3

Table 2. Wet natural frequencies at different diameters and submergence depths.

D(m)	SD(m)	Direction	Mode#	Morison (rad/s)	DMB (rad/s)	Difference (%)
20	20	Horizontal	1	1.42	1.50	5.0
			2	3.91	4.04	3.4
			3	7.62	7.88	3.4
		Vertical	1	1.42	1.49	4.9
			2	3.91	4.06	3.7
			3	7.62	7.94	4.1
20	60	Horizontal	1	1.42	1.42	0.1
			2	3.91	3.93	0.5
			3	7.62	7.70	1.1
		Vertical	1	1.42	1.42	-0.3
			2	3.91	3.91	0.2
			3	7.62	7.68	0.8
10	20	Horizontal	1	0.71	0.72	0.3
			2	1.96	1.98	1.0
			3	3.82	3.86	1.0
		Vertical	1	0.71	0.72	0.3
			2	1.96	1.98	0.9
			3	3.82	3.85	0.7
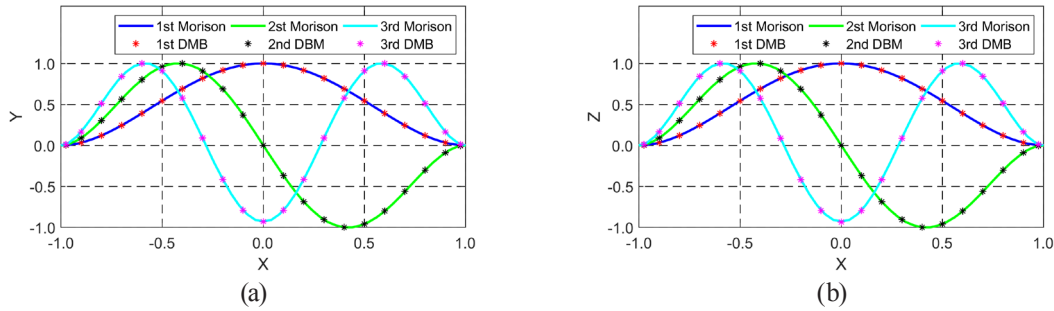
Figure 6. Wet mode shapes at the diameter and submergence depth of 20 m.

4.3 Global Behavior

In previous sections, there were two distinct differences between the DMB and Morison methods; at the diameter and submergence depth of 20 m, the existence of free surface changes the scattered wave force and added mass, which results in differences in total wave force and wet natural frequencies. In this section, global behaviors are further checked at different wave directions. The structural damping matrix based on Rayleigh damping $\mathbf{B_R}$ was added to deal with unrealistic resonant motions at natural frequencies. This study assumes a representative damping ratio of 5% for concrete structures at the fundamental horizontal and vertical natural frequencies.

Figure 7 shows the amplitude envelopes of horizontal and vertical displacements at the diameter and submergence depth of 0.2 m and wave direction of 90°. It turns out that the lowest mode shape is dominant for the given frequency range. In other words, the lowest horizontal and vertical natural frequencies for the DMB method are around 1.50 rad/s and 1.49 rad/s, and thus the lowest natural frequency is dominant for the given frequency range of 0.3 rad/s–1.3 rad/s. Since the Morison method overestimates the wave force at the high-frequency region, highly overestimated motions are seen, especially when wave frequency is close to the fundamental natural frequency.

7

Since the center has the most considerable movement related to the fixed-fixed boundary condition at both ends, results at the mid-length are presented in the later section.

Figure 8 shows the horizontal and vertical motions at the diameter of 20 m, different submergence depths of 20 m and 60 m, and wave direction of 90°. Again, the motion trend coincides with wave force. Overevaluated motions by the Morison method at the submergence depth of 20 m are observed, particularly in the high-frequency region. Since fundamental wet natural frequency for the Morison method is lower than that for the DMB method, resonant induced motion associated with high wave force is detected for the Morison method. On the other hand, the Morison method accurately estimates displacements for deeply submerged cylinders for the given frequency range since wet natural frequencies and wave forces between the two approaches coincide.

Finally, Figure 9 shows the horizontal and vertical motions at the diameter and submergence depth of 20 m and different wave directions of 30° and 60°. As wave direction is not perpendicular to the cylinder, there is an arrival time lag of input waves along the length, which can induce a phase cancellation effect where wave force in the different locations can be canceled out. The phase cancellation effect can be dominant in the high-frequency region. In this example, the lower the wave direction, the smaller the high-frequency motions. As shown in Figure 3, the DMB model estimates the higher wave excitation force for the range of 0.3 rad/s–0.7 rad/s; thus, the DMB model tends to produce higher motion than the Morison method for the given wave directions. Also, the magnitude of motions at the mid-length tends to decrease as the wave direction decreases.
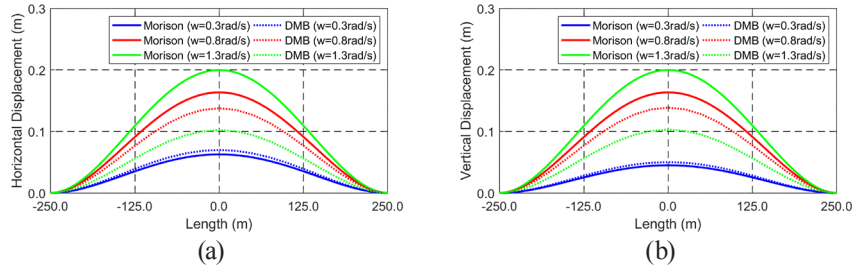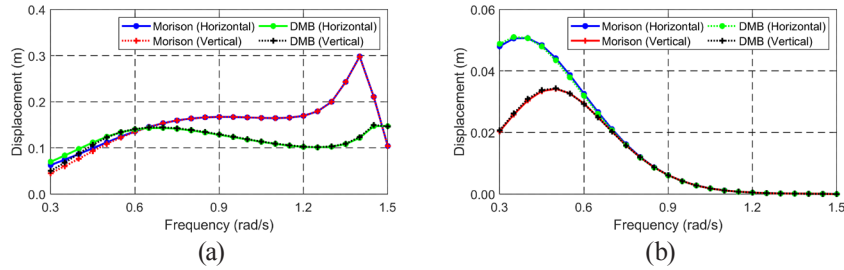

Figure 7. Amplitude envelopes of horizontal (a) and vertical (b) displacements (diameter of 0.2 m; submergence depth of 0.2 m; wave direction of 90°).

Figure 8. Amplitude of displacements at the mid-length and submergence depths of 20 m (a) and 60 m (b) (diameter of 0.2 m; wave direction of 90°).
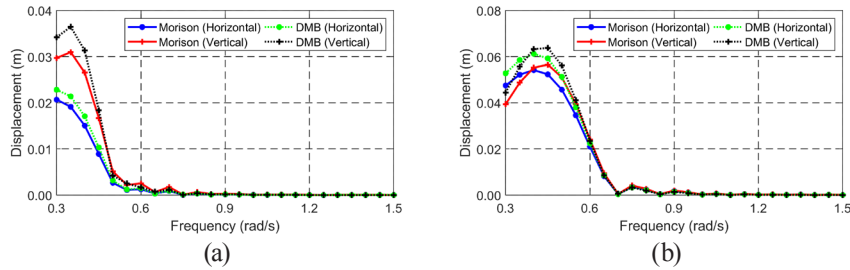
Figure 9. Amplitude of displacements at the mid-length and wave directions of 30° (a) and 60 ° (b) (diameter of 0.2 m; submergence depth of 0.2 m).

5. Conclusions

This study focuses on the hydro-elastic behaviors of a fully submerged horizontal cylinder in regular waves. The frequency-domain discrete-module-beam (DMB) method was developed; a continuous elastic floating structure is discretized into a certain number of rigid bodies while structural flexibility is modeled by beam elements with Euler-Bernoulli beam and Saint-Venant torsion; the hydrodynamic coefficients and wave forces were obtained from 3D potential theory. The time-domain Morison method was also employed; the Morison equation estimates wave forces and elastic behaviors are represented by massless axial, bending, and torsional springs. Various parametric studies on the cylinder diameter, submergence depth, and wave direction were conducted, and wave forces, dry/wet mode shapes/natural frequencies, and dynamic motions were analyzed. The results derived from this study are as follows:

(1) The presence of free surface tends to change the scattered wave force in the DMB model; the larger the diameter and the smaller the submergence depth, the greater the change in the scattered wave force. The overestimation of wave force in the high-frequency region is observed in the Morison model.

(2) Consideration of frequency-dependent added mass in the DMB method slightly changes the wet natural frequencies, whereas wet mode shapes of the two approaches are almost the same.

(3) The difference of wave forces and wet natural frequencies results in significant changes in the overall magnitudes of the dynamic motions. In this example, the Morison model tends to significantly overestimate dynamic motions around the fundamental wet natural frequency.

(4) Dynamics motions decrease with decreased wave direction, and high-frequency motion is reduced mainly due to the arrival time lag of incoming waves along the length, which induces phase cancellation of wave force.

Conflict of Interest

Author declares that there is no conflict of interest.

References

[1] Anastasopoulos, I., Gerolymos, N., Drosos, V., et al., 2007. Nonlinear response of deep immersed tunnel to strong seismic shaking. Journal of Geotechnical and Geoenvironmental Engineering. 133(9), 1067-1090.

[2] Chandrasekaran, S., Nannaware, M., 2014. Response analyses of offshore triceratops to seismic activities. Ships and Offshore Structures. 9(6), 633-642.

[3] Zhao, E., Dong, Y., Tang, Y., et al., 2021. Numerical investigation of hydrodynamic characteristics and local scour mechanism around submarine pipelines under joint effect of solitary waves and currents. Ocean Engineering. 222, 108553.

[4] Wang, Z., Yang, H., 2016. Parametric instability of a submerged floating pipeline between two floating structures under combined vortex excitations. Applied Ocean Research. 59, 265-273.

[5] Jin, C., Kim, M.H., 2018. Time-domain hydro-elastic analysis of a SFT (submerged floating tunnel) with mooring lines under extreme wave and seismic excitations. Applied Sciences. 8(12), 2386.

[6] Zou, P., Bricker, J.D., Chen, L., et al., 2022. Response of a submerged floating tunnel subject to flow-induced vibration. Engineering Structures. 253, 113809.

[7] Deng, S., Ren, H., Xu, Y., et al., 2020. Experimental study on the drag forces on a twin-tube submerged floating tunnel segment model in current. Applied Ocean Research. 104, 102326.

[8] Won, D., Seo, J., Park, J.S., et al., 2020. Internal force evaluation of a submerged floating pipeline under irregular waves. Journal of Marine Science and Technology. 28(6), 13.

[9] Nagavinothini, R., Chandrasekaran, S., 2020. Dynamic response of offshore triceratops with elliptical buoyant legs. Innovative Infrastructure Solutions. 5(2), 1-14.

[10] Morison, J., Johnson, J., Schaaf, S., 1950. The force exerted by surface waves on piles. Journal of Petroleum Technology. 2(05), 149-154.

[11] Lin, H., Xiang, Y., Yang, Y., et al., 2018. Dynamic response analysis for submerged floating tunnel due to fluid-vehicle-tunnel interaction. Ocean Engineering. 166, 290-301.

[12] Jin, C., Bakti, F.P., Kim, M., 2021. Time-domain coupled dynamic simulation for SFT-mooring-train interaction in waves and earthquakes. Marine Structures. 75, 102883.

[13] Muhammad, N., Ullah, Z., Choi, D.H., 2017. Performance evaluation of submerged floating tunnel subjected to hydrodynamic and seismic excitations. Applied Sciences. 7(11), 1122.

[14] Jin, C., Kim, S.J., Kim, M., 2021. Coupled time-domain hydro-elastic simulation for submerged floating tunnel under wave excitations. International Conference on Offshore Mechanics and Arctic Engineering. V006T006A023.

[15] Chakrabarti, S.K., Tam, W.A., 1975. Interaction of waves with large vertical cylinder. Journal of Ship Research. 19(01), 23-33.

[16] Chung, J.S., 2018. Morison equation in practice and hydrodynamic validity. International Journal of Offshore and Polar Engineering. 28(01), 11-18.

[17] Chang, S., Huang, W., Sun, H., et al., 2019. Numerical investigation of secondary load cycle and ringing response of a vertical cylinder. Applied Ocean Research. 91, 101872.

[18] Chandrasekaran, S., Jain, A., Gupta, A., 2007. Influence of wave approach angle on TLP's response. Ocean Engineering. 34(8-9), 1322-1327.

[19] Li, Y.S., Zhan, S., Lau, S., 1997. In-line response of a horizontal cylinder in regular and random waves. Journal of fluids and structures. 11(1), 73-87.

[20] Chen, B., Lu, L., Greated, C.A., et al., 2015. Investigation of wave forces on partially submerged horizontal cylinders by numerical simulation. Ocean Engineering. 107, 23-31.

[21] Jin, C., Kim, M., 2021. The effect of key design parameters on the global performance of submerged floating tunnel under target wave and earthquake excitations. CMES-Computer Modeling in Engineering & Sciences. 128(1), 315-337.

[22] Bakti, F.P., Jin, C., Kim, M.H., 2021. Practical approach of linear hydro-elasticity effect on vessel with forward speed in the frequency domain. Journal of Fluids and Structures. 101, 103204.

[23] Lu, D., Fu, S., Zhang, X., et al., 2016. A method to estimate the hydroelastic behaviour of VLFS based on multi-rigid-body dynamics and beam bending. Ships and Offshore Structures. 14(4), 354-362.

[24] Wei, W., Fu, S., Moan, T., et al., 2017. A discrete-modules-based frequency domain hydroelasticity method for floating structures in inhomogeneous sea conditions. Journal of Fluids and Structures. 74, 321-339.

[25] Jin, C., Bakti, F.P., Kim, M., 2020. Multi-floater-mooring coupled time-domain hydro-elastic analysis in regular and irregular waves. Applied Ocean Research. 101, 102276.

[26] Orcina, 2020. OrcaFlex User Manual Version 11.0 d.

[27] Faltinsen, O., 1993 Sea loads on ships and offshore structures. London, UK: Cambridge university press.

ARTICLE

Structural Integrity Analysis of Containers Lost at Sea Using Finite Element Method

Selda Oterkus[1] **Bingquan Wang**[1] **Erkan Oterkus**[1*] **Yakubu Kasimu Galadima**[1] **Margot Cocard**[1]
Stefanos Mokas[2] **Jami Buckley**[2] **Callum McCullough**[3] **Dhruv Boruah**[4] **Bob Gilchrist**[4]

1. PeriDynamics Research Centre, Department of Naval Architecture, Ocean and Marine Engineering, University of Strathclyde, Glasgow, UK
2. Buckley Yacht Design Ltd, New Milton, UK
3. M Subs Limited, Plymouth, UK
4. Oceanways Technologies Ltd, London, UK

ARTICLE INFO

ABSTRACT

Unlike traditional transportation, container transportation is a relatively new logistics transportation mode. Shipping containers lost at sea have raised safety concerns. In this study, finite element analysis of containers subjected to hydrostatic pressure, using commercial software ANSYS APDL was performed. A computer model that can reasonably predict the state of an ISO cargo shipping container was developed. The von Mises stress distribution of the container was determined and the yield strength was adopted as the failure criterion. Numerical investigations showed that the conventional ship container cannot withstand hydrostatic pressure in deep water conditions. A strengthened container option was considered for the container to retain its structural integrity in water conditions.

1. Introduction

As a light steel structure, containers have many advantages in ocean transportation. Container transportation reduces the number of manual loading and unloading, and handling in traditional transportation methods, which can avoid cargo damage, wet damage, and loss caused by human and natural factors. Therefore, the shipping container transportation method has completely replaced the traditional shipping method and has become a new and highly efficient transportation method [1].

Container transportation has revolutionized the transportation of goods by sea and has become the global standard for transportation of goods in the world today.

---

*Corresponding Author:
Erkan Oterkus,
PeriDynamics Research Centre, Department of Naval Architecture, Ocean and Marine Engineering, University of Strathclyde, Glasgow, UK;
Email: erkan.oterkus@strath.ac.uk*

Although containers simplify the transportation of large quantities of goods, many accidents still occur during transportation, causing a large number of containers to be lost during sea transportation. The World Shipping Council's 2020 Sea Container Lost Report shows that an average of 1,382 containers are lost at sea each year [2]. According to "Safety and Shipping Review" by Allianz. Although it is not uncommon for containers to be lost at sea, the risks of bad weather, improper stowage and strapping, and even the resulting environmental issues have caused people to pay additional attention to the issue of container loss [3].

Containers are usually manufactured in factories, transported to the construction site, and assembled quickly [4]. Due to the rapid increase in the use of freight containers for marine cargo and the development of special container ships, the safety of containerization in marine transport has been considered by International Organization for Standardization (ISO). Consequently, International Convention for Safe Containers (CSC) was introduced which aims to sustain a high level of safety of human life and facilitate international transport of containers by providing uniform international safety regulations [5].

There have been various studies available in the literature which considers the structural analysis of containers. Giriunas et al. [6] have investigated the ISO shipping container's structural strength for non-shipping applications. Antoniou and Oterkus [7] proposed origami based design concepts which can improve the structural efficiency of a container by FEM. An analytical, numerical, and experimental work on the in-plane stiffness of container buildings has been carried by Zha and Zuo [4]. They presented a feasible design and construction of the container. However, there is no study available in the literature which investigates the state of the containers lost at sea.

The main goal of this study is to analyse structural integrity of the International Organization for Standardization (ISO) shipping containers lost at sea. The construction standards of containers are presented. The structural response of shipping container subjected to underwater hydrostatic loading conditions is investigated. The von Mises stress distribution on a container at various water depths is demonstrated. Strengthened container option to withstand higher hydrostatic pressures is investigated.

2. Methodology

2.1 Finite Element Method

In this study, a standard shipping container model was constructed and analysed by using finite element method. For numerical calculations, ANSYS, a commercial finite element software, was utilised. The container is subjected to hydrostatic pressure around all surfaces, which represents the state of the container lost at sea. The thickness of the side and top walls of the container is significantly smaller compared to its length and width. Consequently, the container was discretized by shell elements in the finite element model. The thickness of the plates can be defined through the section property definition.

The element type, SHELL181, used in this work is widely used to simulate shell structures with thin to medium thickness. As presented in Figure 1, it is a four-node element with six degrees of freedom at each node which are translations in the x, y, and z directions, and rotations about the x, y, and z-axes.
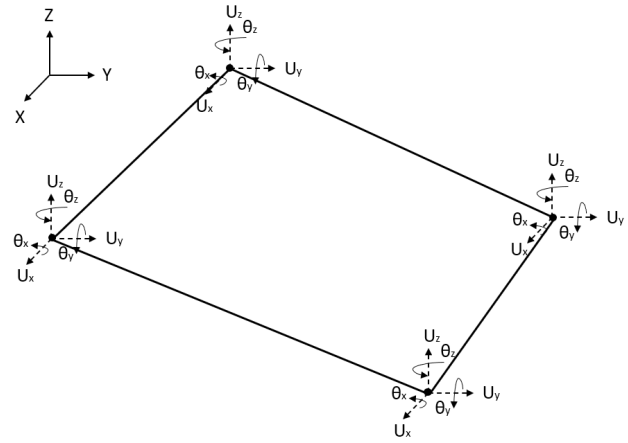
Figure 1. SHELL181 Geometry and Its Nodal Degrees of Freedom.

2.2 Failure Criterion

In this study, the structural integrity of the container was examined by using the von Mises yield criterion. It was assumed that if the von Mises stress of the container subjected to hydrostatic loading is equal or greater than the yield limit of the construction material, then the container will damage.

The stress state at a point can be defined by a 3×3 tensor for a three-dimensional model as

$$\begin{bmatrix} \sigma_{xx} & \sigma_{xy} & \sigma_{xz} \\ \sigma_{xy} & \sigma_{yy} & \sigma_{yz} \\ \sigma_{xz} & \sigma_{yz} & \sigma_{zz} \end{bmatrix} \tag{1}$$

where σ_{xx}, σ_{yy}, σ_{zz} are normal stresses and σ_{xy}, σ_{xz}, σ_{yz} are shear stresses. Von Mises stress σ_v combines the stress components or principal stresses into equivalent stress. In terms of stress components given in Equation (1), it can be calculated as [8]

$$\sigma_v = \sqrt{\frac{(\sigma_{xx} - \sigma_{yy})^2 + (\sigma_{yy} - \sigma_{zz})^2 + (\sigma_{zz} - \sigma_{xx})^2 + 6(\sigma_{xy}^2 + \sigma_{yz}^2 + \sigma_{zx}^2)}{2}} \tag{2}$$

In terms of principal stresses, it can be expressed as [8]

$$\sqrt{\frac{(\sigma_1 - \sigma_2)^2 + (\sigma_2 - \sigma_3)^2 + (\sigma_3 - \sigma_2)^2}{2}} \qquad (3)$$

in which σ_1, σ_2 and σ_3 are principal stresses.

3. Container Geometry Model

Depending on the types of goods that their containers are carrying, ISO and CSC stipulate specifications related with structural strength, applicability, and application of shipping containers. According to the guidance based on ISO, CSC, and container manufacturer standards, the dimensions of the most common 20 ft container are shown in Table 1 and Figure 2.

Table 1. The geometrical dimensions of a 20 ft container

|	Length L	Width W	Height H
20 ft container	6090 mm	2440 mm	2590 mm
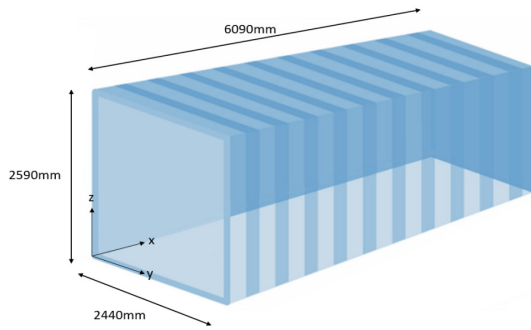
Figure 2. Dimensions of a 20 ft shipping container.

The container was designed and constructed for the transportation of general cargo on sea. The main components of the container in this work focused on the side walls, end walls and the roof of the container. The trapezium section sidewall is built with 9Pcs 2.6 mm thick fully vertically continuous corrugated steel panels at the intermediate area and 2Pcs 2.6 mm thick fully vertically continuous corrugated steel panels at both ends. The top to bottom view of the side wall is presented in Figure 3.
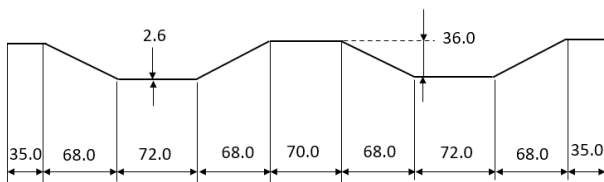
Figure 3. Top to bottom view of the side wall.

The trapezium section end wall in Figure 4 was constructed with 2.6 mm thick vertically corrugated steel panels, which are butt welded together to form one panel.
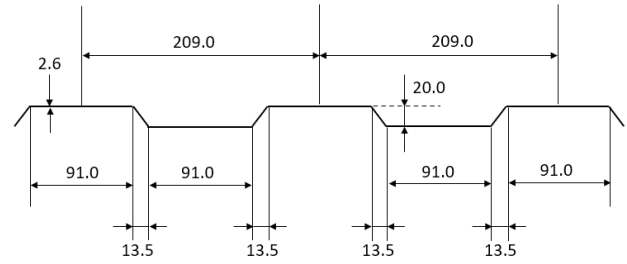

Figure 4. Top to bottom view of the end wall.

The roof was constructed by several die-stamp corrugated steel sheets with a certain upwards camber at the centre of each trough and corrugation while the floor of the container was constructed as a flat sheet.

4. Numerical Evaluation

Finite element software Ansys Mechanical APDL was performed for finite element analysis in this study. The considered container shown in Figure 5 was constructed based on the geometry from Table 1. The side walls are constructed based on the dimensions provided in Figure 3 and Figure 4, respectively.
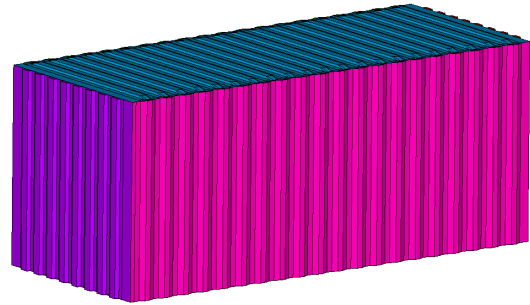
Figure 5. The model geometry of the container.

The container components are typically constructed with steel plate. The density ρ, elastic modulus E and Poisson's ratio v of the model are specified as $\rho = 7850$ **kg/m³**, $E = 200$ **Gpa**, and $v = 0.3$. The material parameter and constitutive relationship of the container model varies depend on the material selected as three types of widely used metal material was considered in the construction. Table 2 indicates material properties of these three material types including ASTM A283 carbon steel [9], SPA-H steel [10] and HY-100 [11] steel.

Table 2. Material parameters of container model

Material Type	Yield Strength σ_{yield}(Mpa)	Ultimate Strength σ_s(Mpa)
ASTM A283	165	310
SPA-H	457	572
HY-100	744	1062

13

The element size, element shape and mesh type of each component in the container model are specified in Table 3. It is worth noting that to make sure that all components are connected to each other. It is important to merge co-incident nodes after the mesh generation is completed, which can tie separate but coincident parts of the model together.
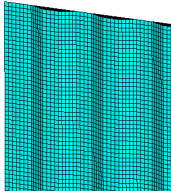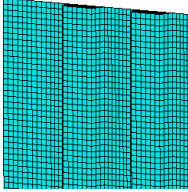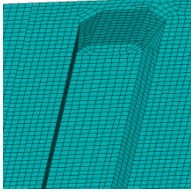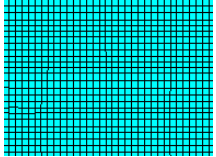
The container model is considered in the occasions of falling and lost at sea during the operation caused by the un-expected sea state (Figure 6). The container is subjected to hydrostatic pressure. Defining the density of the seawater as ρ_s =1025 $\mathbf{kg/m^3}$, the state of the container was investigated at different water depths. The pressure values at different water depths are shown in Table 4. The pressure loading is applied on all surfaces of the container model in the analysis. In finite element model, the hydrostatic pressure was considered as surface loads and applied on nodes.
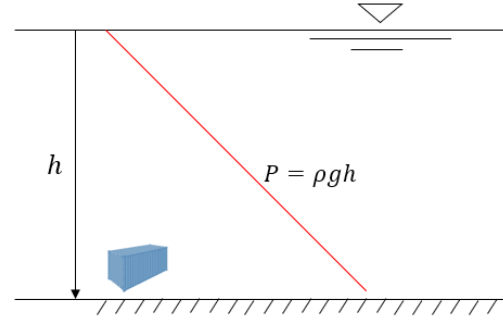
Figure 6. Schematic drawing of container lost at sea and associated hydrostatic pressure acting on it.

The constrained displacements were applied as boundary conditions on the container model to prevent rigid body motion. In addition to hydrostatic pressure acted on all surfaces of the container components, the constrained displacements on the container surface were specified as

Table 3. The details of the finite element model of the container

Component	Side Wall	End Wall	Top Roof	Bottom Floor
Mesh Form				
Element Type	Shell 181			
Size	18 mm	18 mm	10 mm	14 mm
Mesh Type	Structured	Structured	Structured	Structured
Thickness	2.6 mm	2.6 mm	3 mm	20 mm

Table 4. Hydrostatic pressure at different water depths.

Depth (m)	Pressure (Pa)
5	50276.25
15	150828.75
30	301657.5
50	502762.5

$$u_x\left(x=\frac{L}{2},y=0,z=\frac{H}{2}\right)=u_z\left(x=\frac{L}{2},y=0,z=\frac{H}{2}\right)=0 \quad (4)$$

$$u_x\left(x=\frac{L}{2},y=W,z=\frac{H}{2}\right)=u_z\left(x=\frac{L}{2},y=W,z=\frac{H}{2}\right)=0 \quad (5)$$

$$u_x\left(x=\frac{L}{2},y=\frac{W}{2},z=H\right)=u_y\left(x=\frac{L}{2},y=\frac{W}{2},z=H\right)=0 \quad (6)$$

$$u_x\left(x=\frac{L}{2},y=\frac{W}{2},z=0\right)=u_y\left(x=\frac{L}{2},y=\frac{W}{2},z=0\right)=0 \quad (7)$$

in which u_x, u_y and u_z are the displacements in x, y and z directions, respectively.

5. Results and Discussion

The von Mises stress distribution on the container at considered depths is presented in Figure 7. High von Mises stresses can be observed in the middle of the sidewalls. Moreover, a relatively high von Mises stress distribution is shown on the edges of the container model. According to the failure criterion defined by the yield strength and considered construction materials in Table 2, the maximum von Mises stress observed on the container exceeds the yield strength at all water depths. Therefore, the watertightness and structural integrity cannot be maintained after conventional shipping containers are lost at sea.

Based on the conclusion from the comparison, the container needs to be strengthened to withstand hydrostatic pressure. Considering the containers are designed to be heavily loaded and stacked with other containers, it is not feasible to change the geometrical design of the container as this will cause the re-designed container incompatible

with other containers operating in the market. However, the container strength can be improved by increasing the thickness of the sidewalls or alternative construction material. Therefore, in the second case study, the container model components have been redesigned with a different thickness. The new thickness assigned to each component is shown in Table 5. The second case has identical mesh configuration, loading conditions, and constrained displacements with the formal case.

Table 5. The thickness of re-designed container components

Component	Side Wall	End Wall	Top Roof	Bottom Floor
Thickness	22 mm	22 mm	26 mm	30 mm

Figure 8 presents the distribution of von Mises stress of the re-designed container. The comparison between maximum von Mises stress at various depths and yield strength for selected materials is shown in Figure 9. The maximum von Mises stress of the container model is lower than the yield strength of all three materials considered in this study. Thus, the new container design can retain the structural integrity of the container in deeper water conditions.

Table 6 compares the effect of thickness on the maximum von Mises stress between the original and thickened container at different water depths. It can be observed that the thickened container significantly reduces the maximum von Mises stress when subjected to the same hydrostatic pressure conditions as the conventional container.

(a)

(b)

(c)

(d)
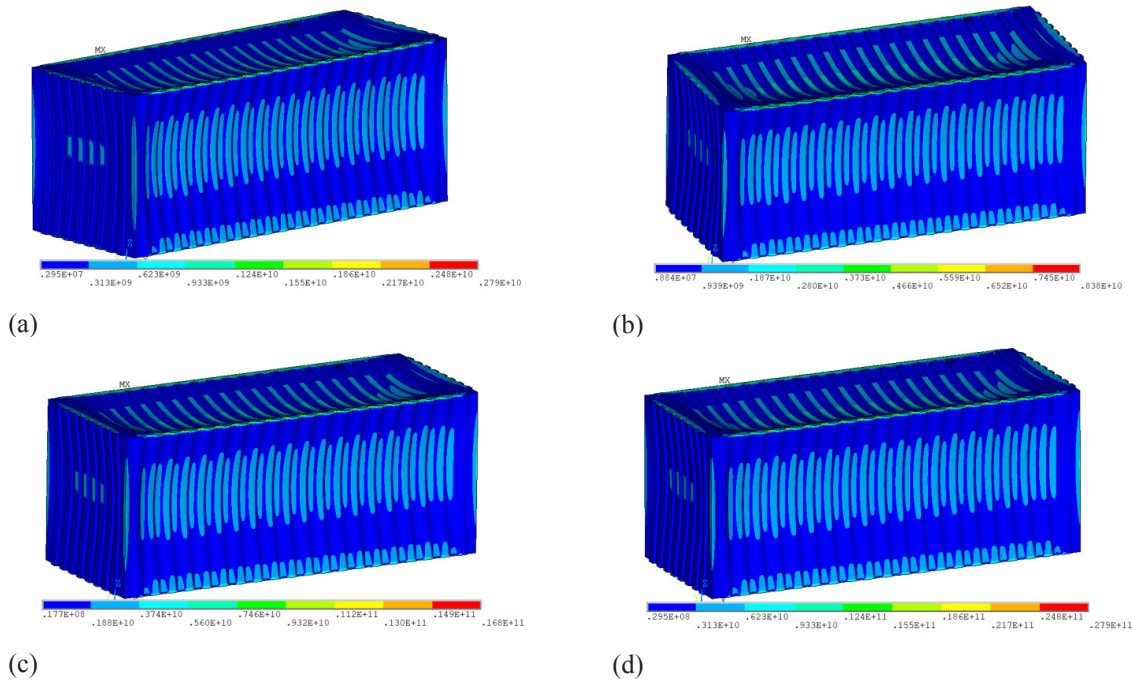
Figure 7. von Mises stress distribution on the container at (a) 5 m, (b) 15 m, (c) 30 m,(d) 50 m water depths.
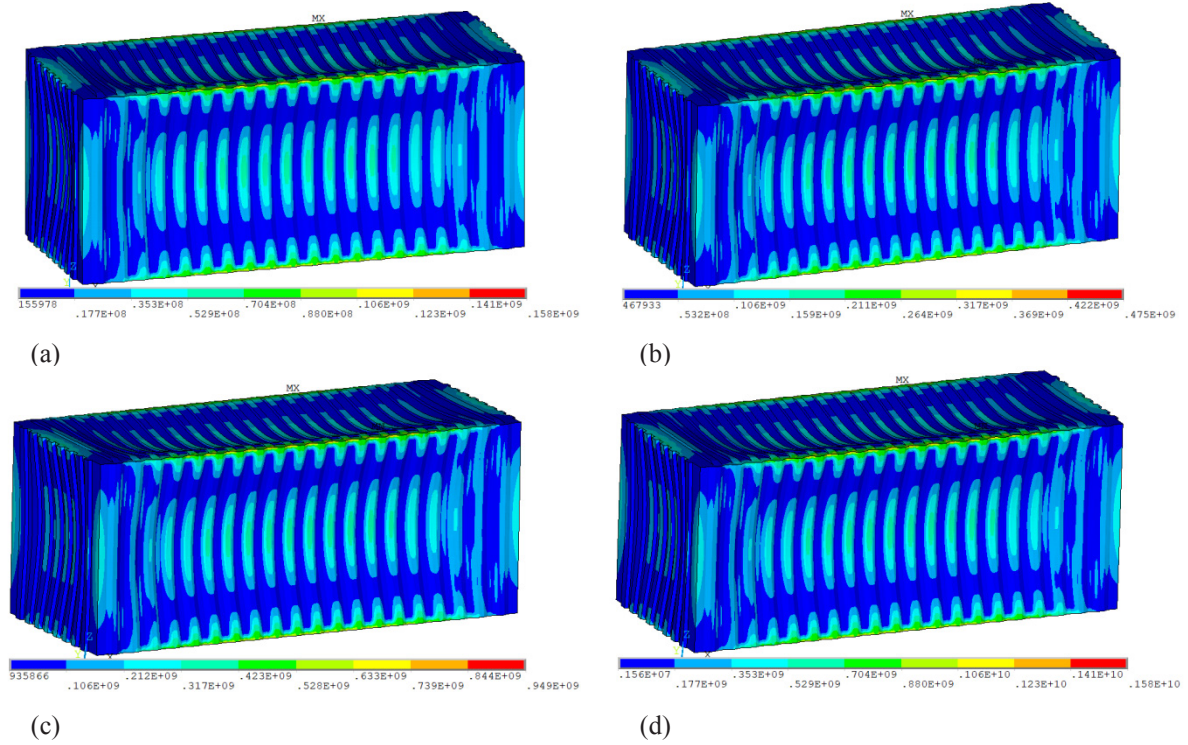
Figure 8. von Mises stress distribution of re-designed container at (a) 5 m,(b) 15 m,(c) 30 m,(d) 50 m.
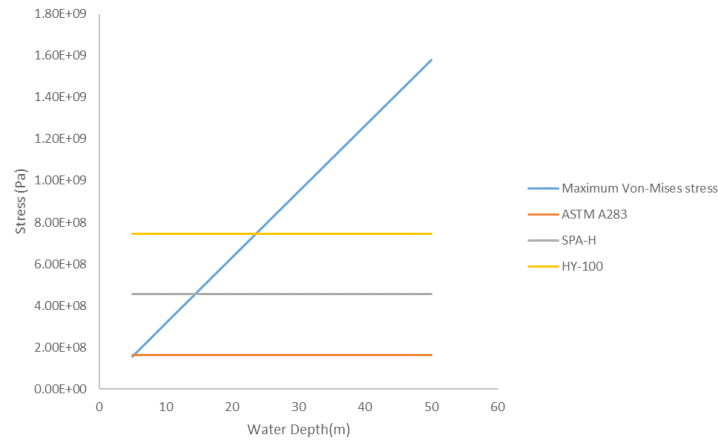
Figure 9. The comparison between maximum Von-Mises stress at various depths and yield strength.

Table 6. The effect of thickness on maximum Von Mises stress

Water Depth	Original Configuration	Thicker Configuration	Stress Reduction
5 m	2.79E9 Pa	1.58E8 Pa	94%
15 m	8.38E9 Pa	4.75E8 Pa	94%
30 m	1.68E10 Pa	9.49E8 Pa	94%
50 m	2.79E10 Pa	1.59E9 Pa	94%

6. Summary and Conclusions

In this study, finite element analysis was conducted to investigate the structural behaviour of shipping containers lost at sea. Three different construction materials were discussed for conventional size containers. von Mises stress was employed as a failure criterion. The hydrostatic pressure was increased with the water depth. For containers constructed with traditional configuration, the container lost its structural integrity in shallow water very quickly. The increased thickness reduced the von Mises stress and made the container to retain its structural integrity at a deeper water level.

Unpredictable weather conditions and low operational risk awareness could cause shipping containers to be lost at sea. Increasing the thickness of the container sidewall will increase production costs, but if the structure is damaged when fell into the water, the consigned goods may spread out in the sea and float. Floating containers and consignments could pose a risk of collision with small ocean-going vessels such as yachts and fishing boats. Moreover, if the container contains dangerous goods that may cause risk to the ecological environment, it is even more important to maintain the structural integrity of the container when it falls into the water to prevent any type of pollution. As an alternative solution to traditional container shipping, commercial type cargo submarines can be utilised especially for short distances.

Acknowledgement

Conflict of Interest

There is no conflict of interest.

References

[1] Lee, C.Y., Song, D.P., 2017. Ocean container transport in global supply chains: Overview and research opportunities. Transportation Research Part B: Methodological. 95, 442-474.

[2] The International Institute of Marine Surveying (IIMS), 2020. World Shipping Council containers lost at sea 2020 report issued and shows a decrease. [online] Available at: <https://www.iims.org.uk/world-shipping-council-containers-lost-at-sea-2020-report-issued-and-shows-a-decrease/> (Accessed 29 December 2021).

[3] Allianz, 2021. Safety and Shipping Review. An annual review of trends and developments in shipping losses and safety.

[4] Zha, X., Zuo, Y., 2016. Theoretical and experimental studies on in-plane stiffness of integrated container structure. Advances in Mechanical Engineering. 8(3), 1687814016637522.

[5] CSC, 1996. International convention for safe containers.

[6] Giriunas, K., Sezen, H., Dupaix, R.B., 2012. Evaluation, modeling, and analysis of shipping container building structures. Engineering Structures. 43, 48-57.

[7] Antoniou, K., Oterkus, E., 2019. Origami influence on container design. *A*nnals of Limnology and Oceanography. 4(1), 015-019.

[8] Timoshenko, S.P., Goodier, J.N., 1951. Theory of elasticity.

[9] ASTM International, 2013. ASTM A283/A283M-13-Standard Specification for Low and Intermediate Tensile Strength Carbon Steel Plates.

[10] Akkaş, N., 2017. Welding time effect on tensile-shear loading in resistance spot welding of SPA-H weathering steel sheets used in railway vehicles. Acta Physica Polonica A. 131(1), 52-54.

[11] Zarzour, J.F., Konkol, P.J., Dong, H., 1996. Stress-strain characteristics of the heat-affected zone in an HY-100 weldment as determined by microindentation testing. Materials characterization. 37(4), 195-209.

Sustainable Marine Structures

https://ojs.nassg.org/index.php/sms

ARTICLE

Dynamic Analysis of Splash-zone Crossing Operation for a Subsea Template

Adham M. Amer[1]   Lin Li[1]*   Xinying Zhu[2]

1. Department of Mechanical and Structural Engineering and Materials Science, University of Stavanger, Norway
2. Havfram AS, Stavanger, Norway

ABSTRACT

Subsea templates are steel structures used to support subsea well components. Normally, offshore crane vessels are employed to install them to the target location on the seabed. Crossing the splash-zone during the lowering of a subsea template is considered the most critical phase during the installation due to slamming loads and needs to be studied to provide the operational weather criterion during the planning phase. In this study, dynamic response analysis has been carried out to evaluate the allowable sea states for the plash-zone crossing phase of the subsea templates. The numerical model of the lifting system, including the crane vessel and the subsea template, is firstly built in the state-of-the-art numerical program SIMA-SIMO. Then, dynamic analysis with time-domain simulations is carried out for the lifting system under various sea states. The disturbed wave field due to the shielding effects from the installation vessel is considered when calculating the hydrodynamic forces on the template. Statistical modelling of the dynamic responses from different wave realizations is used to estimate the extreme responses of various sea states. The application of the generalized extreme value distribution and Gumbel distribution in fitting the extreme responses is discussed. Moreover, the influence of the shielding effects from the vessel, as well as the influence of the changing size of the suction anchor on the hydrodynamic responses and the allowable sea states are studied.

1. Introduction

The lowering operation of subsea assets through the wave splash-zone is considered the critical phase during an offshore installation process. The combined high costs and sensitivity of the operation to weather conditions reduce the possibilities to correct errors during the installation process. The consequence of the failure of the operation is significant. Thus, numerical modelling of the installation system is required during the planning phase to tackle both the uncertainties and high risks involved in such operations. Various numerical studies have been performed to analyze the dynamic responses of lifting operations when the lifted objects cross the splash-zone. These stud-

---

*Corresponding Author:
Lin Li,
Department of Mechanical and Structural Engineering and Materials Science, University of Stavanger, Norway;
Email: lin.li@uis.no

ies addressed the dynamic responses during the installation of different subsea assets such as subsea trees [1], manifolds [2,3], templates [4], suction anchors [5], and spools [6]. In a typical offshore lowering operation, the vessel hull is used to shield the lowered asset from the incident waves. The hull diffracts the incoming waves and reduces the overall dynamic forces acting on the subsea asset as the lowering takes place. This phenomenon is known as shielding effect. Developing an adequate numerical model to account for shielding effect requires an accurate calculation of the diffracted wave data around the installation vessel. Several studies proposed numerical approaches to consider the shielding effect from the installation vessel while lowering subsea assets, such as monopiles and spools, through splash-zone [6,7].

Performing time-domain simulations for the lowering system is a common approach to carry out such numerical studies. The numerical modelling requires a proper estimation of the hydrodynamic loads acting on the marine structure. Generally, this needs an accurate estimation of both added mass and damping coefficients of the submerged structural members [8,9]. The estimation of these coefficients is quite challenging, especially when perforated elements such as suction anchors are considered.

Lifting operations within a limited duration are often classified as weather-restricted operations. For such operations, it is required to establish the operational limits during the planning phases. For marine lifting operations sensitive to wave loads, these limits are often given as functions of significant wave height (Hs), spectral peak period (Tp), wave direction, etc. In similar studies, operational limits are obtained through numerical simulations, model tests, field measurements, offshore observations, or a combination of what previously mentioned [10]. Among them, numerical simulations are less expensive and are mostly applied to study the critical responses during operations and compare the dynamic responses with the operational criteria to provide the operational limits [11].

This study focuses on the lifting operation of a subsea template. Subsea templates are used to provide guidance and support for well drilling equipment and other completion activity taking place on the seabed. They also act as supporting frames for other subsea production system components, including manifolds, risers, and wellheads. Subsea templates are normally installed by a floating crane vessel at a deep offshore site [12]. The installation process of subsea templates consists of different phases. First, the template is over-boarded by the installation vessel. After being lifted-off from the deck of the installation vessel, the template is lowered through the wave splash-zone. Finally, the template is further submerged until it reaches the seabed. A typical subsea template usually has four suction anchors. Due to the large cross-sectional area of the anchors, the template experiences high hydrodynamic loads when crossing the splash-zone. Furthermore, the dynamic features of such operations undergo continuous changes and are dominated by non-linear responses. Thus, the prediction of the motion responses and the estimation of the slamming loads on the subsea template in the wave zone can be quite challenging. Several numerical studies were conducted to capture the dynamic responses when lowering subsea structures through the splash-zone [1,2,5,6, 13-16].

According to DNV standards, several operational criteria shall be considered during the splash-zone crossing phase of the lifting operation [9]. The first criterion is to evaluate the potential for damage to the lowered object due to the slamming loads. The other criterion is on the potential for snapping forces acting on the lift wire and slings due to the slack limit being reached. Here, the snap force is defined as a dynamic force within a short duration, which is associated with any sudden changes within the lifted object velocity [17].

This paper presents a numerical study on the splash-zone crossing operation for a subsea template. The installation system and the numerical model used in this study are firstly introduced. Then, a validation of the numerical results with actual field measurements is performed. Next, the operation acceptance criteria and the statistical models used to assess the allowable sea states are given, followed by time-domain and eigen value analysis of the numerical model. Lastly, the dynamic responses and the allowable sea states for different sensitivity studies are presented with detailed discussions.

2. The Installation System and the Numerical Model

The lifting system consists of two main bodies the installation vessel and the subsea template. A typical offshore installation vessel is used for the operation [6], and the vessel technical specifications are presented in Table 1.

Table 1. Installation vessel technical specifications.

Item	Unit	Value
Overall length	[m]	156.7
Overall breadth	[m]	27
Displacement at maximum draft	[ton]	1.70E4
Maximum draft	[m]	8.5
Crane maximum lift capacity	[ton]	400
Crane operating radius	[m]	10 - 40

A typical integrated template structure (ITS) is applied in the numerical model [18], and the side and top views of the template can be found in Figure 1. The template structure mainly consists of four hollow suction anchors, four hollow washout sleeves, and eight guideposts attached to the top of the template. The overall length and width of the subsea template are 20.8 m and 17.4 m, respectively, and the overall height from the top of the guideposts to the bottom of the anchors is 12.9 m. The total mass of the template is 263 tons. The mass of the template is distributed evenly at the four corners, making an easy four-sling arrangement for handling the template in the air and during the lowering operation into the water. The dimensions of the main elements of the template are presented in Table 2.

Table 2. Subsea template dimensions and specifications.

Item	Unit	Value
Overall height	[m]	12.9
Overall length	[m]	20.8
Overall width	[m]	17.4
Mass in air	[ton]	263
Outer diameter of the suction anchors	[m]	5.5
Outer diameter of the washout sleeves	[m]	0.98
Wall thickness (suction anchors and washout sleeves)	[m]	0.02
Height of the suction anchors height	[m]	8.225
Height of the washout sleeves	[m]	7.725
Carbon steel density	[kg/m³]	7850

The crane, crane lift wire, slings, and winch compose the hoisting system for the lifting operation of the template. Because of the large dimension of the template structure, four slings on top of the four suction anchors are applied to distribute the tension in the slings. The four slings connect the template to the hook of the crane block, and the lift wire connects the crane block and the crane tip. The slings maintain a fixed length during the installation process, while the main lifting wire increases in length as lowering takes place. The winch speed is normally kept at a low value during splash-zone crossing. For this study, the lowering speed of the winch is kept at 0.1 m/s.

2.1 Numerical Model

The numerical model has been built using the marine operation numerical program SIMA-SIMO [19]. The coupled numerical model consists of the installation vessel, the template, and the hook. Both the installation vessel and the template have six degrees of freedom (DOFs), and the hook only has three DOFs. The global coordinate system is highlighted in Figure 2. The origin is located at the free water surface, and the middle section of the installation vessel. The X-axis points towards the bow of the vessel, the Y-axis points towards the port side, and the Z-axis points upwards. The crane's operating radius is set to 18m during the operation. The established numerical model of the operating system is shown in Figure 2.

The wire couplings through four slings and the lift wire are modeled as linear springs. The axial stiffness, *k* can be expressed as:

Figure 1. Top and side views of the subsea template used in the numerical model.
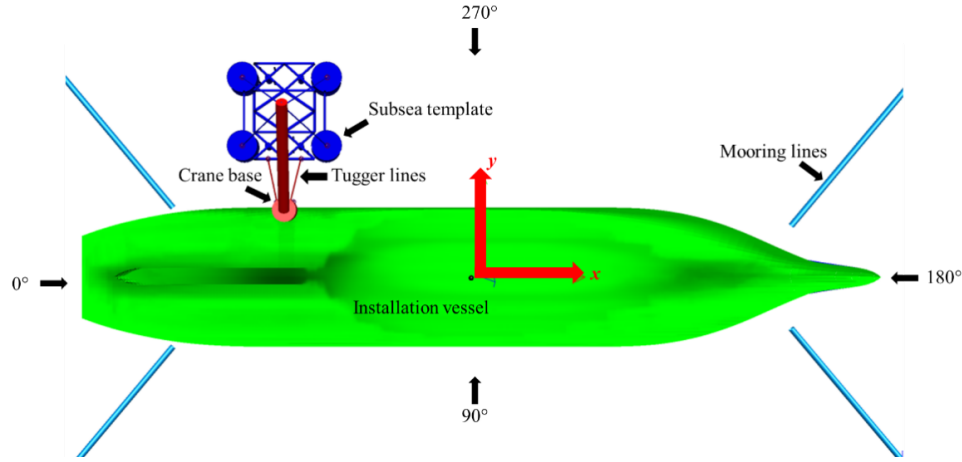
Figure 2. Coupled numerical model in SIMA-SIMA.

$$\frac{1}{k} = \frac{l}{EA} + \frac{1}{k_o} \tag{1}$$

where *EA* is the modulus of elasticity times the cross-sectional area of the wire; *l* is the effective length of the wire, and it changes for the main lift wire when the winch runs during the lowering operation. $1/k_o$ is the connection flexibility. The properties of the wires are chosen based on the practical operations, and they are given in Table 3.

Table 3. Properties for the lift wire and slings.

Item	Unit	Lifting Wire	Slings
Unstretched length	[m]	39.8	18.1
Connection flexibility	[m/N]	1.3e-07	1.3e-07
Damping	[Ns/m]	1.0e+07	6.16e+06
Axial stiffness EA	[N]	1.2e+09	3.08e+08
Breaking strength	[N]	1.3e+07	6.1e+06

Tugger lines are usually used in lowering operations to control the yaw motion of the template. In this study, a constant tension is applied to two crane tugger lines. Both lines are connected to the template structure and the crane base (see Figure 2). To illustrate the function of the tugger lines, the yaw motion of the template during the lowering phase with and without the two crane tugger lines is compared and shown in Figure 3 under the same sea state. A large increase in the template yaw angle from 0 to 140 degrees can be clearly observed without using any tugger lines. This large yaw is undesirable and should be avoided for a safe operation. By adding two tugger lines with 5 ton's tension in each line, the mean yaw angle of the template maintains around 0 deg, and less fluctuation in the yaw motion is seen after 300 s after the template crosses the splash zone. Thus, the tugger lines are important in the numerical model to avoid large yaw motion for the template during the whole lowering process.
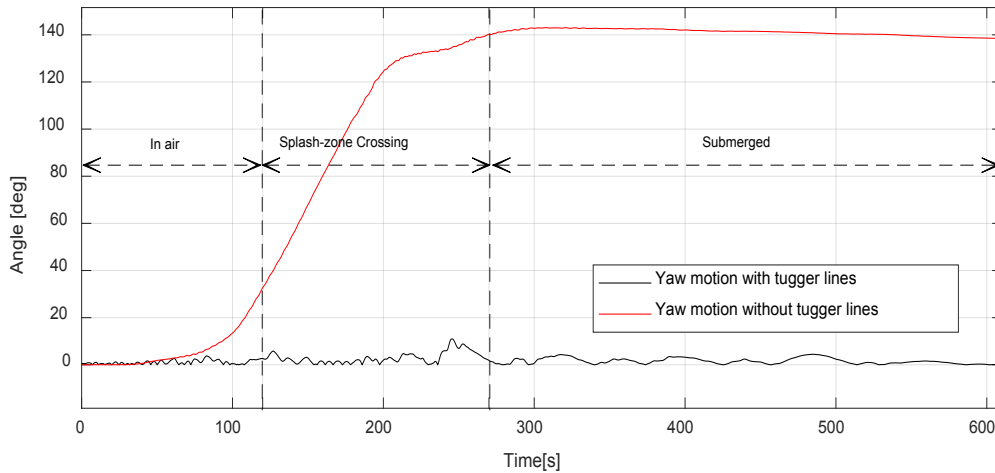
Figure 3. Template yaw motion at Hs = 2 m and Tp = 8 s.

Modeling of hydrodynamic forces on the template

The template is modeled in SIMA-SIMO using slender elements. The empirical Morison's formula is considered suitable to calculate hydrodynamic forces for slender elements with a D/L ratio (diameter over wavelength) much less than 0.2 [20]. Each slender element is divided into several strips. Based on Morison's equation, the wave force per unit length on each strip normal to the member, F_s, is given as follows:

$$F_s = \rho_w(1 + C_A)\frac{\pi D^2}{4}\ddot{\zeta}_s - \rho_w C_A \frac{\pi D^2}{4}\ddot{x}_s + \frac{1}{2}\rho_w C_q D|\dot{\zeta}_s - \dot{x}_s|.(\dot{\zeta}_s - \dot{x}_s) \quad (2)$$

where ρ_w is the fluid density; D is the outer diameter of the element; and C_A and C_q are the added mass and quadratic drag force coefficients, respectively. $\ddot{\zeta}_s$, $\dot{\zeta}_s$, $\ddot{x}_s$ and $\dot{x}_s$ are accelerations and velocities of the fluid and the element itself, respectively.

The reference volume when calculating the vertical added mass of one such anchor equals the volume of the entrapped water inside the cylinder plus the volume of a sphere with a radius equal to the radius of the anchor. This reference volume is illustrated in Figure 4. For the top hatches of the suction anchors, they are normally open in the actual operations, and thus a perforation effect for each suction anchor takes place. For the subsea template used in this study, a perforation percentage of 6% is accounted for each anchor. This percentage causes a reduction in the value of the vertical added mass according to the following expression [8],

$$A_{33} = A_{33o}\left(0.7 + 0.3\cos\left[\frac{\pi(p-5)}{34}\right]\right) \quad (3)$$

where A_{33} is the perforated vertical added mass, A_{33o} is the non-perforated vertical added mass, and p is the perforation ratio in percentage. If p is less than or equal to 5%, the vertical added mass is assumed to be non-perforated and A_{33} will be equal to A_{33o} in the previous formula.

The experimental study performed by Solaas and Sandvik (2017) is used to calculate the damping of the

suction anchor in the axial direction [21]. Free oscillation decay tests in the axial direction were performed for anchors with different height to diameter ratios and perforations to provide an accurate measurement of the hydrodynamic coefficients. These experiments concluded that for anchors with a perforation ratio of over 4%, the axial linear damping term is primary, and the quadratic damping term is secondary. Since the anchor used in this study has a perforation of 6%, only linear damping in the axial direction needs to be considered. Figure 5 includes the linear damping data of an anchor having a diameter of 5 m and a height of 8.9 m. By scaling the linear damping with the introduced anchor diameter in Table 2, the new vertical damping value can be estimated. The horizontal damping for each anchor is estimated according to DNVGL-RP-N103 recommended practice [8].

Three slender elements, namely the vertical, top, and bottom elements, are employed in SIMA-SIMO to distribute the hydrodynamic forces acting on each anchor. The inputs of each of these elements are presented in Table 4. The inputs are assigned in the elements local coordinate system in SIMO.

The vertical element, which has the same height as the anchor, is modeled to consider numerical properties including the structural mass, volume, lateral added mass, and damping. The lateral added mass (Ma_{La}) for the vertical element is set to be equal to the added mass of a cylinder normal to the flow plus the mass of the entrapped water inside the anchor (see Figure 4).

The element located at the top of the anchor is used to model the added mass caused by the water above the anchor roof and the damping due to the flow through the ventilation hatches at the top. Ma_{Ax} for the top element equals the perforated vertical added mass of the upper half of the water sphere divided by the element length (see Figure 4). The total perforated added mass is calculated from Equation (3). The quadratic drag components (D_{2La}) for the top and vertical elements are calculated based on the given guidelines in DNVGL-RP-N103 [8].
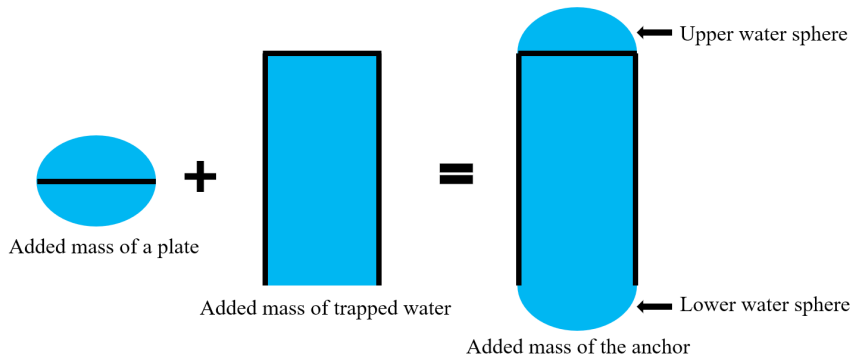
Figure 4. Illustration of the reference volume for the added mass of a suction anchor in the vertical direction.
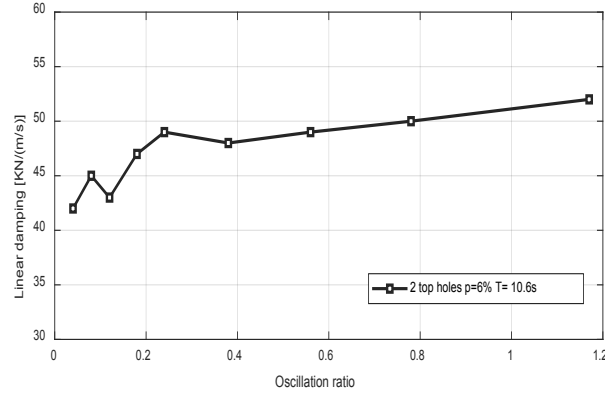
Figure 5. Axial linear damping of a suction anchor with two top holes and 6% perforation ration [21].

Table 4. Slender elements hydrodynamic coefficients input in SIMO.

|			Vertical element	Top element	Bottom element
Item	Description	Unit	Value	Value	Value
D_{2Ax}	Axial quadratic damping	Ns^2/m^3	-	-	-
D_{2La}	Lateral quadratic damping	Ns^2/m^3	5800	5800	-
D_{1Ax}	Axial linear damping	Ns/m^2	-	-	5.7e+05
Ma_{Ax}	Axial added mass	kg/m	-	2.32e+05	2.42e+06
Ma_{La}	Lateral added mass	kg/m	39910	39910	-

Another element in the numerical model located at the bottom of the anchor accounts for the hydrodynamic properties that generate slamming forces. The element is located at the bottom tip of the anchor to use the wave kinematics at the entrance of the anchor when calculating the slamming forces during time-domain simulations. Ma_{Ax} for the bottom element is the sum of the perforated vertical mass of the trapped water and the lower half of the water sphere divided by the element length. The element has a length of 0.1 m. The axial linear drag D_{1Ax} for the bottom element is estimated based on linear damping data presented in Figure 5. Depth-dependent coefficients (DDC) are used to ensure that the forces appear when the suction anchor roof touches the instantaneous water surface. The DDC used in this model are defined in Figure 6 and Table 5. RMa_{Ax} and RD_{1Ax} are the ratios of relative axial added mass and relative axial linear drag, respectively. Both terms are assigned in SIMO to control the development of both axial drag and added mass as the template gets submerged. The value is assigned between 0, which means that the hydrodynamic term is not yet developed, and 1 which means the hydrodynamic term is fully developed. Since the added mass is at its highest only when the roof of the anchor reaches the wave surface, RMa_{Ax} is set to 0 along the anchor length (position A to C). Once the anchor roof reaches the free water surface

(position D to E), the added mass starts developing from 0.9 to 1. As for RD_{1Ax}, a slight development of damping takes place when the bottom of the anchor touches the water surface (position B to C). Same as the added mass, the damping becomes fully developed from 0.8 to 1 when the anchor roof reaches the water surface (position D to E).
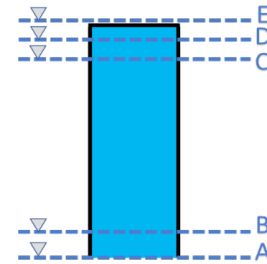
Figure 6. Depth-dependent coefficients activation levels for each anchor.

The total hydrodynamic calculations of the template, including the top structure, are presented in Table 6. The table clearly shows that most of the inertia forces are caused by the template total added mass. The total added mass in both axial and lateral directions is almost 5 times larger than the actual mass of the template. This significantly large added mass value may generate large slamming loads on the subsea template model when it crosses the splash-zone according to Equation (2).

Table 5. Depth-dependent coefficients inputs in SIMO

Position	Description	Anchor slender element vertical location in global coordinate [m]	RD_{1Ax}	RMa_{Ax}
A	anchor above water level	0	0	0
B	anchor penetrates water level	−0.1	0.1	0
C	anchor roof above water level	−8.025	0.1	0
D	anchor roof partially submerged	−8.125	0.8	0.9
E	anchor roof completely submerged	−8.225	1.0	1.0

Table 6. Total hydrodynamic calculation of the template

Item	Unit	Value
D_{2Ax}	kNs^2/m^2	64
D_{2La}	kNs^2/m^2	290
D_{1Ax}	kNs/m	57
Ma_{Ax}	ton	1152
Ma_{La}	ton	1381

2.2 Environmental Conditions

Disturbed wave kinematics

The wave field close to the vessel is different from incident waves when the construction vessel is present, and this disturbance of the wave field is known as "shielding effects". Because of this, the hydrodynamic forces on the subsea template are affected when it crosses the wave zone. To take into account the influence of the disturbed wave fields during the lowering operation, a numerical method was developed by interpolating the disturbed wave kinematics in both horizontal and vertical directions at each instance when calculating the hydrodynamic forces of a monopile during the lowering operation [22,23]. The same method was applied to the spool lowering operation [6], but the disturbed wave kinematics were only interpolated in the horizontal plane at the mean free surface since spools mainly consider horizontal elements. In the vertical direction, a decay formula as in incident waves for the wave kinematics was used. Although subsea templates contain both horizontal and vertical elements, the critical loads during lowering occur when the top roof of the anchors touches the water surface. When the anchor roof crosses the splash-zone, the added mass component theoretically increases from zero and becomes fully developed over a short vertical distance [24]. Thus, the decay formula in the vertical direction is also applied in this study for simplification.

Numerical program WADAM is applied to calculate the RAOs for the disturbed wave kinematics caused by the vessel diffraction and radiation using potential flow theory [6]. Figure 7 shows the contour of the RAOs of the disturbed wave elevation near the installation vessel with a 165 deg wave direction (long-crested waves) as an example. The initial positions of the subsea template anchors are highlighted in the figure. When the wave period is 12 s, the disturbed wave kinematic RAOs are close to those from the incident wave with RAO values close to 1. However, as the waves become shorter with 6 s peak period, the RAOs are greatly reduced due to the shielding effects. Moreover, it is also observed that the shielding effect is stronger when the location is closer to the stern under shorter wave conditions at a given wave direction.

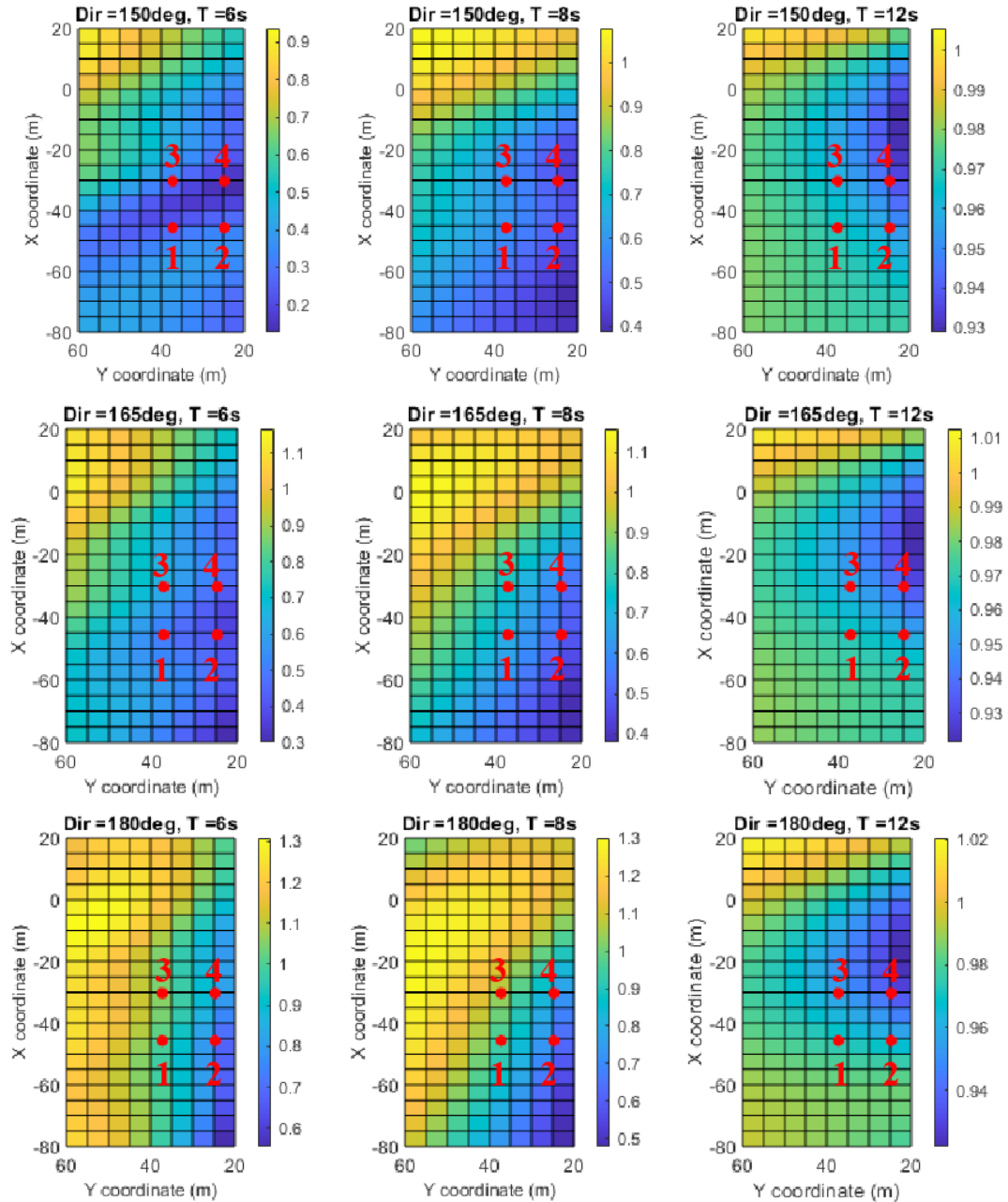### Short-crested waves and shielding effect

In real sea conditions, the wind-generated seas are often short crested with wave energy spreading in different directions. This spreading of wave energy may cause different forces and motions than those under long-crested waves. In this study, short-crested waves with different combinations of Hs and Tp are used in the numerical simulations. For each combination of Hs and Tp, JONSWAP spectrum is used to generate random waves. The spectrum considering the short-crestedness of the waves is then formulated by the JONSWAP wave spectrum $S(\omega)$ and the directional spreading function $D(\theta)$:

$$S(\omega, \theta) = S(\omega)D(\theta) \tag{4}$$

$$D(\theta) = \begin{cases} C(n)cos^n(\theta - \theta_0) & |\theta - \theta_0| \leq \pi/2 \\ 0 & |\theta - \theta_0| > \pi/2 \end{cases} \tag{5}$$

$$C(n) = \frac{1}{\sqrt{\pi}} \frac{\Gamma(1 + n/2)}{\Gamma(1/2 + n/2)} \tag{6}$$

where θ_0 is the main wave direction. The spreading index n describes the degree of wave short-crestedness, and n →∞ represents a long-crested wave field. Offshore lifting operations are usually carried out in relatively low sea states. Thus, the wave spreading is more significant when compared to higher sea states. In this study, a constant n = 2 is used in the spreading function when generating short-crested waves, and this index is considered reasonable to represent wind-generated seas in relatively low waves. Furthermore, the disturbed wave field caused by

Figure 7. RAOs of the wave elevation in disturbed wave region near the installation vessel at three different directions.

the shielding effects is highly influenced by the wave direction, as shown in Figure 7. Thus, the effects of short-crested waves and the shielding must be accounted for at the same time in the numerical analysis when calculating the responses of the lifting system.

3. Operational Criteria and Statistical Models

3.1 Operational Criteria

Based on DNV guidelines for lifting operations [8,25], two main criteria for the splash-zone crossing, i.e., the

maximum load on the main lift wire and the slack of the main lift wire and slings, are considered when assessing the allowable sea states.

For offshore lifting operations, the recommended dynamic amplification factor (DAF) for a static hook load (SHL) between 100 tons and 300 tons is 1.25. For the studied case, the SHL is around 275 tons, so the maximum allowable dynamic hook load (DHL) is calculated as 345 tons. By checking the lifting capacity of the crane equipment, this DHL value is within the operational capacity of the vessel's crane. Furthermore, the crane itself

requires a maximum value of DAF shall not exceed 1.3, with a maximum static load of 320 tons when the working radius of the crane is 18 m. Based on this requirement, the maximum dynamic tension of the crane lift wire should not exceed 416 tons during the whole operation.

Regarding the slack sling criterion, the DNV standards require a minimum margin against slack which is 10% of the minimum static weight and therefore 10% of the static load for the hoist line and slings, respectively. If some components are hollow and subjected to flooding during submergence, the submerged weight should be taken as the minimum static weight without considering flooding. For the current study, the submerged weight of the subsea template is 230 tons. Therefore, based on the required 10% margin against the slack criterion, the minimum dynamic tension in the main lift wire should not be less than 23 tons, and for each sling, the dynamic tension should never be less than 6 tons during the whole lowering operation.

The above two criteria are used to assess the allowable sea states for the splash zone crossing operation of the subsea template.

3.2 Statistical Models

Because of the variability of stochastic waves, statistical modeling of the critical extreme responses is used during the assessment of the allowable sea states. In this study, the critical responses include the maximum and minimum tensions in the main lift wire and slings during the splash-zone crossing. The maximum (or minimum) tensions from all wave seeds are fitted into a selected statistical model, and the extreme values can be obtained from the fitted statistical model. The sensitivity of the obtained extreme responses depends on the probability of non-exceedance. In practice, a value between 0.9 and 0.99 is chosen according to the associated risks of the operation. In this study, the assigned target probability of non-exceedance is 0.95.

Gumbel extreme value distribution is widely used in predicting both maximum and minimum extreme responses for different offshore structures [26]. The cumulative distribution function (CDF) of Gumbel distribution of a random variable X is given by

$$F_x(x; \lambda, \kappa) = exp\left[-\exp\left(\frac{x - \lambda}{\kappa}\right)\right] \tag{7}$$

where λ and κ are the location and scale parameters of the distribution, respectively.

This study investigates the possibility of achieving a better statistical representation of the operation's extreme responses by comparing Gumbel and Generalized Extreme Value Distribution (GEV) fittings. When dealing

with a small number of available data, a two-parameter fitting can be quite poor due to the lack of flexibility. To overcome this, generalizations of the Gumbel distribution were introduced. GEV combines Gumbel, Fréchet, and Weibull extreme value distributions, which provides more flexibility in fitting a population of data compared to Gumbel. The CDF of the GEV distribution is given by

$$F_x(x; \lambda, \kappa, \beta) = \exp\left(-\left[1 + \beta\left(\frac{x - \lambda}{\kappa}\right)\right]^{-\frac{1}{\beta}}\right) \tag{8}$$

where λ, k, β are the location, scale, and shape parameters of the distribution. The maximum and minimum values for the lift wire and slings are extracted from the response time series for each sea state realization (seed). Then, the parameters of both Gumbel and GEV distributions are estimated using the maximum likelihood method by fitting the responses from all wave seeds. The extreme values are then obtained from the fitted distribution at the given probability of non-exceedance.

4. Model Validation with Field Measurements

Before the allowable sea state assessment is carried out, a validation of the numerical model and numerical results is performed to ensure that the employed numerical model is accurate enough. The validation is to compare the numerical results with the crane logging time history from the same installation vessel during the actual offshore deployment. The logging data are from the installation of a template with a similar footprint to the one used in this study. However, the total weight of the installed template is smaller than the one used in the model. Thus, the current template model is modified in SIMA-SIMO to match that of the installed one. Because the exact wave elevation data were not recorded during the field measurement, various realizations of the waves (seeds) are used for the same Hs and Tp condition in the numerical simulations to validate the results. The effect of variability in seed numbers is further discussed in section 6.3.

Figure 8 compares the lift wire tension of both field measurements and SIMO model. The top plate of the subsea template enters the free surface at approximately 240 s. It is shown that the estimation of the slamming forces at 240 s agrees well with the field measurements. The fluctuations in the lift wire tension from the numerical model matched those from the logged data, especially for seed no.10. The maximum and minimum tension values from SIMO do not show any significant deviation from the measured data in the first 300 s. In seed no.27, the tension force is slightly overestimated after 300 s, while in seed no.10, the force in the lift wire is slightly underestimated for the same time segment. This slight deviation does not
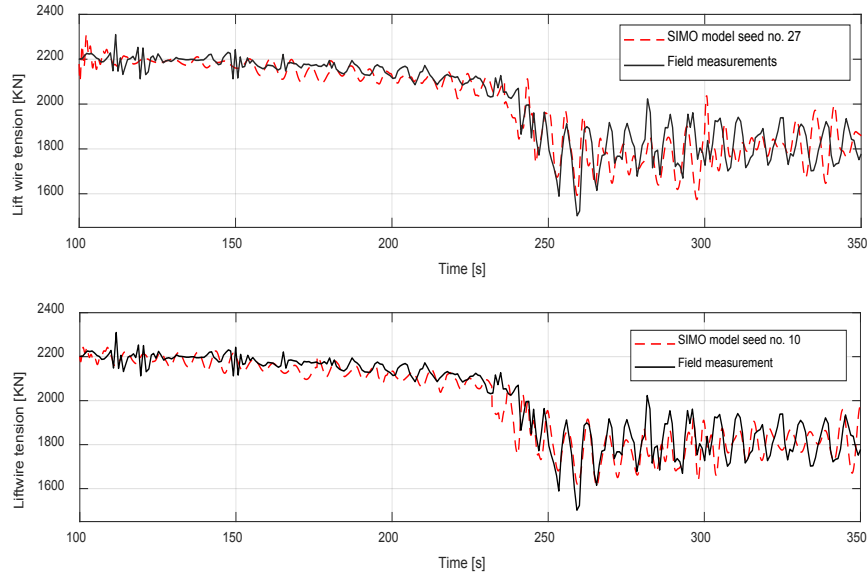
Figure 8. Comparing lift wire tension field measurements with SIMO model (Hs=1.9 m, Tp=6 s) with shielding effect.

impose any limitation on using the established numerical model in this study. Due to the stochastic nature of waves, it is very challenging to capture all variations of the tensions due to lack of exact wave elevation information. However, this comparison validates that the current model is capable to provide accurate estimation of the maximum and minimum tensions in the splash zone crossing process.

5. Eigenvalues and Time-domain Analysis

5.1 Eigenvalues Analysis

The natural periods of the system are obtained from the eigenvalue analysis. The analysis is conducted without including any external forces or damping effect and the following equation of motion is solved in the frequency domain:

$$[-\omega^2(M + M_a) + K] \cdot x = 0 \tag{9}$$

where, ω is the natural frequency; M and M_a are the mass and added mass matrices of the system; K is the stiffness matrix, and x is the motion vector. The mass matrix includes both structural and hydrodynamic added mass. The analysis is performed for three different vertical locations for the template prior to the evaluation of the time-domain simulation results. These locations are illustrated in Figure 9 and defined when:

a) The anchor bottom is just above the free water surface
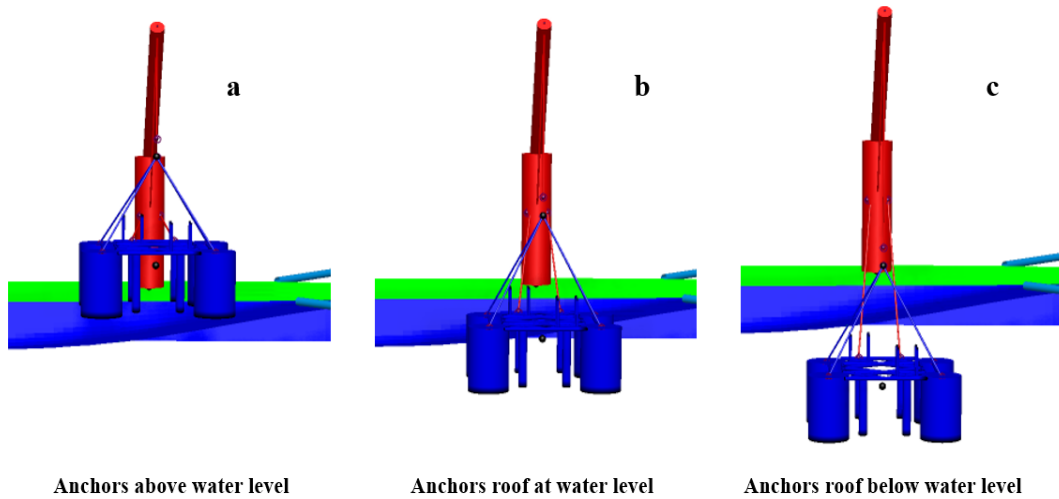
Figure 9. Template vertical positions in SIMO for frequency domain analysis.

b) The anchor roof is at the free water surface

c) The template is fully submerged

Table 7. Coupled system natural periods at three vertical positions of the template. (The vertical positions of the anchor roof relative to the mean free surface are used)

z = 8 m	z = 0 m	z = –8 m	Dominant motions
3.56 s	3.86 s	3.77 s	Template heave & vessel roll
6.91 s	6.94 s	6.96 s	Vessel roll & pitch
8.01 s	8.03 s	8.04 s	Vessel roll & heave
8.86 s	-	-	Template pitch & surge
14.28 s	-	-	Template roll & sway

To simplify the static analysis, the three degrees of freedom (DOF) of the hook are neglected when obtaining the natural periods of the installation system. Thus, the coupled system has 12 DOFs corresponds to 12 modes in total. The most critical position of the template is obtained from the transient dynamic responses in the time-domain simulations. This position is defined when the anchor roof crosses the splash zone. The natural periods of the coupled system are presented in Table 7. At short periods, the system is mainly dominated by the template heave and vessel roll motion for all given template positions. As the natural periods start approaching 8 s, both the pitch and heave motions of the vessel share dominance with the roll motion over the coupled system. Furthermore, when the template is still in air (z=8 m), the template pendulum motion dominates the system at long periods. However, this dominance starts shifting out of the peak periods operational range when the anchors roof is at the free water surface (z=0 m) or deeply submerged (z= –8 m).

5.2 Time-domain Simulations

Both the transient and the steady-state approaches are applied in the time-domain simulations in this study. In both approaches, the equations of motion are solved by numerical integration with a time-step of 0.02 s. The wave excitation forces on the construction vessel are pre-generated from the transfer functions obtained from the frequency-domain analysis. The radiation effects on frequency-dependent added mass and damping forces are included in terms of coupled retardation functions in the time domain. The calculation of wave forces on the subsea template is based on the instantaneous locations of each slender element of the template. The tensions in the wires are directly calculated for each time step based on the relative motions between the bodies.
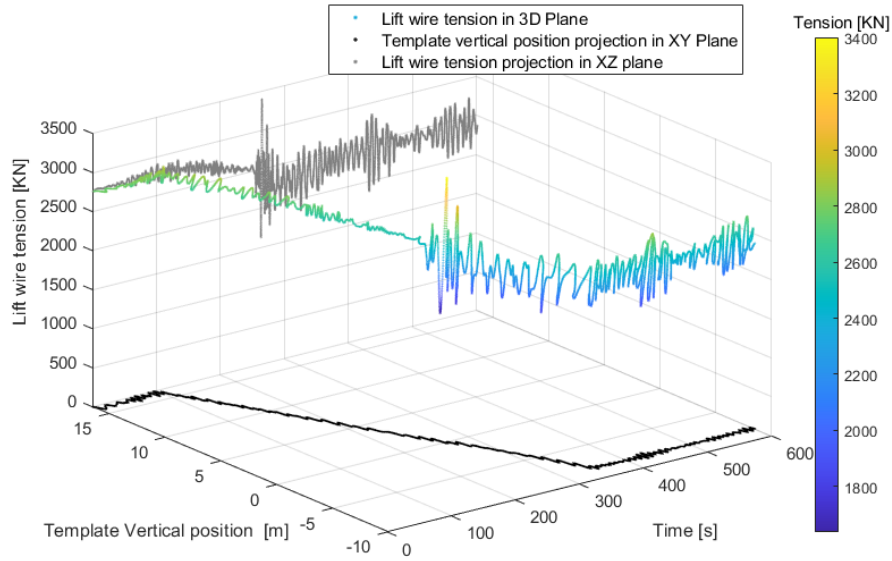
5.2.1 Transient Approach

In the transient approach, the winch starts at 100 s and stops at 600 s with a speed of 0.1 m/s. An example of the dynamic responses of the lift wire tension is presented in Figure 10. In air, the tension acting on the lift wire is mainly due to the template weight. The dynamic force acting on the lift wire starts to decrease gradually due to buoyancy from 130 s when the template anchors are entering the water. When the template is fully submerged at 290 s, the water fills at a steady rate of 144 kg/s for a period of 110 s.

As lowering takes place, a fluctuation in the lift wire tension takes place due to the vessel motion and the slamming loads caused by the wave kinematics. It is noticed that this fluctuation is more intense when the anchors roof reaches the free water surface around 260 s. The vertical position of the template is projected on the XY plane, and the tension time history is projected on the XZ plane in Figure 10. The figure clearly shows that the highest response occurs when the anchor roof is at the free water surface (the template vertical position is close 0 m in XY plane). When the template is fully submerged, the wave kinematics starts decaying exponentially, thus reducing the slamming loads on the template.

5.2.2 Steady State Approach

The steady state approach is performed by placing the template at the most critical submergence during the whole simulation duration with zero winch speed. As previously shown in Figure 10, the largest dynamic response of the lift wire tension occurs when the suction anchor roof reaches the free water surface. In the steady state method, the template is placed where the mean position of the anchor roof is at the mean water surface. The simulation length is set to the same as the duration of the transient approach. Figure 11 compares the lift wire tension using the transient and steady state approach. The hydrodynamic forces are more violent when using the steady state approach. Such outcome is expected since the anchor roofs are constantly subjected to the highest wave kinematics at the free water surface, which increases the tension forces on the lift wire according to Equation (2). However, the lift wire tension behavior starts to be similar between the two approaches after the anchor roof reaches splash-zone around 260 s in the transient case. At this time instance, the template starts experiencing the same dynamic loads due to wave kinematics at the free water surface. As the template is getting fully submerged, the intensity of the slamming loads in the transient case is less compared to the steady state due to the decaying effect.

Figure 10. Lift wire tension using transient approach (Hs = 1.8 m, Tp = 8 s, and Dir = 165 deg), without shielding effect.
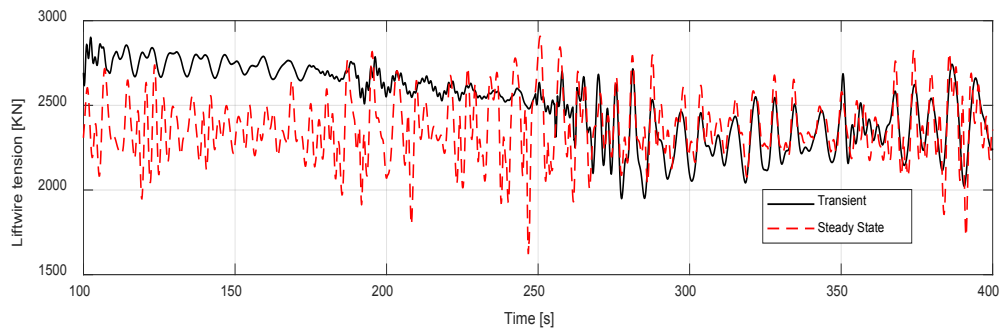
Figure 11. Comparison of responses using steady-state and transient analysis methods (Hs = 1.8 m, Tp = 8 s, and Dir = 165) without shielding effect.

6. Dynamic Responses and Allowable Sea States Assessment

## 6.1 Dynamic Responses with and without Shielding Effect

The lift wire dynamic responses indicate that the maximum tension criterion defined in Section 4 is more critical for the operation than the slack wire criterion. It is also noticed that the dynamic responses of the system during splash-zone crossing can differ greatly with different input sea realizations for the same sea state due to the stochastic nature of waves. Figure 12 provides a comparison of the lift wire tension at two different sea realizations with the same Tp and Hs. Seed no.29 clearly exceeds seed no.48 in terms of maximum and minimum tension. The figure also shows that the minimum slack criterion does not impose any limitation on the evaluated

sea states. The wave elevations at the location where the center of the template is lowered into the water using the two wave seeds are also compared in Figure 12. The comparison shows that the maximum wave elevation when the anchor roof reaches the splash-zone (between 260 s and 265 s) is almost 0.15 m at seed no.48 and 1 m at seed no.29. Thus, higher slamming loads are expected at seed no.29 compared to seed no.48.

When the shielding effect is considered, a decrease in the lift wire tension is observed. Figure 13 compares the time history of the lift wire tension with and without shielding effect using the transient approach. For the results with shielding effect included, the dynamic forces are reduced when the suction anchor roof reaches the splash-zone (around 260 s) for Tp = 8 s. However, the influence of the shielding effect is almost absent at the higher peak period with Tp = 12 s, where the maximum
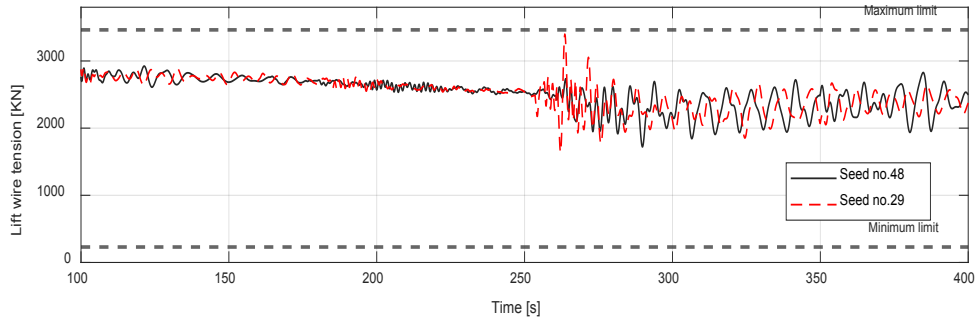
(a) Lift wire tension
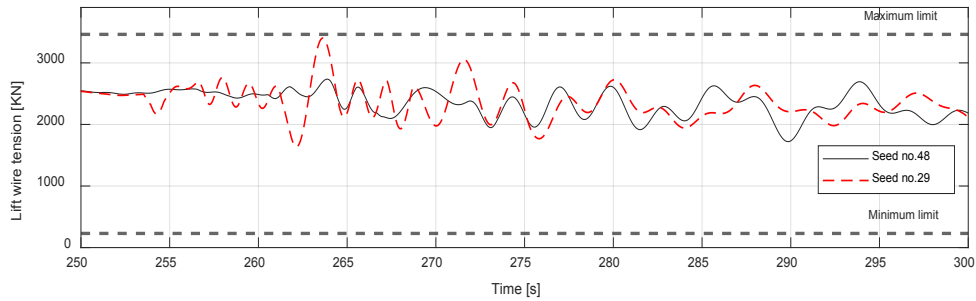
(b) Lift wire tension from 250s to 300s
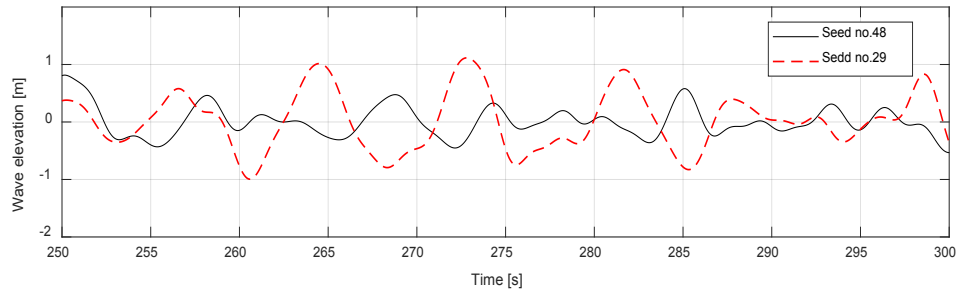
(c) Wave elevation from 250s to 300s

Figure 12. Time histories of lift wire tension and wave elevation of two different wave realizations for the same sea state (Hs=1.8 m, Tp=8 s, Dir=165 deg) without shielding effect.

lift wire tension is 2865 KN and 2832 KN with and without shielding, respectively. This outcome aligns with the obtained wave kinematic RAO in the disturbed waves region near the template in Figure 7. The RAO of the wave kinematics is closer to 1 at 12 s compared to 6s peak period.

Figure 14 also compares the dynamic responses of the lift wire tension with and without shielding effect when steady state simulation is applied. In this case, the dynamic responses are less influenced by the vessel shielding when compared with the transient case at 8 s peak period. The template maintains its position at the free water surface in steady state. As a result, the

wave kinematics are not decaying and the template will experience more slamming loads, thus reducing the overall operational limits. However, the time history still shows an overall decrement in the lift wire tension with the shielding model.

The GEV distribution is used to fit the maximum tensions with and without shielding effect at different peak periods. A total of 100 maximum values of lift wire tension are generated from simulations using 100 wave seeds. The fitting of the probability density functions (PDF) of two wave conditions is compared in Figure 15. It can be observed the PDFs are significantly different with and without shielding at Tp = 6 s. The PDF of the
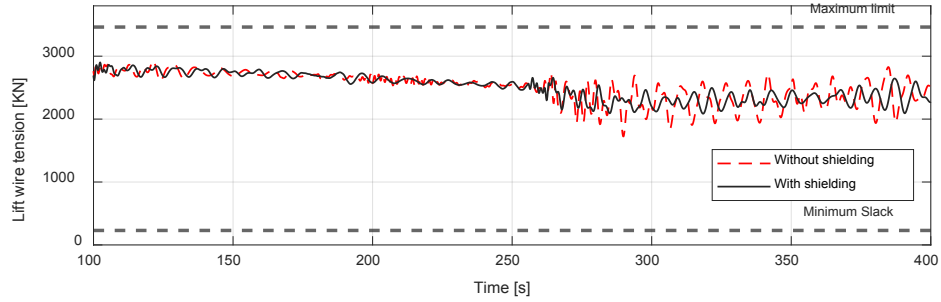
(a) Hs=1.8m, Tp=8s, Dir=165 deg
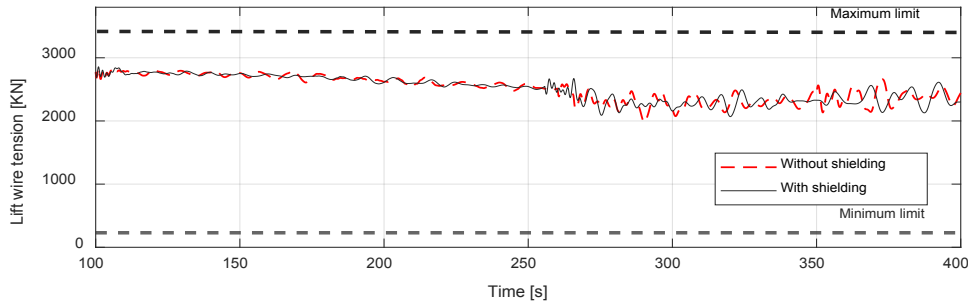
(b) Hs=1.8m, Tp=12s, Dir=165 deg

Figure 13. Time history of the lift wire tension with and without considering shielding effect at two Tp conditions.
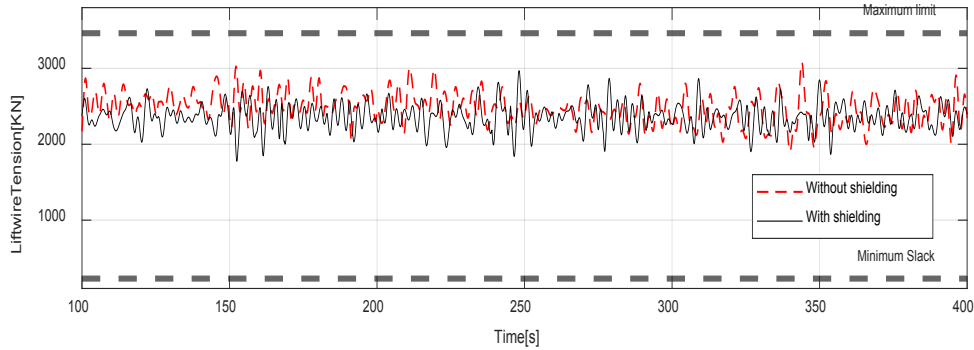
Figure 14. Comparing lift wire tension with and without shielding effect for using steady state approach (Hs=1.8, Tp=8 s, Dir=165 deg).

maximum tensions has more deviation from the mean value without the shielding effect. This is because the template is exposed to higher incident waves, which results in higher variability of the slamming forces using different wave realizations. As Tp increases to 12 s, the PDF of the maximum tensions is similar with and without the shielding effect.

6.2 Influence of the Wave Direction

The RAOs of the vessel and the shielding effect depend on the wave direction. In lifting operations, the vessel is often positioned heading to the incoming waves. At this position, the vessel will experience lower heave and roll motions compared to other headings. The heave, roll, and pitch motions dominate the crane tip responses as the lowering of the template takes place. The RAOs of the vessel's heave and roll for different wave directions are presented in Figure 16.

From Figure 16, the RAOs of both roll and heave motion are lowest when the wave direction is 180° across the given range of the wave peak period. As discussed earlier, the shielding effect is also sensitive to the wave direction. The installation vessel provides a shielding
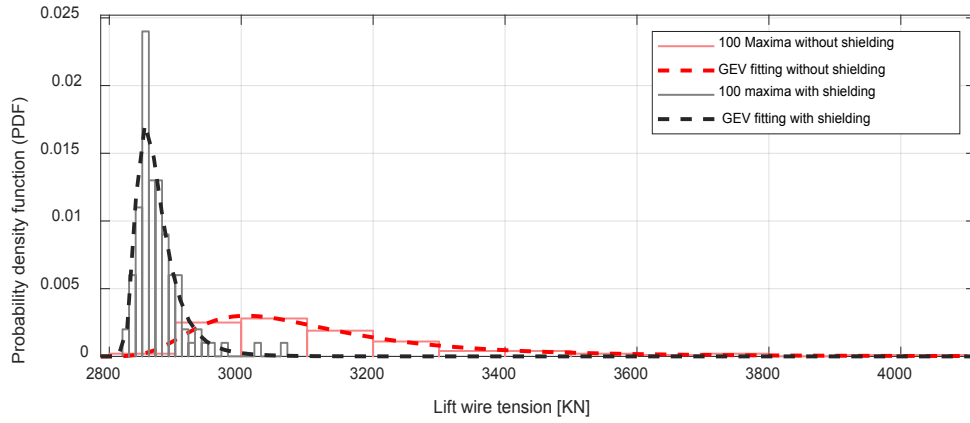
(a) PDF of the maxima at Tp = 6s, Hs = 2m
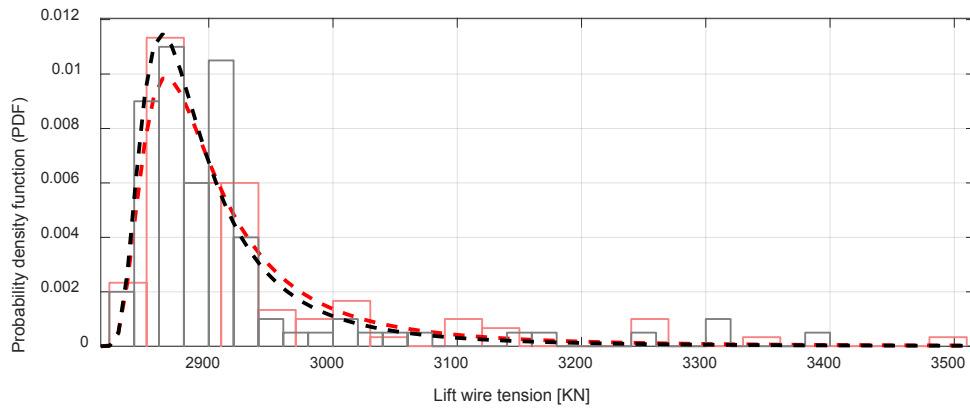
(b) PDF of the maxima at Tp = 12s, Hs = 2m

Figure 15. PDF functions of the maximum lift wire tensions with and without shielding effect.
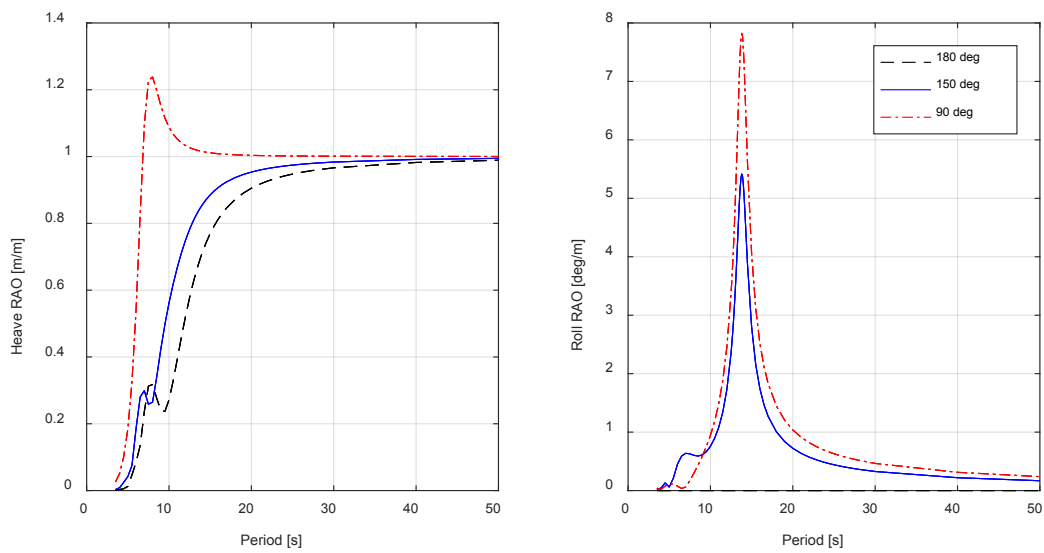
Figure 16. Heave and roll RAOs of the installation vessel.

effect for wave directions between 0° and 180 deg (See Figure 2). The disturbed wave kinematics RAO at 150 and 180 deg are also illustrated in Figure 7. The figure shows an increase in the wave RAO value when the wave direction is 180 deg compared to 150 deg. The influence of changing direction is more noticeable at Tp = 6 s with the RAO value increasing from 0.3 near the anchor location at 150 deg to almost 1 at 180 deg.

To further study the influence of wave directions on the responses of the dynamic system, simulations for three wave directions within a range of 150 to 180 deg using 50 seeds are performed. The chosen peak period is 8 s, and Hs is set to 2 m. 50 maxima of the lift wire tension are obtained from each seed for each wave direction. The maximum lift wire tensions under three wave directions are fitted using GEV distribution and compared in Figure 17. The lowest deviation from the mean tension value is obtained at 180 deg, while the highest is at 150 deg. Thus, it is concluded that a better shielding angle does not necessarily provide better operational limits since the vessel heave and roll RAOs have more influence on the lift wire maxima at any given wave direction.

6.3 Assessment of Allowable Sea State

The extreme value distributions introduced in Equations (7) and (8) are used as the statistical model for the lift wire extreme response. Although Gumbel distribution can provide a proper fitting for the extreme responses in various studies [6,18,27], this study aims to check the possibility of using the GEV distribution to achieve a better assessment of the allowable sea state based on the assigned target probability of non-exceedance. Figure 18 compares the probability plot fitting using the two mentioned distributions against the lift wire maxima. Both distributions show great variability when using different number of seeds. When 25 seeds are used, the plot shows poor fitting near the assigned target probability for both models. Applying the statistical model with this number of seeds can cause an underestimation of the extreme responses due to the outlier data at the tail. When 50 seeds are used, a better fitting is achieved at 0.95 probability of non-exceedance. Moreover, the overall deviation between GEV and Gumbel fittings is less compared to 25 seeds. At 100 seeds, the deviations between the two fittings start to be more obvious at lower probabilities. However, both distributions still provide a slightly more precise prediction of the extreme responses near the tail at 0.95 probability of non-exceedance.

From Figure 18 it can be concluded that assigning a target probability above 0.95 is not practical regardless of the number of seeds being used. The uncertainties of both statistical models are quite large for higher probabilities of non-exceedance. Furthermore, the study cannot conclude which statistical model provides a better fitting for the maxima since a perfect fitting at the tail is not achievable due to the outlier data.

In Figure 19, it is noticed that GEV provides an over-all better fitting with the steady state approach for target probabilities below 0.95. However, at 0.95, both Gumbel and GEV provide an acceptable fitting for the maxima, especially when using 50 or 100 seeds. It is also noticed that assigning a target probability above 0.95 might be possible with GEV when 50 maxima or more are used with the steady state approach.

Since Figure 18 showed a slight variation when using 50 and 100 seeds compared to 25 seeds, the allowable sea states are evaluated based on 50 seeds for the maximum lift wire tension. Figure 20 compares the obtained allowable sea states using the GEV and Gumbel statistical models. The results are obtained using the transient approach
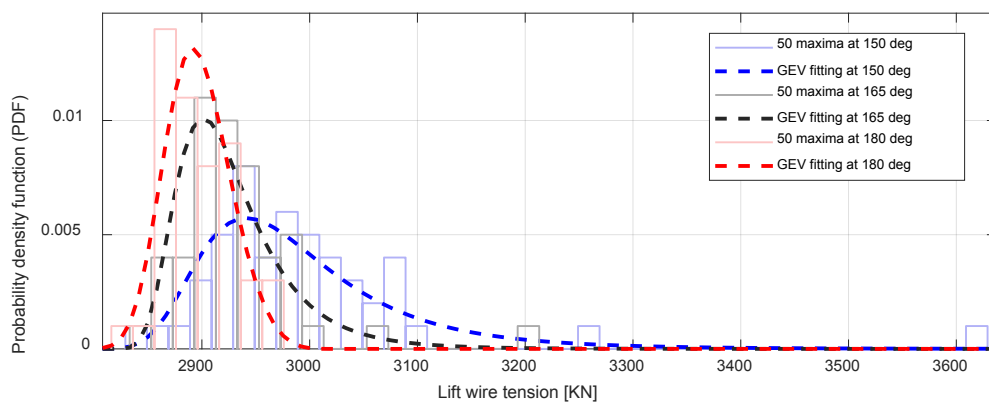
Figure 17. Lift wire maxima PDFs at three different wave directions (Hs = 2 m, Tp = 8 s).
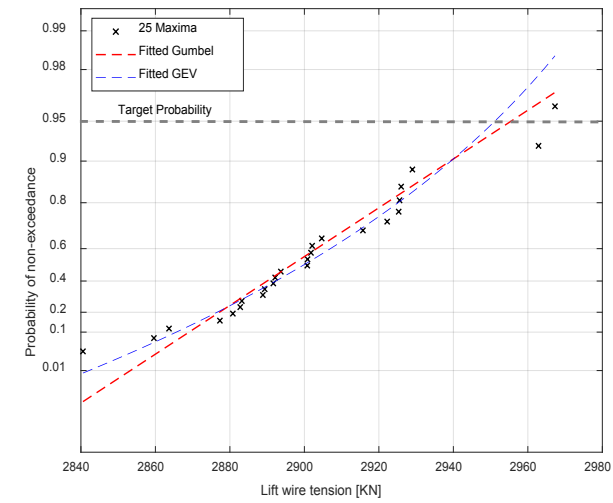
(a) 25 seeds
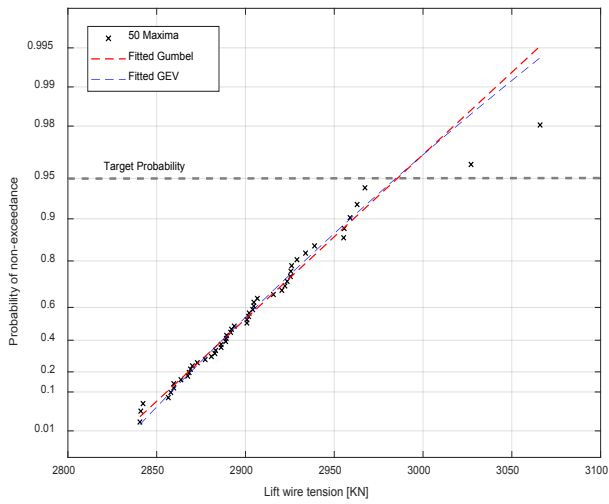
(b) 50 seeds
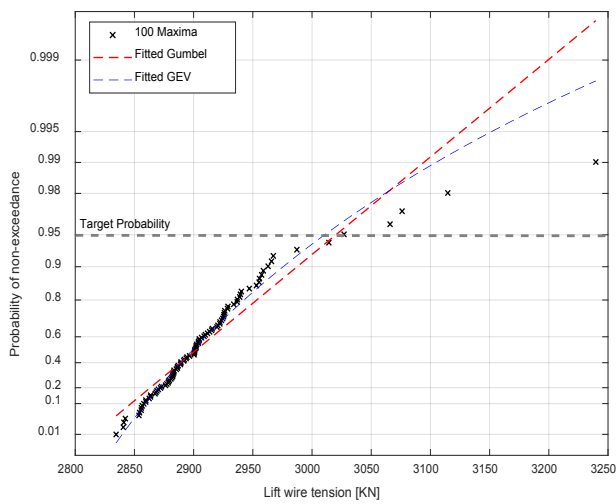
(c) 100 seeds

Figure 18. Probability paper plot for GEV and Gumbel distributions using transient approach with shielding (Hs =1.8 m, Tp =8 s, Dir =165 deg)
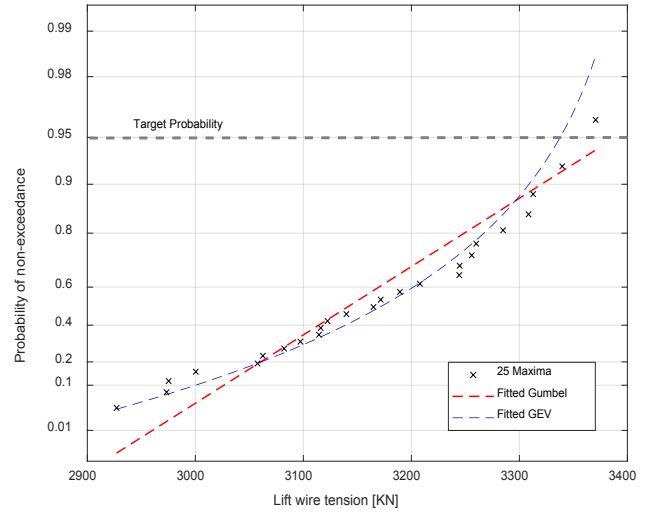
(a) 25 seeds
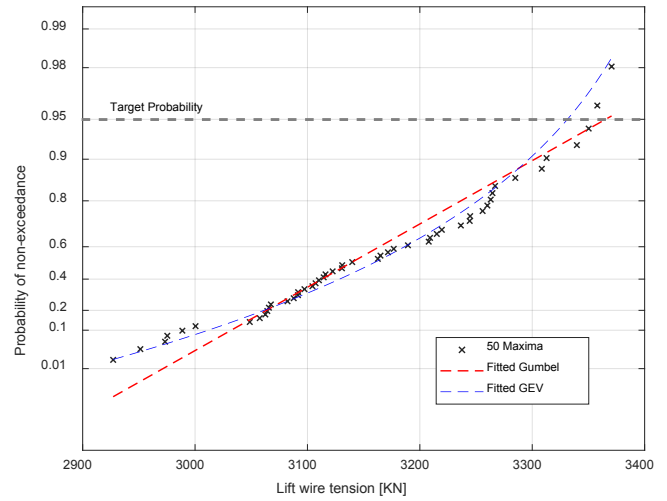
(b) 50 seeds
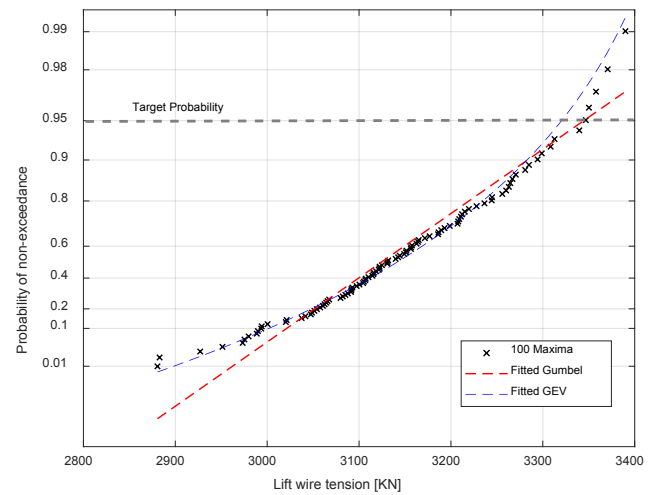
(c) 100 seeds

Figure 19. Probability paper plot for GEV and Gumbel distributions using steady state approach with shielding (Hs =1.8 m, Tp =8 s, Dir =165 deg)

with the shielding effect. The figure does not show any significant differences in the obtained sea states for both distributions. In general, the GEV result is slightly more conservative for the operational Hs across all the chosen Tp. Both distributions provide higher operational limits at lower Tp, especially when 180 deg wave direction is used.
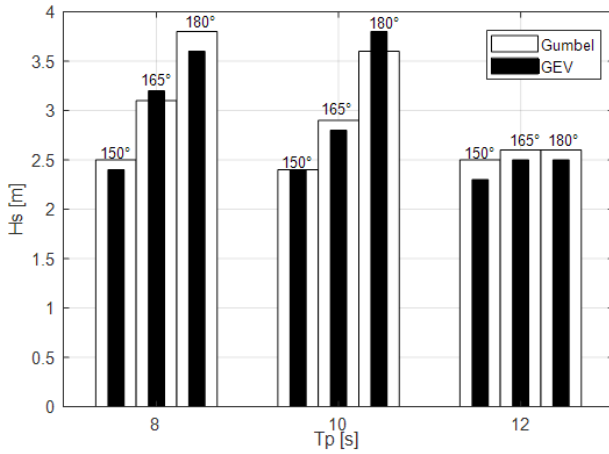
Figure 20. Comparing Gumbel and GEV using transient approach with shielding for different wave directions.

Table 8 compares the obtained allowable sea states for the operation based on GEV models. The comparison is carried out for three wave directions using transient and steady state approaches. The sea states are also compared with and without the shielding effect. A total of 50 lift wire maxima are used for the statistical model. When using transient approach, the allowable sea states are significantly higher at low peak periods with shielding effect, especially at 180 deg wave direction. This outcome is expected after the demonstrated results in Figure 15 and Figure 17.

In steady state, the shielding effect shows less influence on the limiting sea states compared to the transient

approach. The template maintains its position at the free water surface in the steady state. As a result, the wave kinematics are not decaying and the template will experience more slamming loads, thus reducing the overall operational limits. Same as the transient approach, the highest operational Hs is obtained with shielding effect when the wave direction is 180 deg.

Based on this result, the steady state approach does not represent the real operational conditions, and the obtained allowable sea states using this approach will be over conservative, especially for short periods. Normally, the transient approach is more practical for similar studies when a sufficient number of seeds are used.

6.4 Influence of the Dimension of the Suction Anchor

The responses of the template and the lifting system during splash-zone crossing operation depend greatly on the slamming loads acting on the roof of the four suction anchors. Furthermore, Table 6 shows that the total added mass in both vertical and horizontal directions is almost 5 times larger than the actual mass of the whole template. Most of these inertia components are caused by the large size of the anchor. This reveals that the larger dimension of the suction anchors will cause higher slamming loads. To be more specific, when the diameter of the suction anchor increases, the volume of the trapped water inside the anchor will also increase, thus increasing the hydrodynamic added mass in the vertical direction. Larger diameters will also cause an increase in the drag forces on the anchor walls. To study the influence of the anchor size on the allowable sea states, three additional simulation cases are set up by changing the size of the template anchors. Hydrodynamic coefficients for each case are calculated accordingly while the same overall mass of the template is

Table 8. Allowable sea states using transient and steady state based on GEV statistical model.

		Hs[m] with shielding				Hs[m] without shielding		
Transient	Tp[s]\Dir[deg]	150	165	180	Tp[s]\Dir[deg]	150	165	180
	6	3.9	5 *	4.5*	6	1.7	2	2.1
	8	2.4	3.2	3.6	8	1.6	1.7	1.9
	10	2.4	2.8	3.8	10	1.9	2	2.2
	12	2.3	2.5	2.5	12	2.1	2.2	2.3
Steady state	Tp[s]\Dir[deg]	150	165	180	Tp[s]\Dir[deg]	150	165	180
	6	1.7	2.2	2.1	6	1.8	2	2.1
	8	1.9	2.2	2.3	8	1.7	1.9	2
	10	2.2	2.5	2.6	10	1.5	1.7	1.8
	12	2.3	2.4	2.6	12	1.5	1.6	1.7

* At Tp=6 s, the wave will break at such high Hs values. The wave breaking limit is not considered in this study.

a) Transient approach

b) Steady State approach
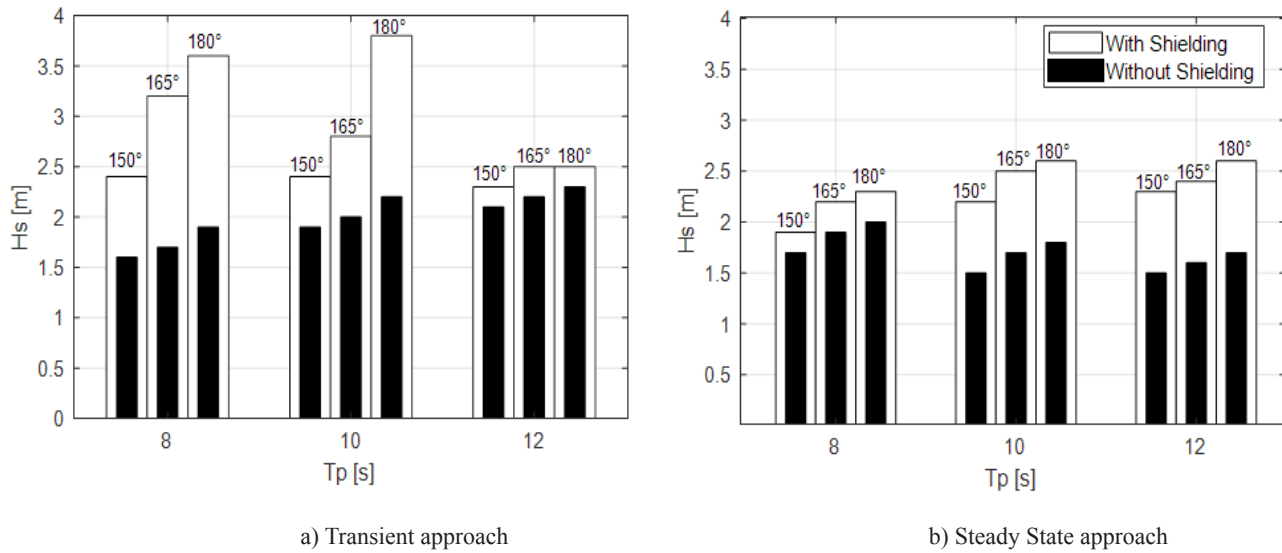
Figure 21. Allowable sea states based on GEV statistical model

applied for all cases. Table 9 compares the hydrodynamic properties of the anchor from the original case with three new cases.

For each case, dynamic responses for 50 seeds are carried out at the same sea sate and wave direction, considering shielding effects. Figure 22 compares the GEV probability plot of the maxima lift wire tension for different cases. When the diameter is reduced to 4m (D4.0), the lift wire tension is 2885 KN at the target probability of non-exceedance. As the diameter increases, the tension increases gradually until it reaches 3160 KN at D5.5. Thus, it can be concluded that any change in the anchor diameter can alter the operational limits significantly. Smaller anchors are most likely to have higher allowable Hs for similar operations. Same as the previous results obtained in section 6.3, Figure 22 also shows that assigning a target

probability higher than 0.95 for all cases is not practical when using 50 seeds. The GEV distribution shows an increased deviation in the fittings from actual values at higher probabilities. If a higher probability is assigned, the obtained lift wire tension from the statistical model can vary significantly from the actual value of the maxima.

The allowable sea states of the four cases with different anchor sizes are presented in Table 10 and Figure 23. From the table, it is seen that Case1 results in highest allowable Hs for all Tp conditions. The most noticeable outcome is when Tp is set to 8 s. The increment in Hs value is less significant when compared with other peak periods. This outcome is explainable through the eigenvalues analysis in Table 7. The analysis showed that the coupled system would experience higher dynamic responses around 8 s period. When the template is still above the water level,

Table 9. Anchor sizing hydrodynamic loads comparison.

Case name	Diameter [m]	Vertical added mass [ton]	Horizontal added mass [ton]	Vertical linear damping [kNs/m]	Horizontal quadratic damping [kNs²/m²]
Case1 (D4.0)	4	140	181	40	24
Case2 (D4.5)	4.5	183	225	44	27
Case3 (D5.0)	5	233	270	52	34
Original case (D5.5)	5.5	290	330	57	48

Table 10. Different anchor sizes allowable Hs using transient approach with shielding effect (wave direction 165 deg).

Case name	Tp [s]			
	6	8	10	12
Case1 (D4.0)	5.5 m	3.5 m	3.4 m	3.4 m
Case2 (D4.5)	5.4 m	3.4 m	3.3 m	3.2 m
Case3 (D5.0)	5.2 m	3.3 m	3 m	2.8 m
Original case (D5.5)	5 m	3.2 m	2.8 m	2.5 m
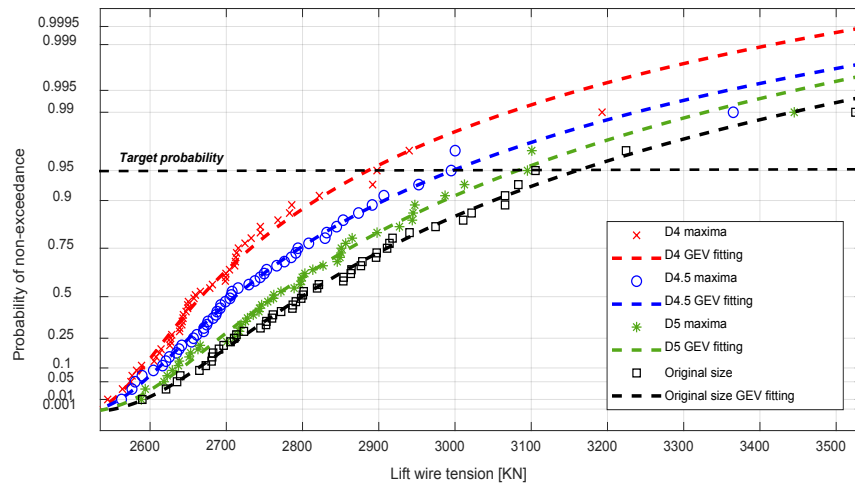
Figure 22. Non-linearized probability plot of the lift wire maxima for different anchor sizes. (Tp = 8 s, Hs = 3 m, Dir = 165 deg, with shielding)
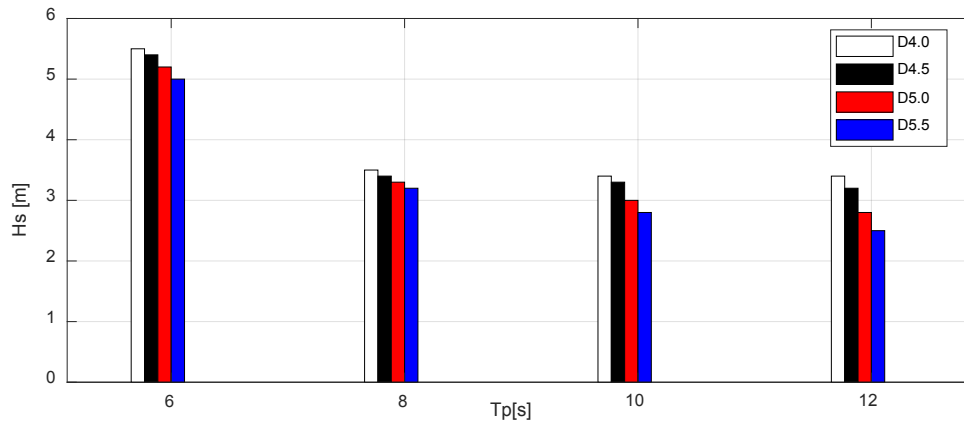
Figure 23. Different anchor sizes allowable Hs using transient approach with shielding effect (wave direction 165 deg).

the natural period is dominated by the vessel and the template pendulum motion. As the template reaches the free water surface, the vessel heave and roll motions start dominating the system at 8 s periods. These combined motions will accelerate the template body through the splash-zone, thus increasing the slamming loads according to Equation (2) and reducing the overall increment of Hs for smaller anchor diameters.

7. Conclusions

This paper presents a numerical study of splash-zone crossing operations for a subsea template. SIMA-SIMO is used to develop the fully coupled numerical model, which includes the installation bodies, the lifting system, and the hydrodynamic inputs. The hydrodynamic loads are calculated according to Morison's equation. Both frequency

and time-domain simulations are performed to identify the critical response of the operation. The operation criteria are defined based on DNV guidelines and the operational sea states are evaluated.

Two time-domain simulation methods are used in the study, the transient and the steady state. The established numerical model is validated with actual field measurements before carrying out the allowable sea states assessment. Two statistical models (Gumbel, GEV) are employed in fitting the lift wire maxima to obtain the allowable sea states of the operation. The operational limits are assessed based on each model. The assessment is carried out for different wave directions and seeds number with and without shielding effect. The influence of changing the wave direction on both the vessel motion and the template is also discussed. Three cases with different anchor sizes are introduced to demonstrate the influence of

changing the anchor diameter on the slamming loads. The main findings are summarized as follows:

- The lift wire maximum tension is identified as the dominating limiting criterion for the operation. The most critical position for the template is defined when the anchors roof is at the splash-zone.

- In the transient approach, the vessel shielding shows more influence on improving the operational limits with short peak periods, especially when the waves are facing the vessel bow. However, the shielding has less influence when it comes to steady state simulations.

- The steady state approach does not represent the real operational conditions, and the obtained allowable sea states will be more conservative, especially for short periods. The transient approach is recommended for similar studies.

- The study showed big variability when using different number of seeds to establish the statistical model. It is also concluded that assigning a target probability of non-exceedance higher than 0.95 is not practical in this study due to the outlier data at the tail.

- It cannot be concluded whether Gumbel or GEV provides a better fitting for the extremes. Both distributions do not provide a perfect fitting, especially at the tails. In general, the differences between Gumbel and GEV are not big when used in obtaining the allowable sea states.

- Decreasing the anchor diameter can alter the operational limits significantly due to the decreased values of hydrodynamic drag and added mass. Thus, templates with the same total mass but smaller anchors are more likely to have higher operational limits at the same sea states.

Conflict of Interest

There is no conflict of interest.

References

[1] Li, Y., Zhao, H., Xu, N., et al., 2020. Study of the Installation Process of the Subsea Tree Passed Through the Splash Zone. Energies. 13(5), 1014.

[2] Jia, D., Agrawal, M., 2014. Fluid-structure interaction: lowering subsea structure/equipment in splash zone during installation. Offshore Technology Conference. Offshore Technology Conference.

[3] Wang, Y.Y., Tuo, H.H., Li, L.W., et al., 2018. Dynamic simulation of installation of the subsea cluster manifold by drilling pipe in deep water based on OrcaFlex. Journal of Petroleum Science and Engineering. 163, 67-78.

[4] Jacobsen, T., Naess, T.B., 2014. Installation of subsea structures using mid-size construction vessels in harsh environments. Offshore Technology Conference-Asia. Offshore Technology Conference.

[5] Gordon, R.B., Grytøyr, G., Dhaigude, M., 2013. Modeling suction pile lowering through the splash zone. ASME 2013 32nd International Conference on Ocean, Offshore and Arctic Engineering. American Society of Mechanical Engineers Digital Collection.

[6] Li, L., Parra, C., Zhu, X., et al., 2020. Splash zone lowering analysis of a large subsea spool piece. Marine Structures. 70, 102664.

[7] Li, L., Gao, Z., Moan, T., 2016. Operability analysis of monopile lowering operation using different numerical approaches. ISOPE.

[8] DNV·GL, 2017. Recommended practice: Modelling and analysis of marine operations, DNVGLRP-N103.

[9] DNV·GL, 2017. Recommended practice: Lifting appliances used in subsea operations, DNVGL-RP-N201.

[10] Acero, W.G., Li, L., Gao, Z., et al., 2016. Methodology for assessment of the operational limits and operability of marine operations. Ocean Engineering. 125, 308-327.

[11] Li, L., Gao, Z., Moan, T., 2015. Response Analysis of a Nonstationary Lowering Operation for an Offshore Wind Turbine Monopile Substructure. Journal of Offshore Mechanics and Arctic Engineering. 137(5).

[12] Bai, Y., Bai, Q., 2010. Subsea engineering handbook. Elsevier: Amsterdam; Boston; Paris.

[13] Bunnik, T., Buchner, B., 2004. Numerical prediction of wave loads on subsea structures in the splash zone. in The Fourteenth International Offshore and Polar Engineering Conference. International Society of Offshore and Polar Engineers.

[14] Damblans, G., Berhault, C., Marcer, R., et al., 2012. CFD and Experimental Investigations of Slamming Load Prediction on Subsea Structures in Splash Zone. The Twenty-second International Offshore and Polar Engineering Conference. OnePetro.

[15] Buchner, B., Bunnik, T., Honig, D., et al., 2003. A new simulation method for the installation of subsea structures from the splash zone to the ultra deep. DOT conference

[16] Ren, B., Wang, Y., 2004. Numerical simulation of random wave slamming on structures in the splash zone. Ocean Engineering. 31(5-6), 547-560.

[17] DNV·GL, 2014. Loadout, transport and installation of subsea objects, DNVGL-OS-H206.

[18] Li, L., Amer, A.M., Zhu, X., 2020. Numerical analysis of an over-boarding operation for a subsea template. Journal of Ocean Engineering and Science.

[19] Ocean, S., 2018. SINTEF Ocean, SIMO 4.12.1 Theory Manual.

[20] DNV·GL, 2018. Enviromental conditions and enviromental loads, DNVGL-RP-C205.

[21] Solaas, F., Sandvik, P.C., 2017. Hydrodynamic coefficients for suction anchors during installation operations. in ASME 2017 36th International Conference on Ocean, Offshore and Arctic Engineering. American Society of Mechanical Engineers Digital Collection.

[22] Li, L., Gao, Z., Moan, T., 2015. Comparative study of lifting operations of offshore wind turbine monopile and jacket substructures considering vessel shielding effects. The Twenty-fifth International Ocean and Polar Engineering Conference. OnePetro.

[23] Li, L., Zhen, G., Moan, T., et al., 2014. Analysis of lifting operation of a monopile for an offshore wind turbine considering vessel shielding effects. Marine Structures. 39, 287-314.

[24] Næss, T., Havn, J., Solaas, F., 2014. On the importance of slamming during installation of structures with large suction anchors. Ocean Engineering. 89, 99-112.

[25] DNV·GL, 2016. Standard: Marine operations and marine warranty, DNVGL-ST-N001.

[26] Baarholm, G.S., Haver, S., Økland, O.D., 2010. Combining contours of significant wave height and peak period with platform response distributions for predicting design response. Marine Structures. 23(2), 147-163.

[27] Solaas, F., Sandvik, P.C., Pâkozdi, C., et al., 2017. Dynamic forces and limiting sea states for installation of grp protection covers. International Conference on Offshore Mechanics and Arctic Engineering. American Society of Mechanical Engineers.

REVIEW

Current Status and Future Trends for Mooring Systems of Floating Offshore Wind Turbines

Ruyan Yang[1]   Xiangyuan Zheng[1*]   Jinlu Chen[1]   Yufei Wu[2]

1. Institute for Ocean Engineering, Tsinghua University Shenzhen International Graduate School, Guangdong, China
2. Guangdong Provincial Key Laboratory of Durability for Marine Civil Engineering, Shenzhen University, Shenzhen, 518060, China

ABSTRACT

With the increasing demand of energy and the limitation of bottom-fixed wind turbines in moderate and deep waters, floating offshore wind turbines are doomed to be the right technical choice and they are bound to enter a new era of rapid development. The mooring system is a vital system of a floating wind turbine for station-keeping under harsh environmental conditions. In terms of existing floating wind turbine projects, this paper is devoted to discussing the current status of mooring systems and mooring equipment. This paper also presents the mooring analysis methods and points out the technical difficulties and challenges in mooring design, installation, operation and maintenance stages. Finally, the developing trends of the mooring system are summarized, aiming to provide a reference for future mooring research.

1. Introduction

Stimulated by global low-carbon policies and promoted by the development of new energy, the wind energy, a kind of renewable clean energy, has been exploited worldwide for its advantages of sustainability and huge reserves, as well as for the increasing maturity of technologies in power engineering, mechanical engineering and offshore engineering. Compared with the land wind energy, the ocean wind energy is more abundant, more stable, vaster in spaces for exploitation, and of fewer impacts on the environment [1]. The wind power has gained rapid development as of 2021 with a globally accumulated capacity of 837 GW, among which the accumulated offshore capacity (bottom-fixed plus floating) has reached 56 GW. Further, the offshore wind energy is doomed to have a bright prospect in human's history by reaching 380 GW by the end of 2030 and 2,000 GW by 2050 [2].

In the past decades, the majority of offshore wind farms was restricted to the offshore shallow water where

---

*Corresponding Author:
Xiangyuan Zheng,
Institute for Ocean Engineering, Tsinghua University Shenzhen International Graduate School, Guangdong, China;
Email: zheng.xiangyuan@sz.tsinghua.edu.cn

bottom-fixed wind turbines were predominantly deployed. The wind turbine foundations include monopile, jacket, tripod and so on. However, their feasibility is limited by the water depth up to 50 m [3,4]. A higher construction and installation cost will be incurred in moderate and deep waters. By comparison, the floating wind turbine (FWT) is more mobile and flexible to deploy, easier to dismantle, and more suitable for relatively deeper waters. In addition, the deployment site of FWTs is far away from the coastline, eliminating the harm of noise and electromagnetic waves to the environment [5]. Also, compared to nearshore fixed turbines, a larger capacity of turbine like the 9.5 MW units in Kincardine UK can be installed onto floating structures to harness more power so as to achieve a higher levelized cost of energy (LCOE) [6]. All these advantages have pushed FWTs to take on an important historical mission in the development of ocean renewable energy. In recent ten years, more and more FWT projects have been constructed in moderate and even deep waters. Table 1 summarizes the worldwide FWT projects already com-

missioned or being constructed, among which the Hywind Tampen project has reached water depth as deep as 300 m. The accumulated capacity for the commissioned FWTs as of 2021 has exceeded 121.4 MW [2].

For a FWT, its mooring system is a crucial system for the station-keeping purpose. The mooring system generally consists of mooring lines, connectors and anchors. In rough seas, the floating foundation of a FWT interacts with the mooring system and the mooring lines restrain the motion of the floater by providing sufficient restoring forces mainly in horizontal directions. Particularly in extreme environment conditions, the floater's motion displacement, mooring line tension, wind turbine pitch angle and acceleration should meet the requirements of specification in codes and standards, such as DNVGL OS E301, API RP 2SK, API RP 2SM etc. For the design of a mooring system, not only the hydrodynamic performance but also the cost of fabrication and installation should be taken into account [7]. Hence, it is one of the objectives in this paper to review the current status of FWTs' mooring systems.

Table 1. World Floating wind turbine projects and their mooring systems as of July 2022 (commissioned or to be commissioned*)

| Country	Year	Project	Wind turbine Capacity (MW)	Floating Foundation Type	Water Depth (m)	Mooring Type
France	2019	Floatgen	2	Barge	33	Semi-taut
France	2022*	Groix-Belle-ILe	4×6	Semi-Submersible	55-70	Semi-taut
France	2023*	EFGL	3×10	Semi-Submersible	70-100	Catenary
France	2024*	EolMed	3×10	Barge	55	Catenary
Norway	2009	Hywind Ⅰ	2.3	Spar	220	Catenary
Norway	2021	TetraSpar Demo	3.6	Spar	200	Catenary
Norway	2022*	Hywind Tampen	11×8	Spar	260-300	Catenary
Portugal	2020	WindFloat Atlantic	3×8.4	Semi-Submersible	100	Catenary
United Kingdom	2017	Hywind Scotland	5×6	Spar	95-109	Catenary
United Kingdom	2021	Kincardine	5×9.5+2	Semi-Submersible	60-80	Catenary
Japan	2013	Fukushina Ph1	2	Semi-Submersible	120	Catenary
Japan	2016	Fukushina Ph2	7	Semi-Submersible	120	Catenary
Japan	2016	Fukushina Ph3	5	Spar	120	Catenary
Japan	2019	Hibiki	3.2	Barge	55	Catenary
China	2021	Sanxia Yinling	5.5	Semi-Submersible	29.2	Catenary
China	2022*	Haizhuang Fuyao	6.2	Semi-Submersible	65	Catenary

2. Types of Mooring Systems

The mooring systems are classified in a variety of types, according to their mooring line configurations and materials, operation requirements and layout characteristics. Depending on the mooring line configuration, the mooring systems of FWTs mainly include three types, i.e., catenary moorings, taut moorings and tether moorings.

2.1 Catenary Mooring

The catenary mooring refers to a suspended mooring line that is in the shape of a catenary under the effect of self-gravity while the bottom of the mooring line lies on the seabed (see Figure 1). As such, the anchor point only bears horizontal force. The catenary mooring usually uses the steel chain as the material of mooring lines. The restoring force comes from the gravity of the mooring line itself. It is generally applied to the water depth below 1000 m, especially less than 500 m [8]. With the increase of water depth, the length and weight of mooring lines will increase significantly, resulting in a high cost and reduced deck payload of the floater. At the same time, the mooring radius will also increase obviously, affecting the laying of submarine pipelines and ship navigation.
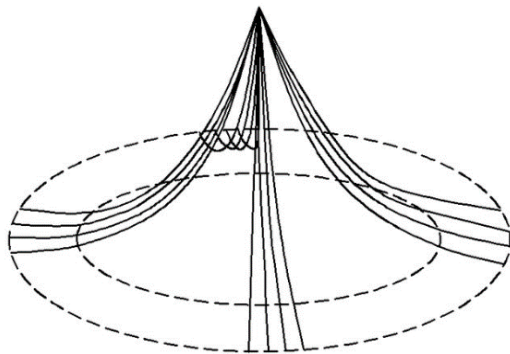

**Figure 1**. The catenary mooring system [9]

So far, the catenary mooring has been most widely used for floating oil and gas platform, as well as FWTs (see Table 1), because of the following advantages: a. The catenary mooring has a simple structure and stable reliability. b. It is economical in the water depth below 500 m. c. The mooring chain has relatively easier fabrication and simpler installation as compared to taut moorings and tether moorings.

The world's first commercial floating wind farm, Hywind Scotland, consists of five 6 MW wind turbines that are 25 km away from Peterhead Scotland. In the water of 95 m ~ 109 m, every FWT adopts a spar foundation with draft of 78 m. Since its center of gravity is lower than the center of buoyancy, the structure has superior stability

even in harsh seas [10]. The five FWTs are anchored to the seabed through three catenary mooring chains. Each mooring chain is about 900 m long with a diameter of 0.09 m. The mooring chains are connected to the floater through a delta connection using the bridle so as to obtain the extra yaw stiffness (Figure 2). The bridle is usually used in spar foundations rather than semi-submersible foundations, because in semi-submersible foundations there is sufficient distance between a fairlead and the center of rotation, leading to enough yaw stiffness. Three suction anchors for each turbine are 5 m in diameter, 16 m tall, with an approximate anchor radius of 850 m [11]. In addition, a special fairlead chain stopper system (see Figure 3) was developed by MacGregor specially for mooring wind turbines in Hywind Scotland wind farm. It can rotate both horizontally and vertically in order to prevent the out-of-plane bending fatigue of the mooring chains [12].
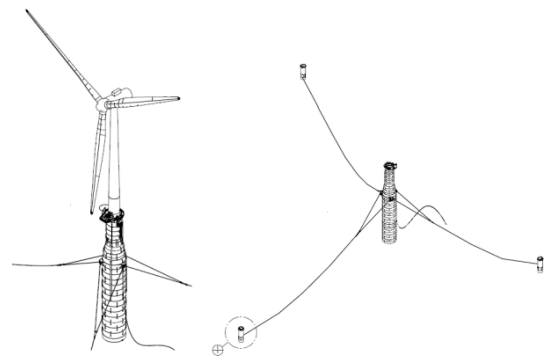
Figure 2. Hywind Scotland mooring system [11]
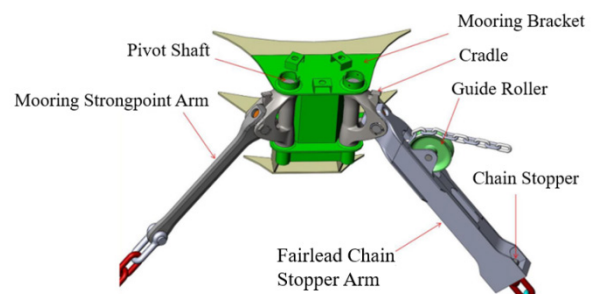
Figure 3. Hywind Scotland fairlead chain stopper system [11]

Sanxia Yinling (Figure 4), the first FWT at the Yangjiang offshore wind farm in Guangdong Province of China, is a FWT demo project with the typhoon-resistant technology. The site is about 30 km offshore with water depth of 29.2 m. The floater adopts a semi-submersible structure of three columns with a diameter of 11.8 m. It has a total displacement (include ballast) of 13,000 t and a design draft of 13.5 m. The mooring system is designed as 3 groups of catenary mooring lines, each composed of 3 mooring lines. Each mooring line is made up of 4 seg-

ments, including a chain segment near the fairlead end, a clump segment, a wire rope segment and a chain segment near the anchor end, from top to bottom. The top end of the mooring line is equipped with a chain stopper and the bottom end is anchored on the seabed by a suction anchor.


Figure 4. China Sanxia Yinling [13]

Nowadays, FWTs are in the high-speed development path towards large tonnage. Also, the new FWT projects will be principally deployed in the water depth of 100 m ~ 300 m. Under this circumstance, catenary moorings will still be the mainstream options in the near future.

2.2 Taut Mooring

The taut mooring system has mooring lines that are taut in tension between the fairlead on the floater and the anchor point on the seabed (Figure 5) such that there are no bottom lying lines. Typically, the angle between the line and the seabed is between 30 degrees and 45 degrees. Therefore, the anchor point should bear both horizontal and vertical forces. Examples of such anchoring structures include suction anchors and vertical load anchors. The taut mooring system usually uses wire ropes, high-strength nylon ropes, polyester cables or other synthetic materials. The recovery force is primarily provided by the axial tensile deformation of the mooring line [14]. In deep water, the taut mooring can greatly reduce the length and weight of mooring lines, as well as the mooring radius. Nonetheless, in shallow water, the stiffness of the mooring line should be very large, excessively increasing the tension of the mooring line. As a consequence, it is more suitable for floaters in deep and ultra-deep waters [8], though over the last two decades a number of applications to wave energy converters in moderate water depths have been realized [15].
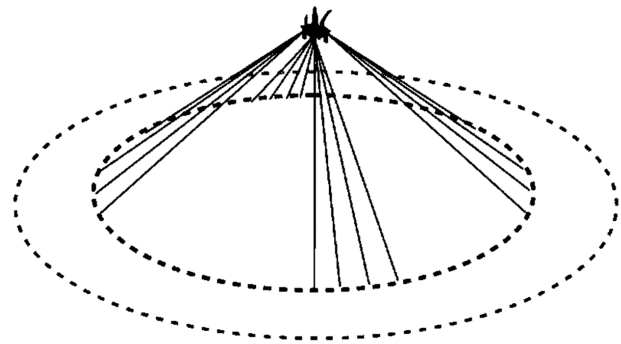

Figure 5. The taut mooring system [9]

In existing FWT projects, only a couple of turbines use semi-taut moorings, such as Floatgen and Groix-Belle-ILe (being constructed) in France (see Table 1). Floatgen has a reinforced concrete foundation designed by Ideol. The foundation is designed as a barge to improve its stability [16] while the damping pool in the central opening of foundation is used to suppress foundation's wave-frequency motions. The dimensions of the square-ring shaped foundation are 36 m in breadth, 9.5 m in height and 7.5 m in draft. Floatgen's semi-taut mooring system consists of six mooring lines, assigned into three groups. From the fairlead to the drag embedment anchor, a single mooring line is composed of a top chain, a nylon cable and a bottom chain. Such an innovative use of nylon cables is a worldwide premiere for the permanent mooring of a large floater in offshore engineering. Simultaneously, the mooring lines are equipped with buoys to prevent friction with the seabed, as well as to balance the self-weight of the mooring lines. Such a novel mooring system satisfies two seemingly paradoxical requirements at the same time. One is the competitive fabrication and installation cost and the other is the ability to keep the floater stable in rough seas [17].

Compared to the catenary mooring system, the taut mooring system possesses the following advantages:

a. The mooring radius is significantly reduced, leading to a smaller seabed area occupied by mooring equipment and fewer risks of collision with other underwater equipment nearby.

b. The restoring stiffness of the mooring line is larger, providing larger restoring forces. Therefore, the horizontal offset of the floater can be greatly reduced.

c. The material of the mooring line has a lighter weight. Thus, not only the self-weight of the mooring system but also the load of mooring system on the foundation is reduced.

d. The length of the underwater mooring line is greatly shortened, making the taut mooring very competitive in cost in deep and ultra-deep waters.

e. The material like nylon and polyester is outstanding

in mechanical performance, especially fatigue resistance and corrosion resistance.
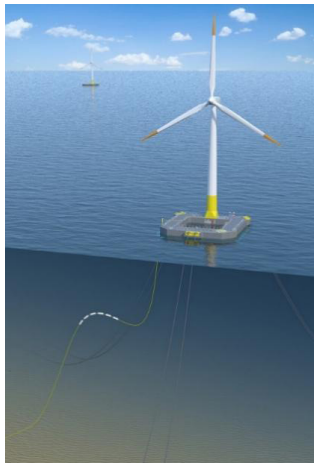

Figure 6. Floatgen and its mooring system [18]

Nonetheless, the mooring lines need to bear huge tension and axial stress under harsh operating states. Under the influence of alternating loads for a long life span, the underwater nylon cables are prone to fatigue failure and material aging. Furthermore, storage, transportation and installation processes all raise strict requirements on cables. In an improper operation, the scrap damage may occur due to cable breakage or abrasion. The sediment entering the cable will also pose a great threat to the mooring system [19]. All these lead to a high cost of fabrication and installation, which is a recognized disadvantage of the taut mooring.

2.3 Tether Mooring

The tension leg platform (TLP) shown in Figure 7 is vertically moored by tendons (also called tethers). The tendon consists of steel tubes with high axial stiffness. The buoyancy of the TLP is greater than its own gravity and the excessive buoyancy is balanced by the pre-tension in tendons. As a result, the stability of the floating foundation principally depends on the mooring system [5]. The anchors like driven piles and gravity anchors are required to withstand large vertical loads. The tether mooring is particularly suitable for the water depth greater than 300 m and its common applications go to oil and gas platforms in Gulf of Mexico. Since the tendons are vertically connected to the seabed, the mooring radius is small.

However, the fabrication process of a tendon is extremely complicated and delicate. Also, the tendon installation requires special installation vessels that can both keep the foundation stable and connect the tendons. Consequently, a high fabrication and installation cost is incurred during tether moorings. In addition, its risks are

enormous. If one tendon fails, the stability of the foundation will suddenly decrease, causing a high risk of capsizing [21]. Due to the pre-tension of tendons, the natural heave frequency of the TLP is extremely high (2 Hz ~ 4 Hz). This will cause high frequency response problems, such as springing and ringing [22]. For these reasons, the tether moorings have not been used on a large scale for FWTs yet. The TLP concept for a FWT stays at the stage of small-scale tests and numerical calculations.
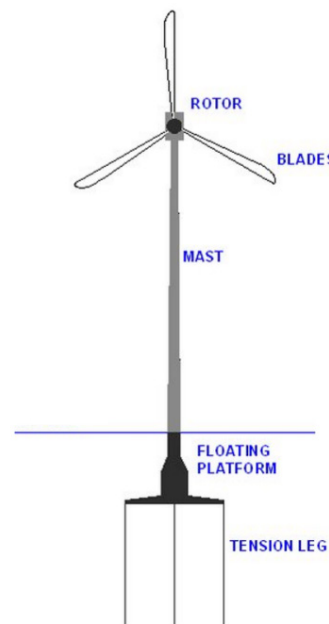
Figure 7. Sketch of FWT with tether mooring [20]

The GICON-SOF project (see Figure 8), a tension-leg FWT with the tether mooring, was initiated in 2009. The floating foundation consists of four columns, anchored to the seabed by four vertical tendons and additional eight slanting tendons. In 2013, a 1:37 scaled model test of the GICON-SOF 2 MW foundation was carried out at the Maritime Research Institute Netherlands (MARIN) [23,24]. In 2016, the combined wind and wave tests were conducted for a 6 MW turbine on the GICON-SOF foundation and the experimental results showed very satisfactory performance for its stability. Though it was reported that GICON-SOF would have prototype sea trials with a 6 MW ~ 8 MW turbine [25], so far no trials have been implemented.

2.4 Other Classifications of Moorings

Depending on the duration of the offshore operation, mooring systems are classified into two categories, temporary moorings and permanent moorings. The temporary mooring is applied to temporary platforms or vessels that operate for periods ranging from a few days to several months, while the permanent mooring is used for floating

structures that operate in fixed sea areas for a long time. In terms of the design life, the operation time can be several years or several decades.
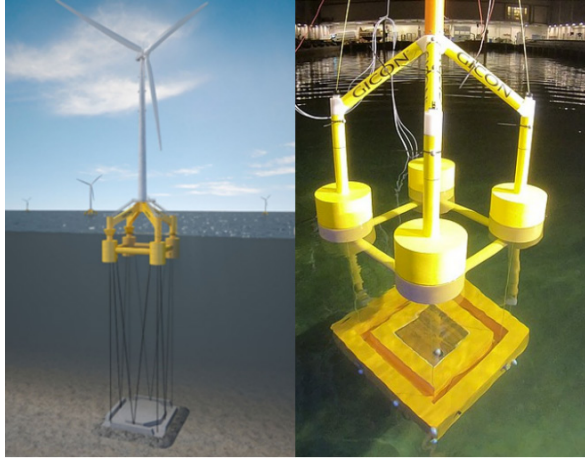
Figure 8. GICON-SOF project (left) and its model test (right) [26]

The mooring systems can also be categorized into spread moorings and single-point moorings according to the requirement of restricting the heading of the floater. The spread mooring, where mooring lines are distributed around the platform, can restrict the offset and heading of the platform from all directions. The single-point mooring is often used for ship-shaped floating structures under severe sea conditions with frequent changes in wind, wave and current directions. It has one or more mooring lines connected with the rotating center, so that the floater has a weathervane effect and can rotate with the direction of wind, waves and currents. The single-point mooring is commonly used in the floating production storage and offloading (FPSO). Though the single-point mooring has not been applied to an actual FWT project, it was adopted by the Eolink [27] FWT concept (Figure 9). Unlike most FWTs, it can spin around its rotating center to face the wind. The patented single point mooring is able to withstand large tide range in shallow water as well [27], but this concept has not been applied to real FWT project yet.
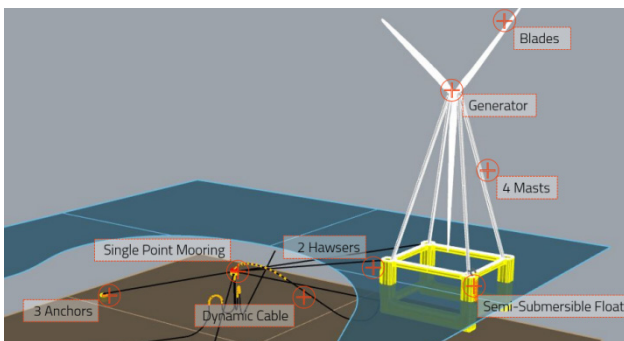

Figure 9. Eolink with single-point mooring [27]

3. Mooring System Equipment

The mooring system for FWTs chiefly contains mooring lines, anchors and connectors. This section discusses the current status of mooring equipment.

3.1 Mooring Lines

3.1.1 Chain

The chain is a common mooring line component with a simple connection and good abrasion-resistance property. The mooring chain is made of a plurality of steel links welded and connected with each other. According to the link form, chains are divided into two kinds: stud-link chains and stud-less chains (Figure 10). The stud-link chain has a stud in the middle to prevent it from entangling and it is often used for temporary moorings, requiring multiple retractions. The stud-less chain, without a stud inside, is about 10% lighter than the stud-link chain with the same breaking strength. There are other advantages for the stud-less chain. For example, there is no loosening of the stud, no cracks at the joints of the stud and it is easier to fabricate and inspect. As a result, the stud-less chain is preferred for permanent moorings.
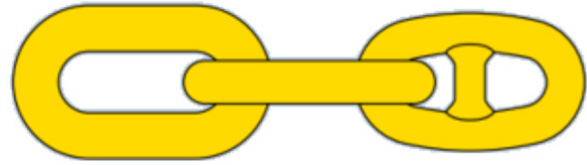
Figure 10. Stud-less chain (left) and stud-link chain (right) [9]

Chains have a wide variety of diameters and grades. The nominal diameter of ocean engineering chains ranges from 70 mm to 200 mm. The classification standard provides several grades based on tensile strengths, shown in Table 2. The grades include R3, R3S, R4, R4S, R5 and R6. R7 is still under development.

Table 2. The performance of different grades of mooring chains [29]

Grade	Yield Stress (N/mm²)	Tensile Strength (N/mm²)	Elongation (%)
R3	410	690	17
R3S	490	770	15
R4	580	860	12
R4S	700	960	12
R5	760	1000	12
R6	900	1100	12

In terms of manufacturers, the Jiangsu Yaxing company in China can produce ultra-high strength R6 chains that have been successfully used in a deep-water drilling plat-

form. Such chains meet the latest international codes and standards, reaching an internationally advanced level.

3.1.2 Wire Rope

The wire rope is made up of multiple strands of metals that wound into a spiral. The wire rope in mooring system usually includes six strands, eight strands and spiral strands, shown in Figure 11. Generally, with more strands, the wire rope has a greater breaking strength, but a heavier weight and a higher fabrication cost. Six strands and eight strands are preferred in the temporary mooring. They are easier to fabricate because they can bend on a winch. Nevertheless, they tend to produce rotational torque when stretched, causing torsion of the wire rope. By contrast, spiral strands are torque neutral, since they have multiple layers wound in opposite directions. Moreover, the spiral wire rope has better corrosion resistance due to its compact structure. The uniform surface of the spiral wire rope also makes it easier to be sheathed, such as the polyurethane sheath. Based on the above advantages, the spiral wire rope is suitable for permanent moorings [30].

Under the same breaking load, the wire rope is lighter and more elastic than the chain, but the structure of the wire rope is more complicated and vulnerable, and its fabrication and installation costs are higher. It is often used in taut moorings or as the middle division of catenary moorings. As for manufactures, the Juli company in China supplies various types of wire ropes such as 1870, 1960, 2160 etc. Globally, the Neptune company in Singapore and the Bridon company in UK have leading manufacturing capabilities [8].
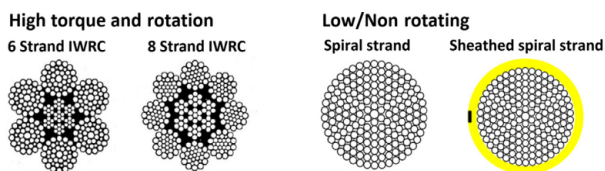

Figure 11. Various types of wire ropes [7]

3.1.3 Synthetic Fiber Rope

The materials of synthetic fiber ropes involve polyester, high molecular polyethylene (HMPE), aramid, and so on. The structural composition of a synthetic fiber rope is shown in Figure 12. Due to its elastic property, the synthetic fiber rope is appropriate for taut moorings. Nonetheless, the complex mechanical properties of synthetic fiber ropes bring new challenges to mooring analysis, including its variable stiffness, creep and slack-taut issues.
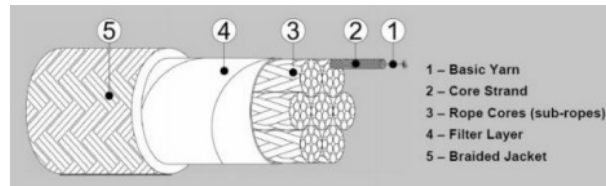

Figure 12. Composition of a synthetic fiber rope [31]

In deep water, the synthetic fiber rope is propitious to reduce the weight and length of mooring lines. The main advantages of synthetic fiber rope include high elasticity, high strength (900 MPa or higher) and low weight. To be specific, under the same breaking force the mass per unit length is only 1/10 of that of the chain or 1/3 of that of the wire rope and the weight is even lighter in water. Additionally, it possesses prominent fatigue resistance performance and excellent corrosion resistance performance [32]. Nevertheless, it is likely to be damaged by sharp objects. Sands would also invade the jacket and damage the rope.

Concerning the manufactures, Lankhorst in Netherland has more than 200 years of manufacturing experience. Its GAMA98 synthetic fiber rope is made of parallel rope cores within an outer jacket. The tension and length of each parallel rope can be precisely controlled during fabrication [33]. The Sixiong rope industry in China completed the production and manufacturing of synthetic fiber ropes that have been successfully used by the CNOOC Lingshui17-2 project for offshore gas exploitation, achieving a huge breakthrough in the field of mooring rope manufacturing.

3.2 Anchors

The choice of anchors is mainly determined by the water depth, the condition of soil and the load type that the anchor point needs to bear. Also, the cost of transportation and installation is a key factor. Typical ocean engineering anchors are shown in the Figure 13, categorized by water depths (shallow to ultra-deep) and soil types (hard to soft).

3.2.1 Gravity Anchor

The gravity anchor is the simplest and oldest anchor foundation in existence. It provides anchor force through the friction with the seabed and its own weight. As a result, the gravity anchor is generally large in size and usually made of steel and concrete. Normally, it is inexpensive to install, but only suitable for medium to hard soil conditions and difficult to remove during decommissioning.

3.2.2 Driven Pile

The driven pile is a hollow steel pipe that can bear

both horizontal and vertical loads generated by the friction resistance between the pile and the surrounding soil. In general, the driven pile must be driven deep enough below the seabed to achieve the desired holding capacity. It is usually installed by pilling hammers or vibratory hammers. There are also some limitations of the driven pile. For instance, the disturbance to the seabed cannot be ignored. Also, when the water depth exceeds 1000 m, the strict installation requirements for equipment leads to a great difficulty of piling. Three driven piles have been used in Haizhuang Fuyao in China.
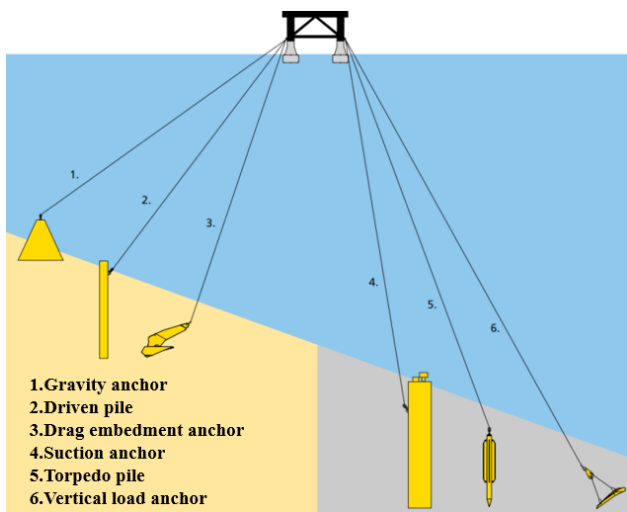

Figure 13. Typical mooring anchors [9]

3.2.3 Drag Embedment Anchor

The drag embedment anchor is one of the most commonly used anchors presently. It offers the horizontal load in the same direction as the installation direction. It is for this reason that the drag embedment anchor is often used in catenary moorings. In addition, certain drag embedment anchors are capable of offering vertical forces now. Generally, the main soil resistance occurs in front of the anchor, and therefore the resistance largely depends on its fluke area [34]. Drag embedment anchors have been used in Floatgen France, Hibiki Japan, WindFloat Atlantic Portugal and so on.

3.2.4 Suction Anchor

Suction anchors are suitable for a wide range of water depths, mainly used in clay, sand and granular layers. Recent applications to FWT projects include Hywind Scotland UK, Sanxia Yinling China, Hywind Tampen Norway etc., among which the Hywind Scotland and the Hywind Tampen use a shared anchoring system. The suction an-

chor can withstand large horizontal and vertical loads of mooring lines. It must be specially designed for soil conditions. Moreover, it is complex to construct and expensive to install. Divers or remote operated vehicles (ROV) are required to install and remove the submersible pumps. The suction anchor is generally a steel cylindrical pipe with an open bottom and a closed top. When installed, the suction anchor is lowered to the seabed and the lower edge of the pipe is embedded into the soil by its own weight. Then, the water in the suction pile is continuously pumped out to reduce the pressure inside the cylinder. The vertical pressure produced by the internal and external pressure difference acts on the top of the pipe, so that the pipe will be continuously pressed into the soil until the cylinder body is all drained and the bottom is closed [35] (Figure 14). In this figure, 'L' denotes the depth to which the suction anchor sinks under the force from hydrostatic pressure difference.
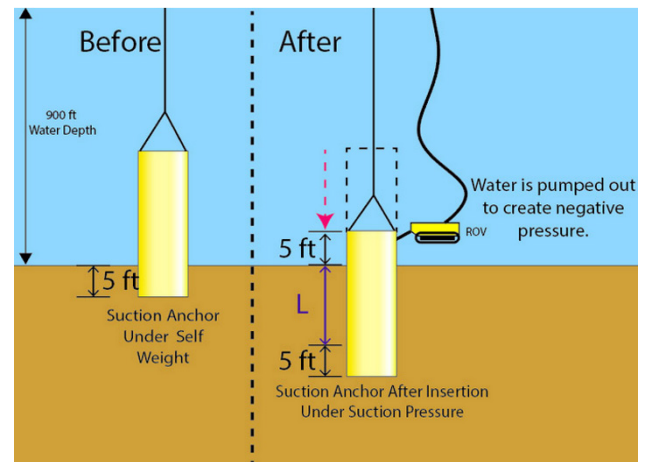
Figure 14. Installation process of the suction anchor [36]

3.2.5 Torpedo Pile

The torpedo pile, driven into the seabed by its own kinetic energy, can withstand both horizontal and vertical loads. The torpedo pile has a small size and good pullout resistance. Also, it is omnidirectional and self-installed, so that it is adaptive for ultra-deep water. Nevertheless, considerations arise to the large usage of steel and its inability to recycle.

3.2.6 Vertical Load Anchor

The vertical load anchor is installed in the same way as the drag embedment anchor, but it penetrates deeper into the soil. The vertical load anchor can bear both horizontal and vertical loads. It is primarily utilized in deep-water moorings.

3.2.7 Summary

Driven piles, drag embedment anchors and suction anchors have been widely applied to FWT projects. Gravity anchors are often used for FWTs in shallow waters provided the soil penetration is sufficiently deep. Torpedo piles and vertical load anchors are not in practical use for FWTs while they have been popularly adopted in deep-water oil and gas exploration. Nonetheless, as the offshore wind development trends towards deep waters, torpedo piles and vertical load anchors will become the potential choice.

3.3 Connectors

Connectors are used to connect the mooring line components. Common connectors in marine engineering include shackles, kenter shackles, pear shackles and swivels. However, due to the limited fatigue life, they can only be used in temporary moorings rather than permanent moorings.

Since it is hard to inspect and replace connectors in permanent moorings, the connector must be robust and durable. The recommended connectors in permanent moorings include long term mooring (LTM) D-shackles and H-shackles. D-shackle (Figure 15 left) consists of a bow component and a pin component. H-shackle (Figure 15 right), named for its shape, can be used to connect chains to chains, chains to wire ropes, chains to synthetic fiber ropes etc. Other types of connectors may be allowed to use in permanent moorings if the fatigue life and the structural strength are qualified.

Figure 15. D-shackle (left) and H-shackle (right) [7]

4. Mooring Analyses

This section is committed to discussing the differences and features of mooring analysis methods including static, quasistatic and dynamic analyses, frequency-domain and time-domain analyses, uncoupled and coupled analyses.

4.1 Static, Quasistatic and Dynamic Analyses

Generally, the motion responses of a floater under environmental loads can be divided into three categories of motions: steady state, low frequency and wave frequency. The response of a mooring system in the steady state can be obtained by static analysis. Meanwhile, the low-frequency response can be analyzed by a static method as well, for the period of the motion is long [37]. One of the typical methods of static analysis is the catenary equation method in which the environmental loads are regarded as static, in order to determine the equilibrium position of the floater, the geometric shape of the mooring lines and the tension distribution along the mooring lines. However, the static analysis ignores the coupling between the foundation and the mooring system, the fluid force on the mooring lines and the elastic deformation of the mooring lines, etc. As a result, the static method can hardly meet the requirements of accuracy when the floater is expected to experience large motions and it is only applicable to the preliminary design of a mooring system.

Following the preliminary design, the dynamic response of the whole system should be determined. In this process, the usually adopted methods include the quasistatic analysis and the dynamic analysis. The quasistatic approach ignores the vertical motion of the mooring system and the dynamic effects of the mooring lines, i.e., added mass, damping, drag force and fluid acceleration. In this approach, the motion of the foundation is subdivided into various instantaneous states and the equilibrium position is acquired by using the static analysis for these instantaneous states. The main shortcoming of this method is that it does not consider the influence of the dynamic effects of the mooring lines on floater's wave-frequency motions. Hence, if wave-frequency impact is negligible, the quasistatic method can be used to predict the response of the whole system. Furthermore, it has been proved [38] that the quasistatic method can achieve satisfactory prediction by using a safety factor with high efficiency.

On the contrary, the dynamic analysis accounts for the time varying properties of the mooring lines. Such an approach is able to accurately simulate the nonlinear characteristics, such as the nonlinear hydrodynamic force on mooring lines, the nonlinear deformation of the mooring lines, and the friction between the mooring lines and seabed, etc. The commonly used methods in dynamic analysis include the finite element method and the centralized mass method. Kwan [37] figured out that the ratio of tensions calculated by dynamic analysis to those calculated by quasistatic analysis is in the range of 1.2 to 19.5. In general, the dynamic analysis is recommended to predict

the responses of floater and mooring lines.

4.2 Frequency-domain and Time-domain Analyses

Frequency-domain analysis is a simple and efficient technique. In frequency-domain analysis, the response of the system is made up of frequency-dependent components and solved by the principle of linear superposition of different frequencies. Moreover, the frequency-domain analysis not only determines the motions of the floater and the tension of the mooring lines separately, but also analyzes the mean response, low frequency response and wave frequency response respectively as well. The recommended analysis procedures provided in API RP 2SK [39] are shown as follows:

a. Determine the mean environmental loads acting on the floater and predict the equilibrium position using static analysis.

b. Determine the low-frequency motion using hydrodynamic analysis. In this process, the mooring stiffness at the equilibrium position is required.

c. Determine the wave-frequency motion using RAOs.

d. Determine the motions of the floater and the tension of the mooring lines using dynamic or quasistatic analysis.

e. Compare the maximum offset and maximum mooring line tension against the design criteria.

However, when using the frequency-domain analysis, its limitations should be noticed. This approach is linearized, and therefore it approximates the nonlinearities including the nonlinear deformation of the mooring lines, geometric nonlinearity, fluid loads and bottom friction etc. Furthermore, the extreme value is obtained from statistical distributions rather than directly from time-domain simulations. On the other hand, though the nonlinear spectral analysis can be adopted for the dynamic analysis, due to its complexity it is seldom used by engineers.

The time-domain analysis is more time-consuming but more accurate than the frequency-domain analysis. It is able to simulate all nonlinearities. Also, the time-domain analysis accounts for the coupling between the mean response, low-frequency response and wave-frequency response. The steps recommended by API RP 2SK [39] are summarized as follows:

a. Establish the hydrodynamic model including the floater and the mooring systems simultaneously. Determine the wind force and current force coefficients.

b. Run the time-domain simulation in the mooring analysis software (like OrcaFlex) and repeat it several times for different seeds.

c. Obtain the extreme value of the floater offset and the mooring lines tension by a proper statistical analysis method.

d. Compare the maximum offset and maximum mooring line tension against the design criteria.

The time-domain analysis is especially preferred for shallow water moorings, mooring lines with composite materials and/or other nonlinear situations, while the frequency-domain analysis is chosen for its efficiency.

4.3 Uncoupled and Coupled Analyses

In uncoupled analysis, the response of the floater and the mooring system are analyzed separately by two independent steps. The first step is to obtain the motion response of the floater based on the three-dimensional potential theory, where the effects of the mooring system are simulated as nonlinear displacement-dependent forces. Subsequently, the motion response of the floater is regarded as the excitation at the top end of the mooring lines and the dynamic response of the mooring lines is gained [40]. In this approach, the damping forces from the mooring system are either neglected or simplified as linear forces acting on the floater. In addition, usually the current loads on the mooring system are also not considered.

However, the foundation and the mooring system are coupled with each other in reality. Besides, the uncoupled method may produce substantial errors especially in deep water environment where the current loads is pronounced and the damping from the mooring system is remarkable [41]. Consequently, in this situation, the coupled analysis is required to determine the interaction between the floater and the mooring system. In the coupled analysis, the rigid model of the floater together with the slender model of the mooring system are solved simultaneously through the nonlinear time-domain analysis. The coupled response is obtained at every time step in order to fully capture all coupling effects such as stiffness, damping and inertia forces [42]. This approach is accurate though it is somehow time-consuming. Nowadays, the coupled analysis is routinely used in the offshore wind industry. Several software has the capacity of doing coupled dynamic analysis for a FWT in the multi-hour storm.

5. Key Challenges and Development Trends of Mooring Systems

5.1 Key Challenges of Mooring Systems

This section is dedicated to the technical difficulties in engineering practice and challenges in research and development of the mooring system from its whole life cycle: design, installation, operation and maintenance stages.

5.1.1 Challenges in Design Stage

Design for shallow-water moorings

The design for the deep-water mooring is relatively straightforward, as it is a proven technology in offshore engineering. But for a FWT in shallow-water environment, if catenary moorings are adopted, the length of chains need to be extremely long and the mooring radius usually reaches ten or twenty times of the water depth, in case that the anchor point is pulled up from the seabed when the maximum offset occurs. Even if a clump is connected to the chain to lessen the chain length, the mooring radius is still more than ten times of the water depth. Therefore, the amount of mooring chains used in shallow water is enormous, resulting in a high cost and ineffective use of ocean farm space. Sometimes, the cost of the mooring system may approach or even exceed the cost of the foundation itself.

Similarly, the taut mooring is also hard to be applied in shallow-water environment. When subjected to large environment loads like wind and waves, a FWT's motions may be remarkable. The taut mooring line needs to bear the station-keeping loads through its elastic deformation. Due to its large stiffness, the mooring line therefore experiences huge dynamic tension. The peak dynamic tension is more than ten times larger than the tension at the static offset. As the displacement of a floating megawatt turbine is becoming larger and larger, such a dynamic response characteristic of taut mooring inhibits its application to shallow-water power exploitation [43-45].

Slack-taut issue of mooring lines

Due to floater's motions, particularly sway, surge and heave, the slack-to-taut cyclic process frequently occurs in mooring lines, accompanied with snap tension. The snap tension can be several times or even a dozen times larger than the mean tension [46], causing the rupture of mooring lines to take place. This would quickly make mooring lines fail and would seriously affect the station-keeping of the foundation [47,48]. Thus, when the aero-hydro-servo-elastic coupling analysis is conducted for predicting the dynamic response of a FWT, the snap tension in mooring lines needs to be taken into account. Nonetheless, how the slack-taut cycles develop in mooring lines is unclear, not alone the detailed influence factors and the controlling mechanism of snap tension in mooring lines.

Nonlinear problems of mooring line materials

The elastic modulus of the wire rope is usually considered as a constant for its linear elasticity. Differentially, the polyester fiber rope has viscoelastic property, that is, the fiber rope has both elastic property of solid deformation and viscous property of liquid flow. Its stiffness changes with motion period, smoothness and load duration [49]. As a result, it is difficult to directly simulate the dynamic characteristics of the polyester fiber rope. For a composite material mooring system, the recovery stiffness of the whole mooring system is nonlinear because the material properties of distinct mooring materials are completely different. This makes numerical modelling more complicated and numerical simulation more time-consuming. Further, for a hybrid mooring, since segmented calculations are often adopted, the issue of discontinuous stiffness emerges.

5.1.2 Challenges in Installation Stage

Twist in mooring lines

The long-term integrity of the mooring system is so critical that the twist introduced in mooring lines should be zero or minimized during the pre-lay of mooring lines and the final hook-up to the floating foundation. If twist exists in the wire rope, it will be easy to induce bird-caging and premature failure. And if twist exists in the chain, it will significantly reduce its strength and fatigue performance. Therefore, it is essential to take additional protective measures to avoid introducing twist during the installation process, despite increasing installation time and cost. At present, the effective methods to forestall twist include the use of low-torque pull-in lines, the use of a second line to balance the torque and the use of in-line swivels.

It is also worth mentioning that nowadays the accurate level of twist acceptance in the mooring system remains unclear. Under different levels of twist, neither could the long-term performance of chains or wire ropes be predicted precisely. Currently, only rough guidelines are available to use, but there is no baseline. Hence, it is an urgency to develop systematic data for the torque-twist behavior of chains and wire ropes, in order to predict the reduced strength and fatigue life.

Damage to mooring lines

During installation, damage to wire ropes may occur. Special care should be taken during the operation of extracting wire ropes from the installation reel. During this process, the wire rope would easily get crushed or tangled. A proper operation to prevent knotting is to pull the wire rope straight down from a reel or mount it on a revolving stage. If damage occurs, the remedial measure should be taken, for example, to provide additional corrosion pro-

tection in the damaged sheath area. But if damage occurs in deep-water operations, the cost of damage assessments and remedial measures would be much higher [50].

5.1.3 Challenges in Operation and Maintenance Stage

Development of mooring line tension monitoring system

For station-keeping and sea-keeping of a FWT, it would be helpful if the time-varying mooring line tension can be timely and accurately recorded. From the monitoring system, precious on-site measurement data, cognition of marine environment and adaptability of floating foundation can be all acquired to improve the technology of integrity management.

The traditional technique for mooring line tension monitoring system is to infer the mooring line tension by measuring the mooring line angle. Such a technique is of great uncertainty in the calculation process [51]. Moreover, most of existing mooring line tension monitoring systems stop functioning after two years of operation due to the harsh environment [52]. For an advanced monitoring system, the automatic design of linkage for adjusting operation needs to be involved. Presently, it is still a great challenge to develop a tension monitoring system with accurate measurement, long service life and advanced automation [53].

Increasing complexity of mooring operations

As the amount of subsea infrastructure quickly grows, many new operations are carried out next to existent infrastructure. Consequently, the operators have to work close to the existing subsea facilities and pipelines. For catenary moorings and taut moorings, it is relatively easier to carry out the operation and maintenance operations for a FWT, because the foundation can be easily disconnected with the mooring system and towed back to the port for maintenance. But for tether moorings, special attention needs to be paid to when removing the tendons from the foundation. Any improper operation may give rise to the capsizing of the floater especially for a FWT whose center of gravity is taller than that of an oil platform.

5.2 Developing Trends of Mooring Systems

Hybrid mooring system concept

The traditional mooring system has its own applicable scope and limitations. Aforementioned, the catenary mooring has a too large mooring radius and too long mooring chains, while the taut mooring has excessive dynamic tension. Accordingly, the hybrid mooring system concept was brought up to solve these problems.

One kind of hybrid mooring concepts is the usage of clumps and buoys. Clumps increase the restoring force of mooring lines, and therefore restrict the floater's offset under extreme conditions. The application of buoys helps to increase the vertical distance between mooring lines and other subsea equipment. Also, buoys can offset the weight of mooring chains partly supported by the floater. A new hybrid mooring system was proposed for a semi-submersible foundation by Yuan et al. [54] Buoys and clumps were respectively connected to the top and bottom of a traditional taut mooring line. It was reported that the tension of the mooring lines was greatly reduced. Xu et al. [55] analyzed and compared three different hybrid mooring systems and carried out a series of wave model tests to investigate their mooring performance. Through this research, a new hybrid mooring system was recommended to significantly reduce the dynamic tension.

The other kind of hybrid mooring concept consists of several segments, each of a different mooring material [56]. The mooring line comprises a bottom chain, a high modulus polyethylene rope, a polyester rope and a top chain from the bottom to top. Such a hybrid mooring system is able to offer an appropriate stiffness and to resist the abrasion between the mooring line and the seabed simultaneously.

Shallow-water mooring

Presently, almost all FWT projects commissioned are located in moderate and shallow waters, since the cost and technical challenges incurred from environmental conditions (i.e. wind and waves) rapidly grow with increasing offshore distance and water depth. The more mature bottom-fixed wind turbines can be a good usher for FWTs. But as mentioned in Section 5.1.1, traditional mooring systems are not suitable for shallow water. So far there is no mooring system with good mooring performance and competitive cost for the deployment of FWTs in shallow water. The recent Sanxia Yinling FWT project has encountered the mooring embarrassment in 29.2 m water depth [13]. More and more studies have been carried out to deal with shallow-water mooring. Benassai et al. [57] analyzed the motion performance of the tri-floater wind turbine at a water depth of 50 m ~ 200 m, considering both catenary moorings and taut moorings. A series of parametric studies were carried out to identify the better mooring configuration. Campanile et al. [58] studied the effects of mooring line number, foundation admissible offset and space between adjacent turbines in water depths of 50 m ~ 80 m and 200 m ~ 300 m. Besides, the cost of installation

and maintenance was preliminarily analyzed. Xu et al. [43] put forward seven mooring concepts for a FWT in the water depth of 50 m and compared the concepts in terms of reliability and cost. In their study, six mooring design concepts were recommended for future research.

New mooring material

The high performance of the synthetic fiber rope is beneficial to its application in the mooring system. Different synthetic materials lead to the diversity of synthetic fiber ropes. In addition to a large number of applications of polyethylene terephthalate (PET), nylon, high modulus polyethylene, new synthetic fiber materials with higher performance are being developed, such as polyethylene naphthalate (PEN) and liquid crystal aromatic polyester (LCAP) etc.

By comparison, PEN has a better mechanical performance and it is about twice as stiff as the conventional grade of PET. Furthermore, its performance of ultraviolet resistance and availability to maintain strength in a wet environment are better. However, the manufacturing capacity of PEN is limited and the cost is rather high.

LCAP is one of polyester materials. It is much stronger and stiffer than traditional synthetic fiber materials. It can avoid axial compression fatigue, creep and abrasion problems. At present, the supply of LCAP is very limited. Consequently, the cost is more expensive than any other synthetic material [59,60].

6. Conclusions

This paper summarizes the current status of the mooring system and the mooring equipment of FWTs, and points out the features of mooring analysis methods and the technical challenges. The developing trends of the mooring system are also given. The conclusions are drawn as follows:

1) Common mooring systems applied to FWTs include catenary moorings, taut moorings and tether moorings. The design and analysis show that the catenary mooring is suitable for medium water depth, while the taut mooring and the tether mooring could be applicable to deep waters. A mooring system particularly suitable for shallow water has not been developed yet, whereas the FWT era is embracing seas of moderate depth, as reflected in Table 1. At present, most of the existing FWT projects adopt catenary moorings and a few projects adopt semi-taut moorings. Tether moorings are still in the stage of model tests. Some hybrid concepts can reduce the motion of a FWT under extreme environmental conditions and offer competitive cost as well, but they still need further research.

2) The mooring system still has some technical difficulties and challenges in its whole life cycle of design, installation, operation and maintenance stages: In the design stage, outstanding issues include the design for shallow-water moorings, the influence mechanism of slack-taut process on the tension response of the mooring system, and the nonlinearity of mooring line materials. In the installation stage, special attention should be paid to avoid the twist in mooring lines and the damage to mooring lines. In the operation and maintenance stage, it is urgent to develop an advanced mooring line tension monitoring technology.

3) The moving trends in mooring research include transformation from traditional mooring schemes to hybrid moorings, from deep water to moderate and shallow waters, and from traditional mooring materials to high-performance composite mooring materials.

Acknowledgement

Conflict of Interest

There is no conflict of interest.

References

[1] Manwell, J.F., Mccowan, J.G., Rogers, A.L., 2006. Wind Energy Explained: theory, design and application. Wind Engineering. 30(2), 169-170.

[2] Williams, R., Zhao, F., Lee, J., 2022. GWEC. Global Wind Report 2022. Global Wind Energy Council. Brussels, Belgium.

[3] Henderson, A.R., Witcher, D., 2010. Floating offshore wind energy—a review of the current status and an assessment of the prospects. Wind Engineering. 34(1), 1-16.

[4] Campanile, A., Piscopo, V., Scamardella, A., 2018. Mooring design and selection for floating offshore wind turbines on intermediate and deep water depths. Ocean Engineering. 148, 349-360.

[5] González, S.F., Diaz-Casas, V., 2016. Present and future of floating offshore wind. Floating offshore wind farms. Springer, Cham. 1-22.

[6] Lerch, M., De-Prada-Gil, M., Molins, C., et al., 2018. Sensitivity analysis on the levelized cost of energy for floating offshore wind farms. Sustainable Energy Technologies and Assessments. 30, 77-90.

[7] Ma, K.T., Luo, Y., Kwan, C.T.T., et al., 2019. Mooring system engineering for offshore structures. Gulf Professional Publishing.

[8] Zhao, J.R., Feng, W., Li, X.K., 2013. Development status of multipoint mooring system in deep water. Oil Field Equipment. 42, 1-7.

[9] Anchors, V., 2015. Anchor manual 2015–the guide to anchoring. Rotterdam: Vryhof Anchors.

[10] Equinor. Equinor - the world's leading floating offshore wind developer. (2022-07-31). https://www.equinor.com/en/what-we-do/hywind-where-the-wind-takes-us.html.

[11] Equinor. Statoil to build the world's first floating wind farm: Hywind scotland. (2022-07-31). https://www.equinor.com/en/news/hywindscotland.html.

[12] Hole, K.B., 2018. Design of Mooring Systems for Large Floating Wind Turbines in Shallow Water. NTNU.

[13] Sanxia Energy. Sanxia Yinling: China's first floating offshore wind turbine. (2021-08-13) [2022-07-31]. https://wind.in-en.com/html/wind-2405763.shtml. 2021.

[14] Jefferys, E.R., Patel, M.H., 1982. On the dynamics of taut mooring systems. Engineering Structures. 4(1), 37-43.

[15] Qiao, D., Haider, R., Yan, J., et al., 2020. Review of wave energy converter and design of mooring system. Sustainability. 12(19), 8251.

[16] Pham, H.D., Schoefs, F., Cartraud, P., et al., 2019. Methodology for modeling and service life monitoring of mooring lines of floating wind turbines. Ocean Engineering. 193, 106603.

[17] Alexandre, A., Percher, Y., Choisnet, T., et al., 2018. Coupled analysis and numerical model verification for the 2MW Floatgen demonstrator project with IDEOL platform. International Conference on Offshore Mechanics and Arctic Engineering. American Society of Mechanical Engineers. 51975, V001T01A032.

[18] Floatgen, France's First Offshore Wind Turbine. (2022-07-31). https://floatgen.eu/en/press-publications.

[19] Bach-Gansmo, M.T., Garvik, S.K., Thomsen, J.B., et al., 2020. Parametric study of a taut compliant mooring system for a FOWT compared to a catenary mooring. Journal of Marine Science and Engineering. 8(6), 431.

[20] Tomasicchio, G.R., Armenio, E., D'Alessandro, F., et al., 2012. Design of a 3D physical and numerical experiment on floating off-shore wind turbines. Coastal Engineering Proceedings. 1, 67.

[21] Bea, R.G., Cornell, C.A., Vinnem, J.E., et al., 1994. Comparative risk assessment of alternative TLP systems: Structure and foundation aspects.

[22] Kim, C.H., Zhao, C., Zou, J., 1995. Springing and ringing due to nonlinear waves on a coupled TLP. The Fifth International Offshore and Polar Engineering Conference. OnePetro.

[23] Adam, F., Steinke, C., Dahlhaus, F., et al., 2013. GICON®-TLP for wind turbines–validation of calculated results. The Twenty-Third International Offshore and Polar Engineering Conference. OnePetro.

[24] Adam, F., Myland, T., Dahlhaus, F., et al., 2014. Gicon®-TLP for wind turbines—the path of development. The 1st International Conference on Renewable Energies Offshore (RENEW). 24-26.

[25] GICON-SOF. Development of A Floating Foundation for Third Generation Wind Turbines with The University Of Rostock. (2022-07-31). http://www.gicon-sof.de/en/sof1.html.

[26] GICON & GLOSTEN n.d. Glosten and Gicon partnership. glosten.com: Glosten. (2022-07-31).

[27] Eolink Cost-effective Floting Wind Farms. Proven shipyard technologies. (2022-07-31). https://www.eolink.fr/en/concept.

[28] Guyot, M., De Mourgues, C., Le Bihan, G., et al., 2019. Experimental offshore floating wind turbine prototype and numerical analysis during harsh and production events. International Conference on Offshore Mechanics and Arctic Engineering. American Society of Mechanical Engineers. 59353, V001T02A004.

[29] DNV. GL. DNVGL-OS-E302: Offshore mooring chain. 2015.

[30] Lunde, T.H., 2021. Roksvaag T B, Solheim S. Mooring of Floating Offshore Wind Turbines. NTNU.

[31] Chakrabarti, S., 2005. Handbook of Offshore Engineering (2-volume set). Elsevier.

[32] Petruska, D.J., Kelly, P., Stone, B., et al., 2010. SS: Fiber Moorings, Recent Experiences and Research: Updating API RP 2SM on Synthetic Fiber Rope for Offshore Moorings. Offshore Technology Conference. OnePetro.

[33] Song, B.T., Jiang, R.X., Li, T., 2021. Application and development status of synthetic fiber cables for marine engineering at home and abroad. Technical Textiles. 1, 77-79.

[34] Zimmerman, E.H., Smith, M., Shelton, J.T., 2009.

Efficient gravity installed anchor for deepwater mooring. Offshore technology conference. OnePetro.

[35] Zhao, Y., Liu, H., 2016. Numerical implementation of the installation/mooring line and application to analyzing comprehensive anchor behaviors. Applied Ocean Research. 54, 101-114.

[36] Drilling Formulas. Suction Anchor Calculation. (2022-07-31) https://www.drillingformulas.com/suction-anchor-calculation/: DrillingFormulas.

[37] Kwan, C.T., Bruen, F.J., 1991. Mooring line dynamics: comparison of time domain, frequency domain, and quasi-static analyses. Offshore Technology Conference. OnePetro.

[38] Wang, H.W., 2011. Research on truncation technology of deepwater mooring system in model test. HEU.

[39] API R P. 2SK. Recommended practice for design and analysis of stationkeeping systems for floating structures, 2005.

[40] Ormberg, H., Larsen, K., 1998. Coupled analysis of floater motion and mooring dynamics for a turret-moored ship. Applied Ocean Research. 20(1-2), 55-67.

[41] Ormberg, H., Fylling, I.J., Larsen, K., et al., 1997. Coupled analysis of vessel motions and mooring and riser system dynamics. Proceedings of the international conference on offshore mechanics and arctic engineering. American Society of Mechanical Engineers. 91-100.

[42] AS D N V G L. Position mooring. DNVGL-OS-E301, 2015.

[43] Xu, K., Larsen, K., Shao, Y., et al., 2021. Design and comparative analysis of alternative mooring systems for floating wind turbines in shallow water with emphasis on ultimate limit state design. Ocean Engineering. 219, 108377.

[44] Dan, D., Chen, Z., Yan, X., 2014. Closed-form formula of the transverse dynamic stiffness of a shallowly inclined taut cable. Shock and Vibration.

[45] Berlioz, A., Lamarque, C.H., 2005. A non-linear model for the dynamics of an inclined cable. Journal of Sound and vibration. 279(3-5), 619-639.

[46] Jiang, K.H., 2005. Study on buoy mooring system. Tianjin University.

[47] Liu, H., Huang, W., Lian, Y., et al., 2014. An experimental investigation on nonlinear behaviors of synthetic fiber ropes for deepwater moorings under cyclic loading. Applied Ocean Research. 45, 22-32.

[48] Luongo, A., Zulli, D., 2012. Dynamic instability of inclined cables under combined wind flow and support motion. Nonlinear Dynamics. 67(1), 71-87.

[49] Huang, W., Liu, H., Lian, Y., et al., 2013. Modeling nonlinear creep and recovery behaviors of synthetic fiber ropes for deepwater moorings. Applied Ocean Research. 39, 113-120.

[50] Bhattacharjee, S., 2015. Design and Installation Challenges for Deepwater Mooring Systems. 2015.

[51] Elman, P., Bramande, J., Elletson, E., et al., 2013. Reducing uncertainty through the use of mooring line monitoring. OTC Brasil. OnePetro.

[52] Siréta, F.X., Zhang, D., 2018. Smart mooring monitoring system for line break detection from motion sensors. The Thirteenth ISOPE Pacific/Asia Offshore Mechanics Symposium. OnePetro.

[53] Bayati, I., Efthimiou, L., 2021. Challenges and opportunities of major maintenance for floating offshore wind. World Forum Offshore Wind eV.

[54] Yuan, Z.M., Incecik, A., Ji, C., 2014. Numerical study on a hybrid mooring system with clump weights and buoys. Ocean Engineering. 88, 1-11.

[55] Xu, S., Wang, S., Soares, C.G., 2020. Experimental investigation on hybrid mooring systems for wave energy converters. Renewable Energy. 158, 130-153.

[56] Lian, Y., Liu, H., Hu, L., 2015. Feasibility analysis of a new hybrid mooring system applied for deep waters. The Twenty-fifth International Ocean and Polar Engineering Conference. OnePetro.

[57] Benassai, G., Campanile, A., Piscopo, V., et al., 2014. Mooring control of semi-submersible structures for wind turbines. Procedia Engineering. 70, 132-141.

[58] Campanile, A., Piscopo, V., Scamardella, A., 2018. Mooring design and selection for floating offshore wind turbines on intermediate and deep water depths. Ocean Engineering. 148, 349-360.

[59] Flory, J.F., Banfield, S.J., Berryman, C., 2007. Polyester mooring lines on platforms and MODUs in deep water. Offshore Technology Conference. OnePetro.

[60] Davies, P., Weller, S.D., Johanning, L., et al., 2014. A review of synthetic fiber moorings for marine energy applications. 5th International Conference on Ocean Energy (ICOE 2014), 4th-6th November 2014, Halifax.

Sustainable Marine Structures

https://ojs.nassg.org/index.php/sms

EDITORIAL
Marine Structures under Special Loads

Chandrasekaran Srinivasan[*]

Madras Institute of Technology, India

Environmental loads that act on marine structures are highly non-deterministic in general. Estimating these loads is a basic requirement for their structural design, but their response is far beyond just counteracting the loads [1,2]. The marine environment poses more challenges starting from the choice of material, structural form, design methods, construction techniques, inspection methods, repair, and retrofitting. Furthermore, strength degradation and service life decrement are complex to estimate as they pose a non-proportional response to age and material use. Special loads such as fire, impact, blast, and loads that arise from marine growth need a special revisit. As the conventional design codes are silent about the recommendations for such special loads, design engineers satisfy the special requirements based on their domain expertise and experience. Corrosion is one of the major threats to the structural members of the marine environment. X52 steel, one of the most-preferred candidates for steel members,

also faces explicit challenges under this corrosive environment. Functionally Graded Materials (FGM), one of the recent advancements in material science, is seen as an effective alternative to counteract the challenges imposed by the marine environment. But, due to the limited knowledge of FGM and its manufacturing techniques, marine engineers cannot take the way out of using conventional marine steel. Apart from a very high-cost factor, relative disadvantages possessed by X52 steel in the marine environment are grossly ignored for want of no alternative.

Marine structures built for coastal protection should possess high reserve strength and long service life. Not because they are strategically important, but because they cannot often be structurally intervened for repair. Furthermore, repair of marine structures like jetties, dry docks, and breakwaters is generally carried out while they are in service. It is obvious that repairing structural members who face strength degradation is quite challenging

*Corresponding Author:
Chandrasekaran Srinivasan,
Madras Institute of Technology, India;
Email: drsekaran@iitm.ac.in

when they are in service [3]. Capacity reduction without any incremental decrease in the encountered loads places marine structures under a special category of repair and retrofitting. Invasive methods such as pressure grouting, crack filling with chemical admixtures, and waterproofing treatments are only cosmetic and shall not help restore the strength of structural members; but, even such methods of repair are directed by the chemical admixture manufacturers, which fall in the domain of non-engineering practices.

Inviting papers from academia, practicing engineers, and researchers addressing the above concerns aims to enlighten readers about robust design practices and repair techniques.

We believe that the papers, though few, shall help the readers understand the focussed complexities faced by marine structures. On behalf of the journal's Editorial Board, I sincerely thank the authors for contributing original papers to this journal. I shall expect a few more contri-butions from academia in the future.

Conflict of Interest

There is no conflict of interest.

References

[1] Chandrasekaran, S., Jain, A.K., Shafiq, N., et al., 2021. Design aids for offshore platforms under special loads, CRC press, Florida. pp. 280.

[2] Chandrasekaran, S., 2020. Design of Marine Risers with Functionally Graded Materials, Woodhead Publishing, Elsevier. pp. 200.

[3] Liu, H.J., Li, H.N., Fu, X., 2021. Wind-resistant performance and failure modes for a semi-submersible offshore platform during jacking closure. Ocean Engineering.
DOI: https://doi.org/10.1016/j.oceaneng.2021.110102